Computational modeling and analysis of low temperature combustion regimes for advanced engine applications

by

Pinaki Pal

A dissertation submitted in partial fulfillment
of the requirements for the degree of
Doctor of Philosophy
(Mechanical Engineering)
in The University of Michigan
2016

Doctoral Committee:

Professor Hong G. Im, Co-Chair
Professor Margaret S. Wooldridge, Co-Chair
Professor Arvind Atreya
Professor Nikolaos D. Katopodes
Associate Professor Venkatramanan Raman

To my parents,

Mausumi and **Biraj**,

and my sister **Mangistha**,

for a lifetime of love, support and motivation

Acknowledgements

This thesis marks the culmination of a wonderful and exciting journey for me. A number of people have contributed to making this phase of my life *very very special*. I would, therefore, like to take this opportunity to express my sincere gratitude to all of them for their tremendous support and encouragement.

First and foremost, I am grateful to my awesome advisors, Prof. Hong Im and Prof. Margaret Wooldridge. Since the very beginning of my graduate studies back in Fall 2011, Prof. Im has been my mentor and teacher. Over the years, he has shared vast amount of knowledge and experience with me from which I have learnt a great deal. I highly appreciate his patience, unwavering support and sheer trust in me to succeed. At every step, he has created opportunities for me to grow as an independent researcher. Whenever in need, I have gained invaluably from his deep wisdom and friendly advice. Moreover, his remarkably calm, humble and warm nature has been something I have always looked up to.

From the beginning of 2013, I became even more fortunate when I started working with Prof. Wooldridge as well. I have found her super positive attitude and never-ending zeal for combustion science, research and life in general, very infectious! Her dedication and enthusiasm towards work has, on a number of occasions, motivated me to put an extra ounce of effort into my own research. Teaming up with her has been a truly enjoyable and rewarding experience for me.

I am very glad as well as proud to have both of them by my side and have the highest regards for them, not just as amazing advisors and teachers, but

also as genuine human beings. You have influenced my life in more positive ways than you can ever imagine…Thank you for everything!

I would also like to thank the other members of my committee, Profs. Arvind Atreya, Venkat Raman and Nikolaos Katopodes, for taking keen interest in my work and providing constructive feedback to improve the quality of this thesis. Thank you for your time, effort and encouragement! In addition, I am grateful to Prof. Mauro Valorani for his guidance and technical support in using the CSP code developed by him at Sapienza University of Rome. A special note of thanks for Prof. Kendal Bushe of University of British Columbia…my three-month internship under his supervision back in the summer of 2010 as an undergraduate student, was instrumental in drawing me towards the field of combustion science. I am thankful to him for showing me a wonderful career path which has been thoroughly exciting and intellectually satisfying.

Next, I would like to thank my labmates and colleagues for their immense contribution to my research. During my initial years as a graduate student, the warm and welcoming energy of Saurabh, Paul and LC made it very easy for me to blend in. I have enjoyed my discussions with them on both research and non-research topics. Thanks to Dr. SeungHwan Keum of General Motors, who did an unbelievable job of guiding me remotely, just through e-mails. He spent a lot of his time and energy on sharing invaluable insights and introduced me to the world of KIVA simulations. Thanks to Dr. Janardhan Kodavasal and Dr. Aris Babajimopoulos for fruitful discussions on engine combustion modeling. It was great fun to collaborate with Andrew on the ignition regime study. Many thanks to Paul, who was always there to get me out of trouble whenever I ran into any code debugging issue or needed any programming advice. He has indeed helped me through some very desperate times. Without his technical expertise, my journey wouldn't have been so smooth. In addition, I also sincerely thank Mohammad, Scott, Cesar,

Dimitris, Hui, Ripudaman, Insu, Brandon and Alex, for their continuous support and close friendships.

I would also like to acknowledge the technical assistance of U-M CAEN and KAUST IT support staffs. I have bugged them with innumerable queries and issues in the past, and every time they have been very kind and patient in helping me out as quickly as possible. I really appreciate it!

In addition, a big thanks to all my undergraduate mentors at IIT Kharagpur: Profs. Abhijit Guha, Souvik Bhattacharyya, Maddali Ramgopal, Koeli Ghoshal and Suman Chakraborty. I believe that under their tutelage, I became well-prepared to handle the challenges of graduate studies later at the University of Michigan. I also thank my Physics teacher, Mrs. Bharti Pillai, from good old school days, whose best wishes continue to be with me even now.

During my stay here in Ann Arbor, I have been extremely fortunate to have made some great friends outside my workplace. First of all, I want to thank my '1660 McIntyre' family: Yash, Rahul (a.k.a. Modi) and Shubhi (a.k.a. Chabaddu/Chabbu/Chubs), for making me feel at home, away from home. As housemates, we shared countless memorable moments with each other that I will continue to cherish forever. I am also grateful to Rupali (a.k.a. Jhalli), Sneha, Swetha, Neha, Maya, Uttara, Sharath and Vasu, for their true friendships and all the fun times! In addition, I am thankful to my friends in India: Deepanshu, Mayank, and Ajit, for always wishing the best for me.

Most importantly, I want to thank my parents, Mausumi and Biraj, and my gorgeous sister, Mangistha, for their unconditional love and perpetual support. Their belief in me has kept me going during the most difficult times of my life. I owe all my accomplishments to them and hope that I will continue to make them proud. *Love you guys!*

Table of Contents

List of Figures

List of Tables

Abstract

Computational modeling and analysis of low temperature combustion regimes for advanced engine applications

By

Pinaki Pal

Co-Chairs: Hong G. Im & Margaret S. Wooldridge

To achieve cleaner and more efficient energy utilization, novel strategies in modern combustion devices for both automotive and stationary power generation applications operate using lean, nearly homogeneous reactant mixtures at high pressure conditions. These include low temperature combustion (LTC) engines and stationary gas turbines using lean premixed combustion, among many examples. Under these conditions, auto-ignition often becomes a dominant process for burning. As such, accurate prediction of auto-ignition characteristics – the ignition delay times as well as the entire evolution of the fuel consumption behavior – is of paramount importance in successful implementation of these advanced combustion systems.

The first part of this dissertation focuses on auto-ignition characteristics at high-pressure, low-temperature conditions, relevant to modern gas turbine

engines. Recent experimental observations have reported large discrepancies between measurements and homogeneous chemical kinetic modeling predictions in the ignition delay times at these operating conditions, with the former being orders of magnitude lower than the latter. This discrepancy has been attributed to a transition in auto-ignition behavior from *strong* (characterized by nearly homogeneous ignition) regime to *weak* (initiated by localized reaction sites and followed by front propagation) regime as the initial mean temperature is lowered, owing to an increased sensitivity of ignition delay time to thermal non-uniformities. In light of these observations, the present work computationally investigates strong and weak ignition regimes in the presence of thermal inhomogeneities. Predictive criteria based on Zel'dovich's theory and passive scalar mixing, which can capture the ignition behavior *a priori*, are first proposed and validated using extensive parametric tests of laminar systems of a lean syngas/air mixture in a one-dimensional configuration. Subsequently, a non-dimensional scaling analysis is carried out to extend the regime criteria to turbulent reacting flows in terms of the characteristic turbulent Reynolds and Damköhler numbers, thereby leading to a turbulent ignition regime diagram. The ignition regimes are classified into three categories: *weak* (where deflagration is the dominant mode of fuel consumption), *reaction-dominant strong* and *mixing-dominant strong* (where volumetric ignition is the dominant mode of fuel consumption). The regime diagram is then, numerically validated against two-dimensional direct numerical simulations (DNS) of syngas/air auto-ignition in the presence of turbulent velocity and temperature fluctuations. A number of parametric test cases, by varying the turbulent Damköhler and Reynolds numbers, are considered. The evolution of the corresponding auto-ignition phenomena, pressure rise, and heat release rate are analyzed. In addition, combustion mode analysis based on front propagation speed and computational singular perturbation (CSP) is also applied to characterize the auto-ignition phenomena. The observed ignition

behaviors are found to be consistent with the predictions of the regime diagram. This demonstrates that the proposed regime diagram comprehensively captures the physical and chemical mechanisms controlling the auto-ignition phenomena in thermally inhomogeneous turbulent reacting flows.

In the second part of the dissertation, validity of a high-fidelity Reynolds-Averaged Navier Stokes (RANS) based spray-interactive flamelet (SIF) combustion model to the simulation of stratified LTC in a direct-injection compression ignition (DICI) engine is assessed, which incorporates the complex interaction between spray evaporation, gas-phase combustion and turbulent mixing. A number of parametric cases are considered, spanning a wide range of in-cylinder charge stratification, by way of varying the fuel start-of-injection (SOI) timing. The numerical results are validated against available experimental data for in-cylinder pressure trace, combustion efficiency, and CO and NO_x emissions. The SIF model results are also compared with those for an extended multi-zone combustion model. It is observed that the SIF model performs well for a wide range of stratified conditions, which is attributed to its ability to incorporate the effects of small-scale turbulent transport on combustion. Finally, the SIF model is employed to further investigate the impact of fuel injection parameters such as injection pressure and spray cone angle on the performance of the DICI engine at low load conditions, for the most delayed SOI timing. Relative effectiveness of the two injection parameters in extending the low load limit of homogeneous charge compression ignition (HCCI) through delayed fuel injection strategy is assessed by conducting extensive parametric studies. The results show that increasing the injection pressure and widening the spray cone angle can reduce NO_x emissions significantly by way of enhanced mixing, while keeping the combustion efficiency reasonably high.

Chapter 1
Introduction

Our society relies heavily on internal combustion (IC) engines for transportation, commerce and power generation. These engines burn vast quantities of fossil fuels. Indeed, 76% of 86 million barrels of crude oil that we consume every day is used in IC engines [1]. These consumption needs are certainly going to increase as even more economic development takes place worldwide in the near future. However, there are insufficient fuel reserves to meet the increasing demand, owing to the non-renewable nature of our primary energy resources, which can adversely affect fuel prices. If the current trend continues, world oil prices are expected to reach $125 per barrel in 2035 as compared to $84.5 per barrel in 2012 [2]. Another issue associated with the massive usage of fossil fuels is that of the accompanying emissions of pollutants, including nitrogen oxides (NO_x) and particulates (soot), in addition to the production of carbon dioxide (CO_2). Pollutant emissions have raised serious environmental and health concerns. For example, the world's annual production of 37 billion tons of CO_2 contributes to green house gases (GHG), which could lead to climate change with unpredictable and irreversible consequences [1]. This has led to more stringent emissions regulations that are continually being tightened further.

In light of the above discussion, there is great need and incentive to curtail dependency on petroleum and to make the best use of world's limited fossil fuel resources, by improving IC engine efficiency and fuel economy, and reducing emissions. This calls for advanced engine technologies and operating strategies as well as utilization of alternative fuels. Towards clean

and efficient energy utilization, new strategies in combustion devices for both automotive and stationary applications operate using lean, nearly homogeneous reactant mixtures at boosted pressure conditions. These include low temperature combustion engines [3] and stationary gas turbines employing lean premixed combustion [4], among many examples. Under these conditions, auto-ignition often becomes a dominant process for burning. As such, accurate prediction of autoignition characteristics – the ignition delay times as well as the entire evolution of the fuel consumption behavior – is of paramount importance in successful implementation of these combustion systems.

1.1 Syngas fuel for stationary gas turbines

1.1.1 Potential as an alternative fuel

Currently, energy derived from coal accounts for almost half of the electricity produced in the US. As the demand for electrical power continues to escalate and the supply of petroleum becomes more costly and insecure, coal is expected to dominate the energy landscape for the foreseeable future, with existing US coal reserves estimated to last more than 250 years based on current demand levels [5]. However, coal power is the most carbon-intensive as well as the most polluting energy source in terms of nitrogen oxides (NO_x), sulfer oxides (SO_x) and particulate matter emissions. Consequently, there is a strong need to develop cleaner and more efficient coal technologies.

In recent years, the utilization of reformed fuels has been considered as an attractive alternative for electric power generation. Among these reformed fuels, which can be derived from coal, biomass and organic waste, high-hydrogen-content (HHC) fuels such as synthetic gas (syngas), containing

hydrogen (H_2) and carbon monoxide (CO) as primary fuel components, are particularly attractive for power generation applications [6]. The integrated gasification combined cycle (IGCC) process has emerged as a viable technology for syngas combustion in advanced power plants. In a coal-based IGCC power plant, syngas is produced by partial oxidation of coal in pure oxygen and steam in high pressure gasifiers [7]. After most of the harmful and corroding contaminants, such as sulfer oxides, ammonia and particulates are removed in a post-gasification process, the syngas is combusted in a gas turbine cycle, and excess heat is converted in a subsequent steam turbine cycle. Besides significant reduction of pollutant emissions and potential for higher thermal efficiencies as compared to conventional coal-fired power plants, this technology also facilitates removal of greenhouse gases when combined with pre-combustion carbon capture and sequestration methods [8]. Furthermore, syngas mixtures can also be used to produce liquid fuels through Fischer Tropsch conversion [9, 10] or to generate pure hydrogen via Water-gas shift technologies.

1.1.2 Challenges to syngas combustion

Despite enormous opportunities in improving combustion efficiency and reducing emissions, syngas combustion in IGCC power plants introduces significant technological and scientific challenges. These challenges mainly arise due to process-related variations in syngas composition, lower density and higher diffusivity of hydrogen as compared to hydrocarbon fuels, and the overall lean operating conditions. Although syngas is primarily composed of H_2 and CO, potential variations are possible in its composition such as, carbon/hydrogen ratio, varying levels of carbon dioxide and water, as well as the presence of other trace species [11]. Therefore, gas turbine combustors operating on syngas must be fuel-flexible. Moreover, the unique thermo-

diffusive properties of hydrogen lead to higher flame speeds, extended flammability limits and lower ignition temperatures, which can affect combustion stability and fuel conversion adversely [12]. In addition, there has been a focus on reducing NO_x emissions that would result from stoichiometric combustion of HHC fuels like syngas, due to high flame temperatures. A common strategy of lowering combustion temperatures is to operate in the lean premixed mode (with fuel-to-air equivalence ratio around 0.5) [13], for which combustion stability depends more highly on auto-ignition characteristics [14]. The IGCC gas turbines typically operate at high pressures ($10 < P < 30$ atm) and low/intermediate temperatures ($T < 1000$ K) [15]. However, syngas combustion under these conditions is not sufficiently understood.

Recent experimental investigations [5, 15-18] reported large discrepancies between measurements and homogeneous chemical kinetic modeling predictions in the ignition delay times of syngas at these conditions, with the experimental values being orders of magnitude lower than the corresponding model predictions. A number of potential contributing factors were proposed to explain the observed discrepancies, such as uncertainties in kinetic rate constants of certain key elementary reactions, for example, $CO + HO_2 = CO_2 + OH$, presence of gas impurities and surface-catalytic processes [15, 17, 19, 20]. In addition, it was recognized that the presence of thermal inhomogeneities at high pressures and low temperatures may also contribute to the overall ignition advancement in comparison with the homogeneous prediction, by way of early flame kernel growth and front propagation. For example, Medvedev et al. [21] analyzed the ignition delay data reported by various experimental facilities [16, 22, 23] and reported that at relatively low temperatures, the measured ignition delays were close to the time scales of deflagrative flame propagation, which were much shorter than the corresponding homogeneous ignition delays. In a recent experimental study

using syngas in the University of Michigan (U-M) rapid compression facility (RCF), Mansfield and Wooldridge [24] demonstrated a transition in the auto-ignition behavior from *strong* (characterized by nearly homogeneous ignition) to *weak* (initiated by localized reaction sites and followed by front propagation) regime as the initial mean temperature was lowered (as shown in Figure 1.1). The issue of premature ignition by local hot spots was also encountered recently for other fuels such as, n-heptane and 2-methylfuran, in some shock tube studies [25, 26].

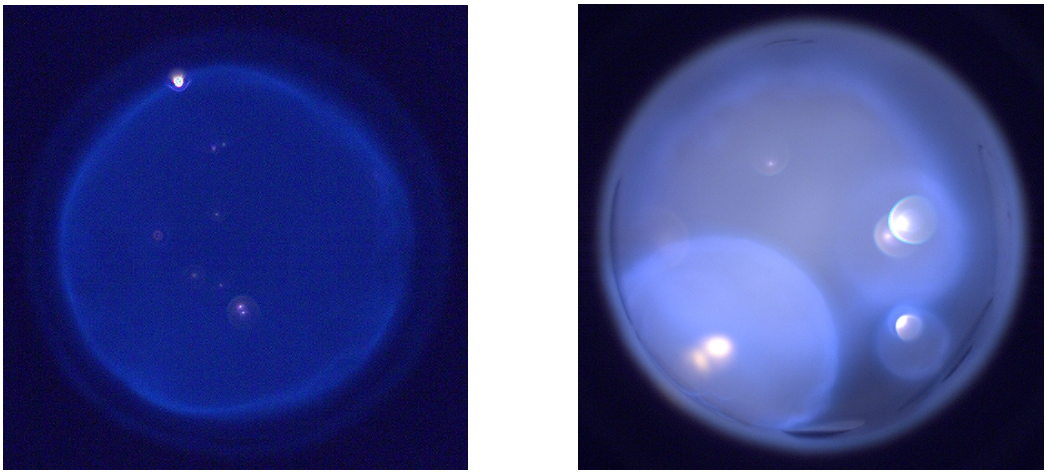

(a) (b)

Figure 1.1: (a) Single frame from high-speed imaging of homogeneous (strong) ignition behavior for experimental conditions P = 3.3 atm, T = 1043 K, Φ = 0.1; (b) Single frame from high-speed imaging of inhomogeneous (weak) ignition behavior for experimental conditions P = 9.2 atm, T = 1019 K, Φ = 0.5 [24].

These observed trends were qualitatively similar to earlier shock tube studies of hydrogen-oxygen ignition [27-30], in which localized ignition at an early stage led to a significant acceleration in the ignition delay times. Meyer

and Oppenheim [28] reported that the boundary between strong and weak ignition coincided with an iso-line of the sensitivity of homogeneous ignition delay time to temperature, $d\tau_{ig}/dT$, in the pressure-temperature space. Consistent behavior was found in the U-M RCF study [24], where a $d\tau_{ig}/dT$ = *constant* line served as a reasonable criterion to differentiate between the strong and weak ignition regimes. Moreover, several criteria to identify the transition between strong and weak ignition regimes were evaluated, including the theoretical criterion proposed by Zel'dovich [31]. The modified criterion proposed by Sankaran et al. [32], based (in part) on the ignition delay time sensitivity, was found to reproduce the experimentally observed trends very well. Recently, reduced order modeling was also attempted [33, 34] to demonstrate that turbulent fluctuations can also result in significant advancement of overall ignition. These recent findings have led to a consensus in the community that scalar non-uniformities are the likeliest causes of the discrepancies between zero-dimensional modeling and experimental auto-ignition delay data [35].

Considering the significance of different ignition regimes in determining the net ignition delay times, it is very important and useful to obtain rational criteria to predict whether a given mixture will ignite in the strong or weak regime. To this end, it is evident that a constant $d\tau_{ig}/dT$ criterion is not sufficient, as a perfectly homogeneous mixture would certainly ignite in the strong regime regardless of the mixture's ignition sensitivity. An additional parameter to represent the local or global temperature distribution within the mixture must also be considered.

1.2 Objectives I

Based on the above discussion pertaining to anomalous auto-ignition behaviors in section 1.1.2, the objectives of the first part of the thesis are as follows:

- To numerically investigate strong and weak auto-ignition regimes at high-pressure, low-temperature conditions in the presence of thermal inhomogeneities. Predictive criteria, which can capture the ignition behavior *a priori*, are proposed and validated using extensive parametric tests of laminar systems of a lean syngas/air mixture in simple one-dimensional (1D) configuration. This will be discussed in Chapter 2.
- To extend the regime criteria to turbulent reacting flows in terms of non-dimensional parameters that are commonly used in characterizing turbulent combustion systems. The scaling relations thus developed are put together into a turbulent ignition regime diagram. This will be discussed in Chapter 3.
- To validate the regime diagram against two-dimensional (2D) direct numerical simulations (DNS) of auto-ignition of a compositionally homogeneous lean syngas/air mixture in the presence of thermal non-uniformities and turbulent fluctuations. This will be discussed in Chapter 4.

1.3 Low temperature combustion for automotive engines

1.3.1 Homogeneous Charge Compression Ignition (HCCI)

The existing gasoline spark-ignition (SI) and diesel compression ignition (CI) technologies are unable to meet the simultaneous requirements of high-efficiency and low emissions. Currently, diesel engines are commonly used for

transportation applications requiring high power density, such as heavy duty vehicles, locomotive and marine engines, because of their higher fuel efficiency and greater reliability. However, conventional CI engines suffer from large NO_x and soot emissions, due to high in-cylinder temperatures and fuel-rich burning. Therefore, emission aftertreatment devices, such as diesel particulate filter (DPF), lean NO_x trap (LNT) and selective catalytic reduction (SCR) systems are required to meet the stringent emission regulations. These systems are expensive and increase the cost of the vehicle enormously. In contrast, SI engines are mostly used in smaller passenger cars and result in lower soot emissions due to nearly stoichiometric premixed combustion. The major disadvantage of SI engines, however, is that their compression ratio is limited by knock, resulting in lower thermal efficiency. In addition, the throttle used to control the air mass flow into the combustion chamber gives rise to pumping losses and further reduction in efficiency.

Recent drive for cleaner and more efficient IC engines has led to investigations of advanced combustion strategies based on low temperature combustion (LTC) that have the ability to yield low NO_x and soot emissions while maintaining high fuel efficiency as shown in Figure 1.2 [36-40]. These methods basically rely on the principle of dilute premixed or partially premixed combustion to reduce emissions. Homogenous charge compression ignition (HCCI) is one of the advanced LTC concepts that have been receiving substantial attention over the last few decades [36, 38, 40]. HCCI employs a well-mixed fuel-air charge like SI engines and relies on CI like diesel engines [41, 42]. Similar to diesel engines, the use of high compression ratios and removal of the throttling valve in HCCI allow for high efficiency operation. On the other hand, the use of a highly diluted premixed fuel-air charge allows for low emissions of NO_x, soot and particulate matter. Therefore, HCCI offers the potential to achieve high efficiencies comparable with diesel while

allowing clean emissions and using relatively inexpensive aftertreatment technologies.

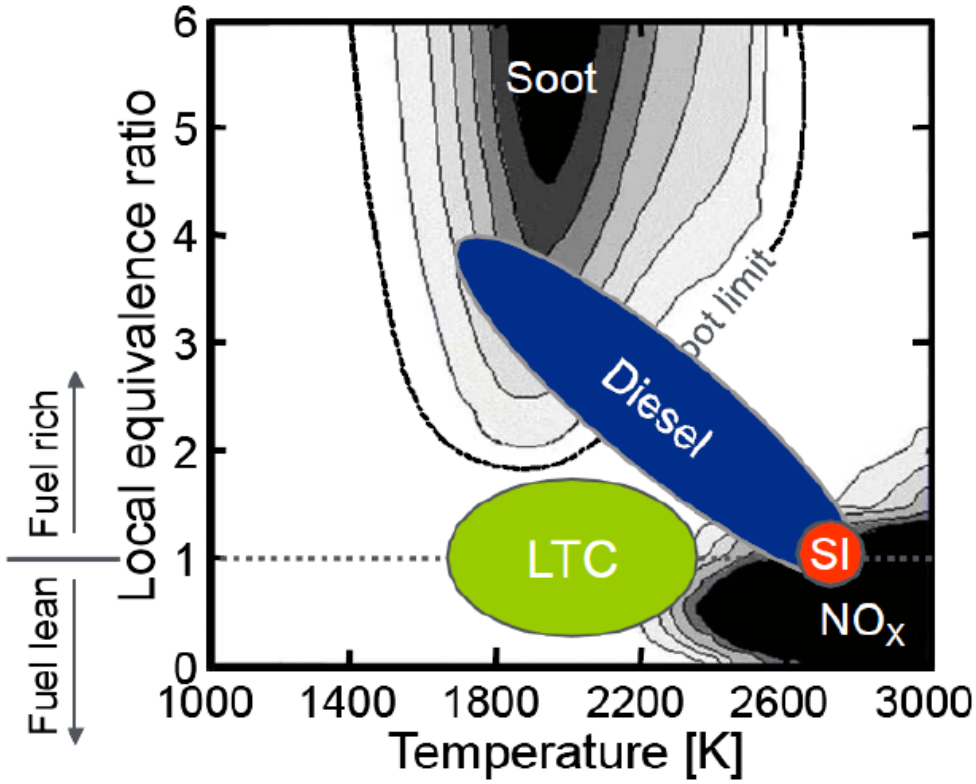

Figure 1.2: Conventional gasoline SI, diesel CI and LTC operating regimes [37].

In spite of these benefits, there are some critical challenges that need to be overcome before the full potential of HCCI combustion can be realized in production applications. One of the main challenges is control of combustion phasing. Unlike conventional SI and CI engines, there is no direct method for controlling the start of combustion. Instead, the start of combustion is purely dictated by the auto-ignition of the fuel-oxidizer mixture, which is influenced by the properties of the mixture and the time-temperature history to which it is exposed [38]. This makes HCCI highly sensitive to a number of factors [43]:

auto-ignition properties of the fuel, fuel concentration, residual rate, mixture homogeneity, intake temperature, latent heat of vaporization of fuel, heat transfer to the engine and other engine-dependent parameters. Another shortcoming of HCCI is its narrow operating range due to the lack of control of heat release rate. At high loads, HCCI suffers from very rapid pressure rise rates that can result in severe engine knock [44]. On the other hand, under low load conditions, HCCI results in a high level of unburned hydrocarbon (UHC) and CO emissions due to low bulk gas temperatures (< 1400 K), resulting in steep decline in combustion efficiency [45].

1.3.2 Stratified LTC

The process involved in mixing fuel and air has important effects on the HCCI combustion process. With HCCI, the start of combustion is dictated by auto-ignition chemical kinetics. Thus, controlling the combustion phasing requires tuning of the auto-ignition kinetics, which is affected by the charge composition and the pressure and temperature histories of the reactants during piston compression [38]. Over the last decade, many experimental and computational studies have demonstrated that inherent or designed in-cylinder stratifications in temperature and mixture composition can spread out the rate of pressure rise (heat release) by changing the combustion mode of homogeneous auto-ignition to a mixed combustion mode of simultaneous auto-ignition and deflagration [32, 37, 46-58]. This can be achieved by a number of stratified LTC approaches, such as partially premixed compression ignition (PPCI) by way of variable valve timing (VVT) for residual gas trap [59] and multi-stage spray injection [60], spark-assisted compression ignition (SACI) [3, 61] which generates deflagrations prior to volumetric auto-ignition thereby spreading out the pressure rise rate, and reactivity-controlled compression ignition (RCCI) which relies on port-fuel injection of a low-

reactivity fuel and late direct injection of a high-reactivity fuel to create fuel reactivity gradients in the in-cylinder [62, 63, 64]. These advanced strategies, however, introduce considerable complexity to the auto-ignition and subsequent combustion processes.

In the presence of thermal and compositional stratifications, turbulent mixing also affects ignition timing and pollutant formation processes. On one hand, turbulence affects combustion indirectly via increased convective wall heat transfer [65, 66]. Secondly, it also affects the mean reaction rate under certain mixture conditions when the fuel-air mixture is not perfectly mixed. Recent high-fidelity 2D turbulent direct numerical simulation (DNS) studies with thermal stratifications [52-55] and both thermal and compositional stratifications [51, 56, 57] have revealed that turbulence may advance or retard overall ignition depending on the ratio of turbulence time scale (τ_t) to ignition delay time scale (τ_{ig}). It is, therefore, important from combustion modeling standpoint, to incorporate proper turbulent mixing models and account for turbulence-chemistry interaction in predictive simulations of stratified LTC engines.

1.3.3 Combustion modeling of LTC engines

In the context of HCCI, a wide variety of combustion models based on the multi-zone (MZ) [67] approach have been extensively developed for engine simulations. The MZ approach assumes that chemistry is independent of turbulence and hence can be described without modeling the influence of small-scale turbulent eddies. This assumption is predicated on the widely accepted view that HCCI is essentially dictated by chemical kinetics only [42]. In this approach, the fluid dynamic processes are computed on a highly resolved grid, while the progress in chemical reaction at each time step is computed by mapping the entire computational cells into a smaller number of

zones with similar temperature and pressure histories, in favor of reduced computational cost. Although MZ models have been demonstrated to perform well at weakly stratified charge conditions [68, 69, 70], it is believed that strong turbulent scalar mixing and transport within fronts may cause such models to lose accuracy at highly stratified conditions [71, 72].

Another combustion modeling framework used extensively for engine simulations is the flamelet [73] approach, which assumes that chemistry is fast relative to mixing time scales. The species compositions and temperature are thus described on a one-dimensional manifold governed by the mixture fraction variable, thereby substantially reducing the computational overhead of solving for the reactive scalar variables in the three-dimensional (3D) physical space. However, unlike the MZ models, turbulence-chemistry interactions at small scales are taken into account via the scalar dissipation rate of the mixture fraction [74]. The representative interactive flamelet (RIF) [75-79] model derived from the original laminar flamelet concept has been applied to simulate engine combustion using single or multiple unsteady flamelet formulations. Subsequently, further refinements have been incorporated to expand the applicability of RIF model to the modeling of mixed-mode combustion encountered in homogeneous-charge late-injection (HCLI) engines [80, 81, 82] and direct-injection compression ignition (DICI) engines [83, 84, 85].

1.4 Objectives II

In light of the previous discussion in sections 1.3.2 and 1.3.3, the objectives of the second part of the thesis are as follows:

- To assess the validity of a novel flamelet-based [85] and existing MZ-based [70] combustion modeling approaches to the simulation of stratified

LTC at low load in a DICI engine. A number of parametric cases are considered spanning a wide range of in-cylinder charge stratification, by way of varying the start-of-injection (SOI) timing. The numerical results are compared with available experimental data [46]. This will be discussed in Chapter 5.

- To numerically investigate the impact of fuel injection parameters such as injection pressure and spray cone angle on the resultant combustion process and pollutant emissions, and thereby explore further potential for extension of low load limit of HCCI. This will be discussed in Chapter 6.

1.5 Outline of Dissertation

The main technical contents of the dissertation are organized as follows:

- In Chapter 2, simple 1D simulations incorporating detailed chemistry and transport are performed to investigate auto-ignition characteristics at high-pressure, low-temperature conditions in the presence of thermal non-uniformities. A lean syngas/air reactant mixture is considered. Effects of both bulk thermal gradients and local thermal hot spots are studied via extensive parametric tests. Two predictive non-dimensional criteria to capture the transition between strong and weak ignition regimes are identified and validated against the simulation results.
- The main purpose of Chapter 3 is to extend the *a priori* criteria developed earlier in Chapter 2 to turbulent reacting flows. A theoretical non-dimensional scaling analysis is conducted based on Kolmogorov's theory of homogeneous turbulence to develop modified predictive criteria for ignition of a compositionally homogeneous reactant mixture in the presence of turbulent velocity and temperature fluctuations. This leads to

an ignition regime diagram in the turbulent Reynolds number - Damköhler number space, that provides guidance on expected ignition behavior based on the thermo-chemical properties of the mixture and the flow/scalar field conditions.

- In Chapter 4, the proposed ignition regime diagram is validated against 2D DNS of auto-ignition of a homogeneous lean syngas/air mixture in the presence of turbulence and thermal fluctuations. Various parametric test cases are chosen such that they lie in different regions on the regime diagram. The auto-ignition behavior for each case is characterized based on the analysis of heat release rate, front propagation speed and relative importance of transport versus chemistry. Subsequently, the observed auto-ignition behaviors are compared with those predicted by the ignition regime diagram.
- In Chapter 5, closed-cycle computational fluid dynamics (CFD) simulations of LTC of iso-octane in a direct-injection compression ignition (DICI) engine at low load conditions are performed. A number of parametric cases are considered by varying the SOI timing, ranging from very early fuel injection (140^0 before top-dead-center (bTDC)) to delayed fuel injection (45^0 bTDC) timings. A spray-interactive flamelet (SIF) combustion model incorporated into the computational fluid dynamics (CFD) code is validated against available experimental data for in-cylinder pressure trace, combustion efficiency, and CO and NO_x emissions. In addition, the SIF model results are also compared with those for an extended multi-zone (EMZ) combustion model, in order to investigate the importance of incorporating the effects of turbulence-chemistry interaction in the combustion model. Mathematical formulation and details of the SIF and EMZ combustion models are also included in Chapter 5.

- In Chapter 6, the SIF model is employed to further investigate the impact of fuel injection parameters such as injection pressure and spray cone angle on the performance of the DICI engine at low load conditions, for the most delayed SOI timing. Relative effectiveness of the two injection parameters in extending the low load limit of HCCI through delayed fuel injection strategy is assessed by conducting extensive parametric studies.
- Finally, Chapter 7 summarizes the main contributions and insights from this work and provides recommendations for future study.

The original contributions presented in this dissertation have also been reported/are to be reported in the following journal publications:

- Chapter 2: ***Pinaki Pal****, Andrew B. Mansfield, Paul G. Arias, Margaret S. Wooldridge, Hong G. Im*: A computational study of syngas auto-ignition characteristics at high-pressure and low-temperature conditions with thermal inhomogeneities, *Combustion Theory and Modelling*, 19(5), 2015, pp. 587-601.
- Chapter 3: *Hong G. Im,* ***Pinaki Pal****, Margaret S. Wooldridge, Andrew B. Mansfield*: A regime diagram for autoignition of homogeneous reactant mixtures with turbulent velocity and temperature fluctuations, *Combustion Science and Technology,* 187 (8), 2015, pp. 1263-1275.
- Chapter 4: ***Pinaki Pal****, Mauro Valorani, Paul G. Arias, Hong G. Im, Margaret S. Wooldridge, Pietro P. Ciottoli, Riccardo M. Galsssi*: Computational characterization of ignition regimes in a syngas/air mixture with temperature fluctuations, *Proceedings of the Combustion Institute,* 2016 (submitted).
- Chapter 5: ***Pinaki Pal****, SeungHwan Keum, Hong G. Im*: Assessment of flamelet versus multi-zone combustion modeling approaches for stratified-charge compression ignition engines, *International Journal of Engine Research,* 2015, DOI: 10.1177/1468087415571006.

- Chapter 6: *SeungHwan Keum,* ***Pinaki Pal****, Hong G. Im, Aristotelis Babajimopoulos, Dennis N. Assanis*: Effects of fuel injection parameters on the performance of homogeneous charge compression ignition at low-load conditions, *International Journal of Engine Research*, 2015, DOI: 10.1177/1468087415583597.

Chapter 2
High-pressure Low-temperature Syngas Auto-ignition in the Presence of Thermal Inhomogeneities

In this chapter, a computational study is conducted to investigate the characteristics of auto-ignition in a lean syngas/air mixture at high-pressure and low-temperature conditions in the presence of thermal non-uniformities. *A priori* criteria based on Zel'dovich's theory [31, 32] and passive scalar mixing are formulated and validated as predictive indicators of ignition regime of the reactant mixture. As a first step, extensive parametric studies are conducted using simple one-dimensional configurations with the level of initial temperature fluctuations being prescribed as the key parameter. The temperature inhomogeneities are represented by a global sinusoidal temperature profile and a local Gaussian temperature spike (hot spot). The corresponding ignition behaviors are then characterized and the resulting ignition delay times are reported in comparison with the reference homogeneous mixture conditions.

2.1 Numerical setup and initial conditions

1D constant-volume simulations are performed using the DNS code, S3D [86], which solves the compressible, Navier-Stokes, species continuity and total energy equations. A fourth-order explicit Runge-Kutta method and an eighth-order central differencing scheme are used for time integration and spatial discretization, respectively [87]. A detailed H_2/CO mechanism with 12

species and 33 chemical reactions [88] is employed. The mechanism is linked with CHEMKIN [89] and TRANSPORT [90] libraries for evaluating the reaction rates and thermodynamic and mixture-averaged transport properties, respectively. Periodic boundary conditions are imposed, such that heat release in the computational domain leads to pressure rise and compression heating of the reactants.

A number of parametric conditions are considered for initial pressures (P_0) of 10 atm and 20 atm, and the initial mean temperature (T_0) range of 850-1100 K, as typically encountered in gas turbines. A uniform syngas/air mixture with H_2:CO molar ratio of 0.7:1 and fuel-air equivalence ratio of 0.5 is chosen. In addition, the mixture is diluted with twice the amount of nitrogen present in the air (i.e. a molar ratio of N_2:O_2 = 11.28), to ensure the pressure rise is sufficiently high to serve as an indicator of auto-ignition, but also low enough to avoid shock wave formation [91, 92]. A uniform grid size of $4.7\ \mu m$ is used to allow sufficient resolution of the thin propagating fronts. The initial flow is quiescent.

Temperature non-uniformities are represented by two types of initial conditions. First, to represent moderate global temperature variations, a sinusoidal temperature profile is superimposed on the initial mean temperature, with a prescribed root-mean-square (RMS) fluctuation, T', and wavelength spanning the domain length, L. Alternatively, to represent a localized ignition source, a hot spot is represented by superimposing a Gaussian temperature profile, T_{hs}, onto the mean temperature:

$$T_{hs}(x) = \frac{A}{\pi}\exp\left[\frac{-2n^2(x-L/2)^2}{L^2}\right] - \frac{A}{2.5n} \qquad (2.1)$$

where the factor n governs the size of the hot spot and A determines the amplitude. By definition, T_{hs} has a zero mean so that the mean of the total

temperature distribution remains at T_0. The amplitude (ΔT) of the hot spot is varied in the range 25-100 K as observed in some syngas ignition experiments [93], while the size of the hot spot is kept constant at 0.6 cm. The value of n = 16 is chosen in order to keep the size of the incipient hot spot reasonably small (localized) as compared to the domain size, as has been typically observed in the experiments [24]. It is noted that for fixed domain length, initial mean temperature (T_0) and hot spot magnitude (A), a decrease in n results in an increase in the size/strength of the hot spot, while the initial end-gas temperature becomes lower in order to maintain constant T_0. Consequently, this would lead to a higher propensity for deflagrative front propagation. In other words, the effect of solely decreasing n is qualitatively similar to the effect of solely increasing A (section 2.3), and therefore is not discussed separately. The sensitivity to parameter n is directly reflected in the Sankaran number defined in section 2.2.1, representing the changes in the RMS temperature. Figure 2.1 shows examples of initial temperature profiles for the two types of prescribed thermal inhomogeneities. In the present work, the ignition regime is classified as *weak* when most of the reactant mixture is consumed by deflagrative front propagation.

Table 2.1: Initial conditions for parametric cases

Set #	P_0 (atm)	T_0 (K)	T' (K)	L (cm)
1	20	910-1100	10	1.2
2	10	910-1100	10	1.2
3	10	910-1100	10	2.4

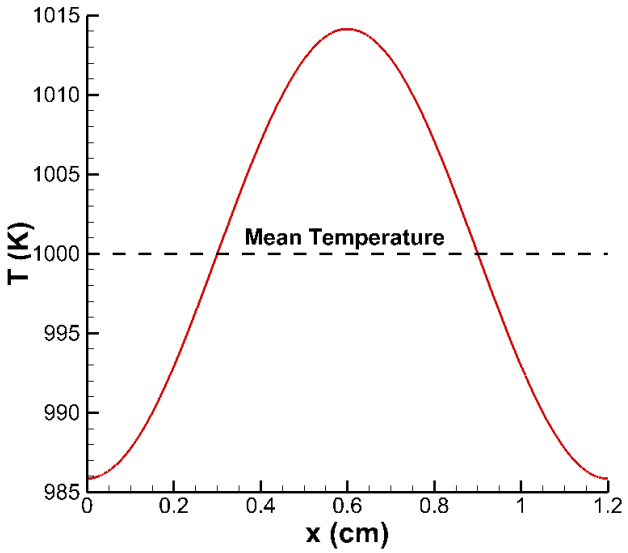

(a)

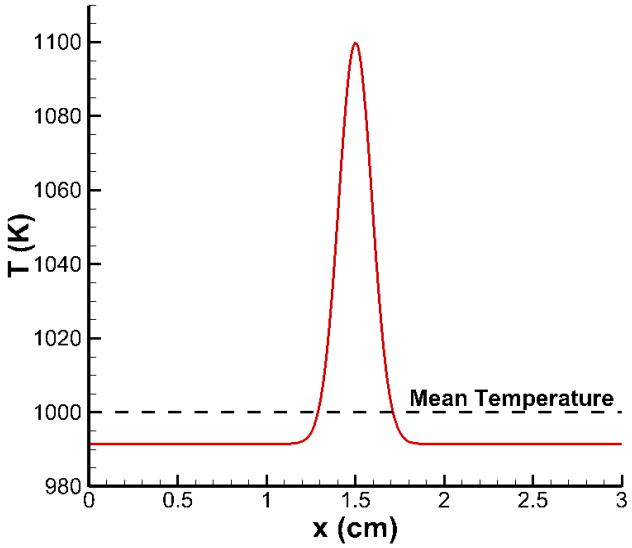

(b)

Figure 2.1: Sample initial temperature profiles with (a) global temperature gradient (T' = 10 K, L = 1.2 cm) and (b) local hot spot (ΔT = 100 K), at T_0 of 1000 K.

2.2 Effects of global temperature variations

2.2.1 Strong ignition limit: The Sankaran number

To investigate the effect of global temperature variations, parametric tests are carried out at different thermodynamic conditions, for varying magnitudes of the RMS temperature fluctuation (T') and the associated wavelength (L), as listed in Table 2.1. The corresponding homogeneous ignition delay times ($\tau_{ig,0}$), laminar flame speeds (S_L), and temperature sensitivities of ignition delay ($|d\tau_{ig,0}/dT_0|$) at the mean initial conditions considered in the present work are plotted in Figures 2.2(a) and 2.2(b), respectively. The ignition delay time is defined as the time at which the maximum pressure rise rate occurs. Note that S_L decreases, whereas both $\tau_{ig,0}$ and $|d\tau_{ig,0}/dT_0|$ increase with a decrease in temperature, at a given pressure.

Figure 2.3 shows typical behavior of temperature evolution for the overall progression of the ignition and combustion process for T_0 = 1030 K and T' = 10 K, corresponding to set #1. Ignition first occurs at the location of the highest temperature in the middle of the domain, and subsequently reaction fronts emanate from this ignition kernel, propagating towards the left and right ends of the domain. The propagating fronts heat the remaining charge by compression, thereby accelerating the ignition of the end-gas. Similar to Figure 2.3, for all other parametric cases listed in Table 2.1, the reactant mixture is completely consumed by ignition front propagation.

To determine the nature of the propagating front, the numerical results for the parametric cases are analyzed based on two quantitative metrics. The first metric to distinguish between deflagrations and spontaneous propagation fronts is the density-weighted front propagation speed [94, 95], S_d, defined as:

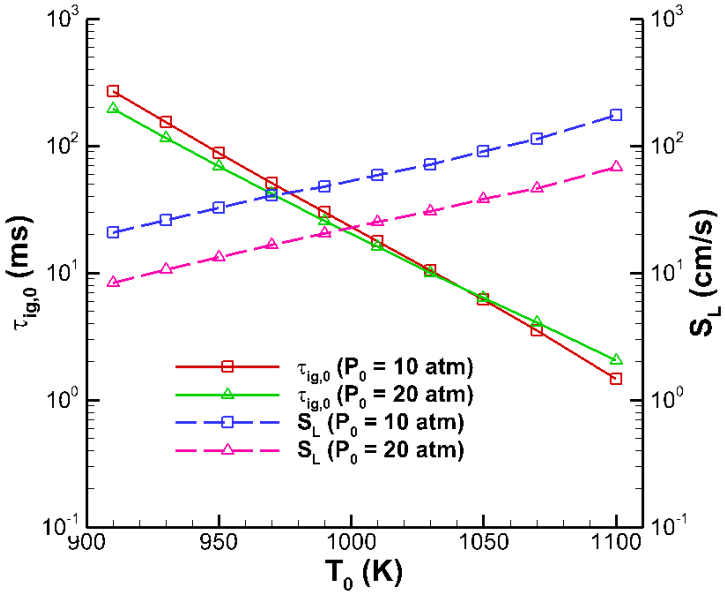

(a)

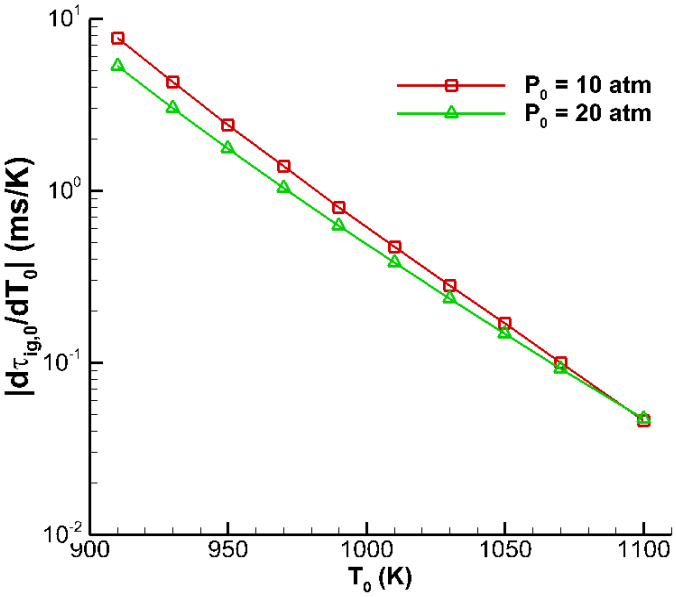

(b)

Figure 2.2: (a) Homogeneous ignition delay and laminar flame speed versus initial mean temperature and (b) ignition delay sensitivity versus initial mean temperature, for all cases listed in Table 2.1.

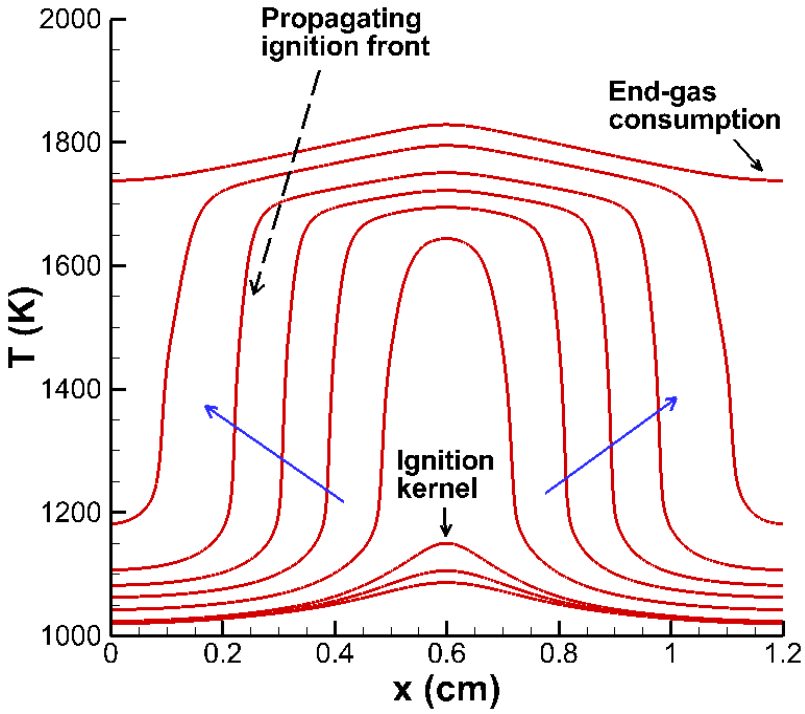

Figure 2.3: Temperature versus distance for a sequence of times, for T_0 = 1030 K, corresponding to set #1 in Table 2.1. The equally spaced time sequence starts from 7 ms with an increment of 0.25 ms. Arrows indicate the direction of increasing time.

$$S_d = \frac{1}{\rho_u |\nabla Y_k|}\left(\dot{w}_k - \frac{\partial}{\partial x_j}\left(\rho Y_k V_{j,\mathrm{k}}\right)\right) \tag{2.2}$$

where Y_k, $V_{j,k}$ and $\dot{w}_k$ denote species mass fraction, species diffusion velocity in the j-direction, net production rate of species k, and ρ_u denotes the density of the unburned mixture, which is calculated from the local enthalpy and fresh reactant mixture condition based on the assumptions of constant pressure and enthalpy across the front [71]. S_d is computed at the location of maximum heat release and H_2 is chosen as the species k in the present work.

As the second metric to identify the nature of the propagating fronts, the reaction and diffusion budgets for the H_2 mass fraction at the time of minimum front propagation speed are examined. A characteristic front

Damköhler number (Da_{fr}) is defined as the ratio of the peaks of reaction and diffusion of H_2 within the front:

$$Da_{fr} = \frac{\max(|\dot{w}_{H_2}|)}{\max(\nabla.(-\rho D_{H_2} \nabla Y_{H_2}))} \tag{2.3}$$

where the maximum values for the reaction and diffusion terms closest to the reaction zones are considered. H_2 is used for the calculations in the present study; it was found that the choice of other species such as OH and HO_2 yielded consistent results.

Figure 2.4(a) shows the computed temporal evolution of the front speed for two initial mean temperatures of 910 K and 1030 K, corresponding to set #1 in Table 2.1. The x-axis and y-axis are normalized by the homogeneous ignition delay times ($\tau_{ig,0}$) and laminar flame speeds (S_L) respectively, at the corresponding initial mean conditions. Nominally, the curves exhibit a characteristic U-shape behavior, representing a stabilized low speed front propagation between the initial ignition kernel development and final consumption points where the speed becomes unbounded due to nearly zero fuel concentration gradient [71]. For T_0 = 910 K, S_d is almost equal to the laminar flame speed, whereas for T_0 = 1030 K, the ignition front propagates at a speed higher than the corresponding S_L by an order of magnitude. The final thermal runaway also occurs relatively faster for the lower T_0 case.

Figure 2.4(b) shows the spatial profiles of the diffusion and reaction terms in the H_2 species conservation equation for the two cases. As the configuration is symmetric, only the right half of the domain is shown. The time instants correspond to the minimum front propagation speed for the respective cases. For T_0 = 1030 K, the diffusion term is nearly negligible relative to the reaction term. On the other hand, for T_0 = 910 K, the two contributions are comparable. Figure 2.4 indicates that the higher

temperature case exhibits spontaneous ignition behavior whereas for the lower temperature case, auto-ignition occurs via deflagrative front propagation.

The variation of Da_{fr} with T_0 for the three parametric sets listed in Table 2.1 is plotted in Figure 2.5 to capture the trend in auto-ignition behavior. As T_0 decreases, transport effects become more important and the ignition regime transitions from spontaneous (strong) propagation to deflagration (weak), indicated by the Da_{fr} approaching unity.

As an alternative metric to identify the nature of the front, the Zel'dovich-Sankaran criterion [32] predicts that strong ignition is encountered when:

$$\mathrm{Sa} = \beta \frac{S_L}{S_{sp}} = \beta S_L \left| \frac{d\tau_{ig,0}}{dT_0} \frac{dT_0}{dx} \right| \leq 1 \tag{2.4}$$

where Sa is called the Sankaran number and $S_{sp} = \left| \left(d\tau_{ig,0} / dT_0 \right) \cdot \left(dT_0 / dx \right) \right|^{-1}$ is the speed of a spontaneous ignition front. dT_0/dx represents the initial temperature gradient in the mixture. β is chosen to be 0.5 following Ref. [32].

The variation of Sa with T_0 for the different parametric sets is also shown in Figure 2.5. The data shows the Sa = 1 criterion coincides well with $Da_{fr} \approx$ 1.4, which is a reasonable indicator to identify deflagrative fronts. For β in the range of 0.3-0.9, the strong ignition limit corresponding to Sa = 1 computed for each parametric set shifts by a maximum of $|\Delta T_0|$ = 20 K about the value computed for β = 0.5 and the corresponding Da_{fr} varied in the range 1.1-1.8, which is again a good indicator of deflagrative front propagation. This demonstrates that Equation (2.4) can serve as an appropriate non-dimensional criterion to predict the ignition regime. The magnitude of Sa quantitatively represents the net effect of chemistry, thermo-physical properties of the mixture and system-specific thermal characteristics on the auto-ignition behavior.

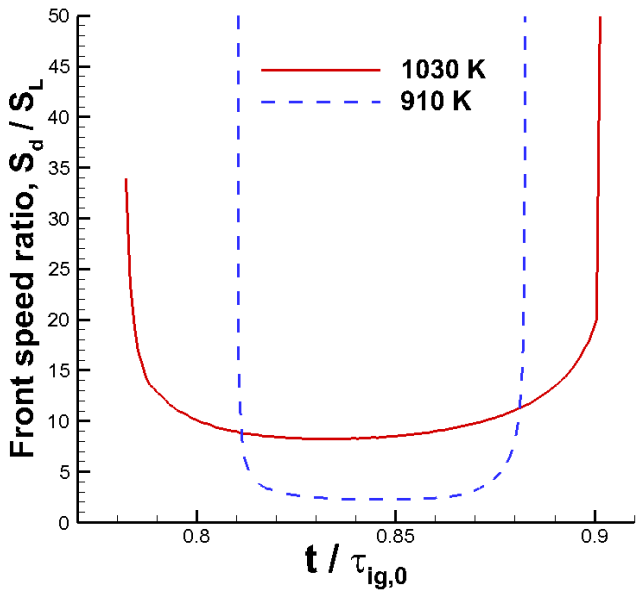

(a)

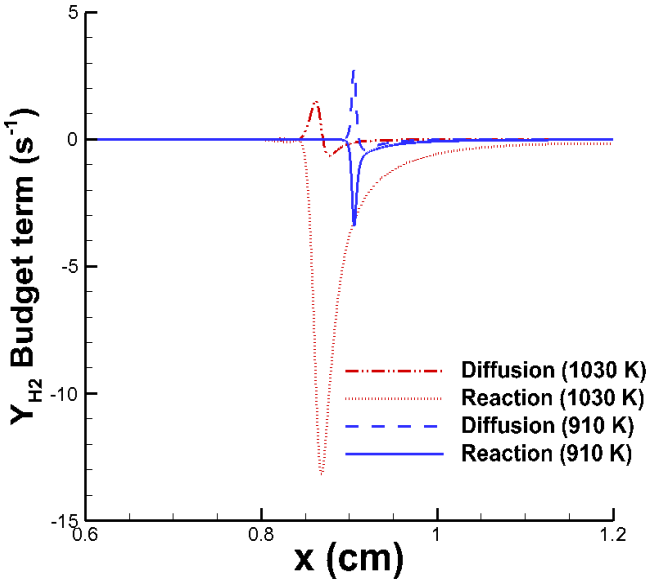

(b)

Figure 2.4: (a) Evolution of normalized front propagation speed as a function of normalized time, and (b) hydrogen reaction and diffusion budget terms at the time instant of lowest front propagation speed, for T_0 = 1030 K (red) and T_0 = 910 K (blue), corresponding to set #1 in Table 2.1.

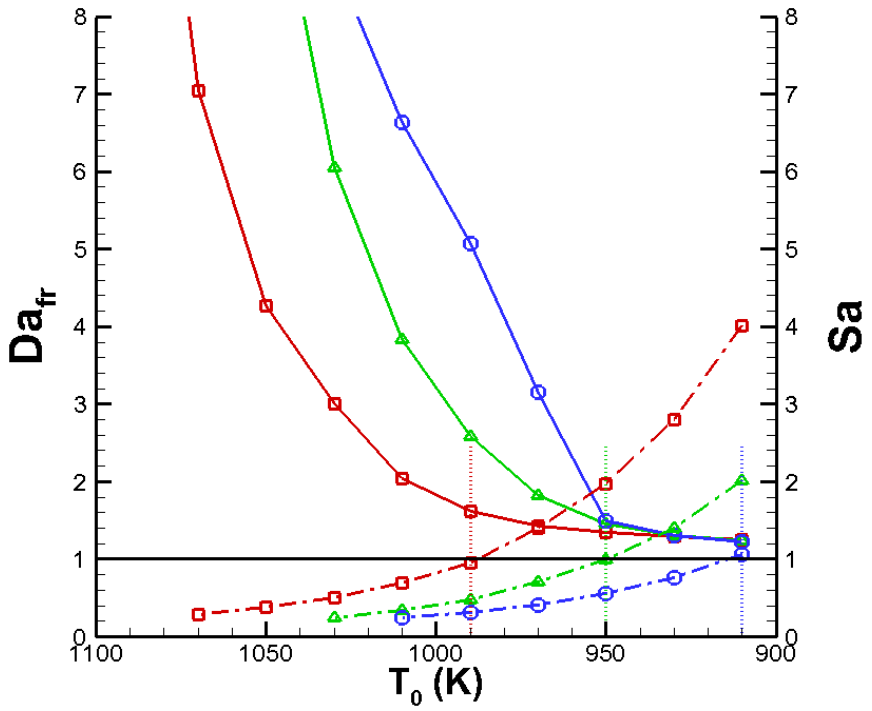

Figure 2.5: Variation of front Damköhler number (solid lines) and Sankaran number (dash-dot lines) versus initial mean temperature (T_0) for parametric set #1 (circles), parametric set #2 (squares) and parametric set #3 (Δ's) in Table 2.1. The dotted lines show the corresponding T_0 at which Sa = 1 for each parametric set.

2.2.2 Role of passive scalar mixing

In addition to transport within the flame front, the effect of diffusive transport can also modify the ignition characteristics. For example, rapid turbulent mixing within the bulk mixture may dissipate local temperature peaks before they can act as ignition kernels leading to front propagation. The impact of passive scalar mixing on auto-ignition can be quantified by the mixing Damköhler number (Da_{mix}) defined as:

$$\mathrm{Da}_{mix} = \tau_{mix} / \tau_{ig,10\%} \tag{2.5}$$

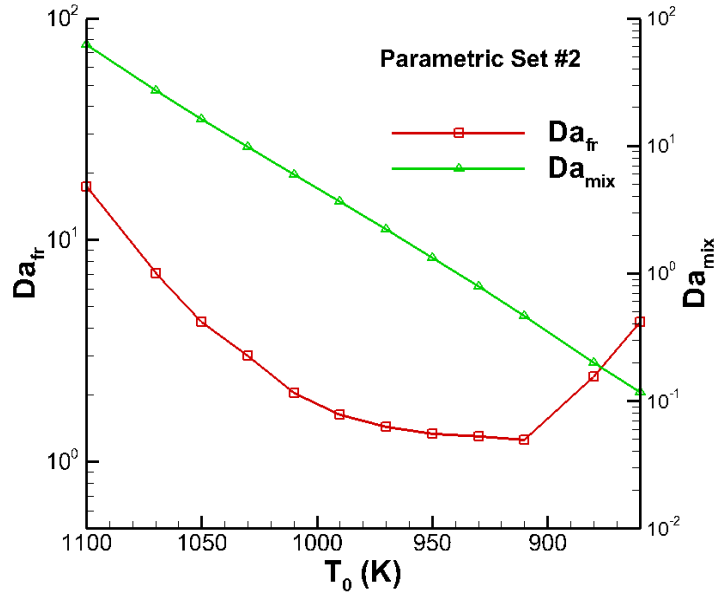

(a)

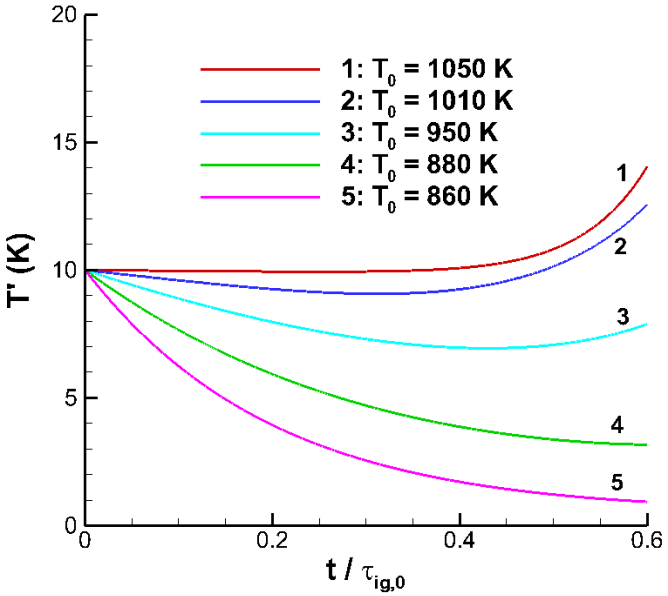

(b)

Figure 2.6: (a) Variation of the front and mixing Damköhler numbers as a function of the initial mean temperature, and (b) temporal evolution of temperature fluctuation for different initial mean temperatures, corresponding to parametric set #2 in Table 2.1.

where τ_{mix} is the mixing time scale determined by

$$\tau_{mix} = \frac{T''^2}{2\alpha_0 \left|\nabla T_0\right|^2} \tag{2.6}$$

and $\tau_{ig,10\%}$ represents the shortest ignition time scale of the initial mixture [55] and is defined as the homogeneous ignition delay time at the temperature $T_{\min} + 0.9\left(T_{\max} - T_{\min}\right)$, where $T_{\min}$ and $T_{\max}$ are the minimum and maximum initial temperatures in the domain. α_0 denotes the thermal diffusivity at the initial bulk thermodynamic conditions.

When the Da_{mix} becomes less than O(1), the passive scalar dissipation effects are expected to become important. To substantiate this hypothesis, the parametric set #2 in Table 2.1 is further expanded to include lower T_0 values at 880 and 860 K. The variation of the front and mixing Damköhler numbers with the initial mean temperature is shown in Figure 2.6(a). For T_0 < 910 K, as Da_{mix} becomes much lower than unity, Da_{fr} begins to increase, indicating a shift in the ignition regime from deflagration to spontaneous ignition. The time evolution of the temperature fluctuation (T'') for a few parametric cases is shown in Figure 2.6(b). It is observed that the temperature fluctuations dissipate more significantly at lower T_0, as the mixing time scale becomes shorter relative to the reaction time scale, promoting strong ignition at sufficiently low initial mean temperatures and leading to non-monotonic ignition trend as depicted in Figure 2.6(a).

Note that such a rapid scalar mixing scenario has not been observed in previous shock tube and RCF experiments [16] at lower temperatures. The present discussion of global temperature fluctuations applies to the conditions in which the temperature fluctuations are directly correlated with turbulent flows [51]. In the nearly quiescent conditions as encountered in shock tubes and RCF, local thermal stratification or hot spots are considered

the primary mechanism to trigger an early ignition and flame propagation. As such, the representative temperature gradient used in Equation (2.4) must be determined in a different way, which subsequently suppresses the possibility of $Da_{mix} < 1$ observed in Figure 2.6(a). The characteristics of ignition caused by localized ignition sources are studied in the following section.

2.3 Effects of local hot spots

In this section, the influence of temperature inhomogeneities as highly localized temperature gradients, representing "hot spots", on syngas auto-ignition characteristics are investigated. Parameters of interest are (a) the hot spot strength (ΔT) for a given T_0, and (b) T_0 for a fixed value of ΔT. Details of the numerical setup are described in Section 2.1.

Figure 2.7 shows the temporal evolution of the temperature field for T_0 = 910 K, P_0 = 20 atm, with two different hot spot strengths at (a) ΔT = 25 K and (b) 100 K. For both cases, an ignition kernel first develops at the center of the domain, leading to front propagation, followed by the end-gas auto-ignition. Temporal evolution of the corresponding front Damköhler numbers is shown in Figure 2.8. The pressure remains spatially uniform and varies with time only. For both cases, $Da_{fr} \approx 1.15$ at the minimum plateau condition indicating that the fronts are deflagrative in nature. Therefore, instead of Da_{fr}, percent mass fraction burned by deflagration is employed to investigate the relative importance of deflagration versus end-gas self-ignition. It can be seen that the ignition front develops much earlier and travels much further into the unburned mixture for ΔT = 100 K. As a result, the mass fraction burned by deflagration is found to be much higher for ΔT = 100 K ($\approx 68\%$) as compared to that for ΔT = 25 K ($\approx 33\%$).

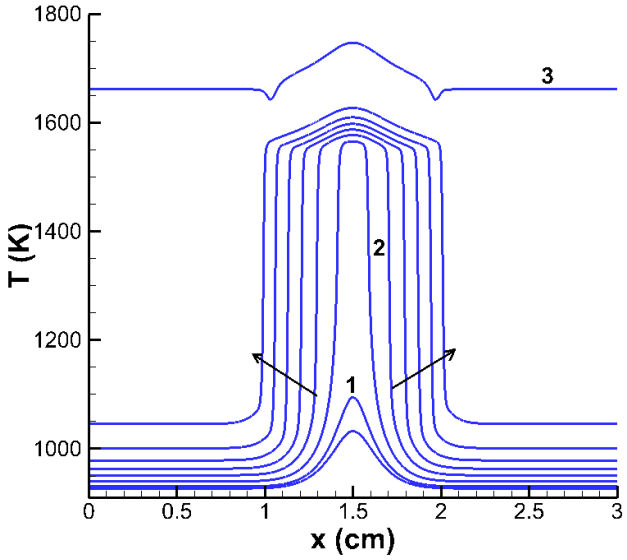

(a)

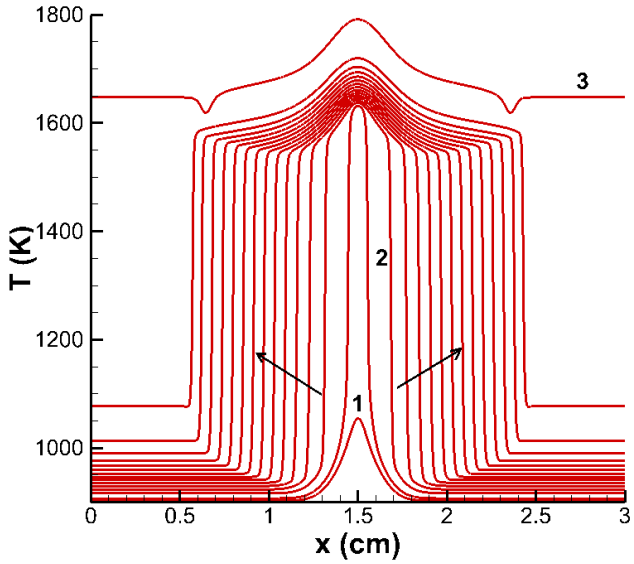

(b)

Figure 2.7: Temporal evolution of the temperature profiles during ignition for T_0 = 910 K, P_0 = 20 atm: (a) ΔT = 25 K starting at 146 ms. (b) ΔT = 100 starting at 24 ms, shown at an equal time increment of 4 ms. Arrows indicate the direction of increasing time. Numbers denote the ignition kernel (1), propagating front (2) and the end-gas auto-ignition (3) phase.

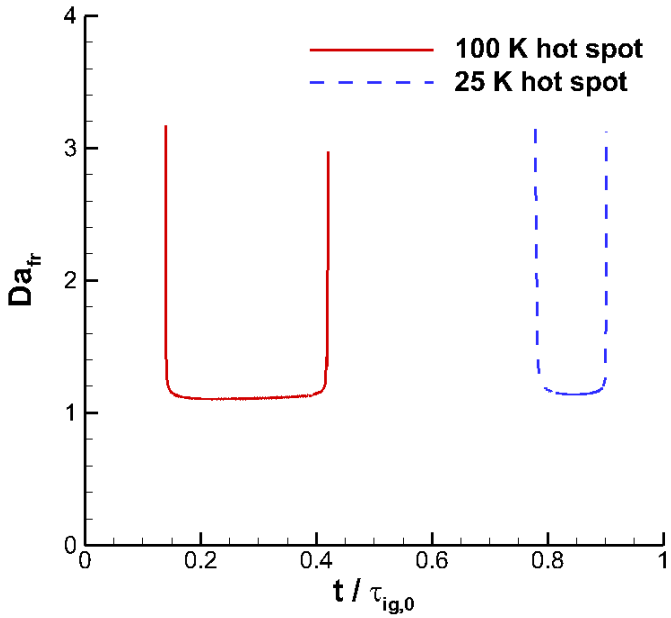

Figure 2.8: Front Damköhler number versus time (normalized by homogeneous ignition delay time at the mean initial mixture conditions) for ΔT = 25 K and ΔT = 100 K; T_0 = 910 K and P_0 = 20 atm.

To further investigate the effect of the strength of the hot spot, Figure 2.9 shows the evolution of (a) the mean and (b) end-gas temperature for T_0 = 910 K and with ΔT ranging from 25 to 100 K. The time axis is normalized by $\tau_{ig,0}$, which is identical for all cases. As ΔT increases, the front propagation mode becomes more prominent (as shown in Figure 2.7), and the overall ignition delay time decreases. The earlier front establishment also leads to an earlier rise in the end-gas temperature as shown in Figure 2.9(b).

The hot spot ignition cases are now tested for the validity of the Zel'dovich-Sankaran criterion. Since Equation (2.4) is based on the bulk temperature gradient of the system, for the hot spot ignition condition a representative temperature gradient is defined as based on the initial root-mean-square (RMS) temperature and half of the domain size ($L/2$), similar to section 2.2.1. Table 2.2 shows the mass fraction burned by deflagration and the computed Sankaran numbers for the four cases under study. It is clearly

seen that Sa increases with increasing ΔT, thus capturing the quantitative contributions of the deflagrative front propagation in the overall ignition behavior. For ΔT = 100 K, *Sa* nearly reaches unity, at which a large fraction of the reactant mixture (nearly 70%) is consumed by the flame front. In addition to the test cases discussed above, additional parametric tests were also performed by varying the domain size for fixed ΔT and hot spot shape (not shown here). It was still observed that *Sa* = 1 coincided with a mass fraction burned by deflagration in the range 60-70%. This indicates that the Zel'dovich-Sankaran criterion serves as a rational predictive criterion for identifying the transition from strong to weak ignition regime and provides a quantitative estimate of the significance of the deflagration mode on the overall ignition characteristics. Note that passive scalar dissipation plays a negligible role here, as Da_{mix} for all parametric cases are found to be greater than unity.

Table 2.2: Mass fraction burned by deflagration and Sankaran numbers for different parametric cases (T_0 = 910 K, P_0 = 20 atm)

ΔT (K)	Mass fraction burned by deflagration (%)	Sa
25	33	0.24
50	38	0.48
75	48	0.72
100	68	0.96

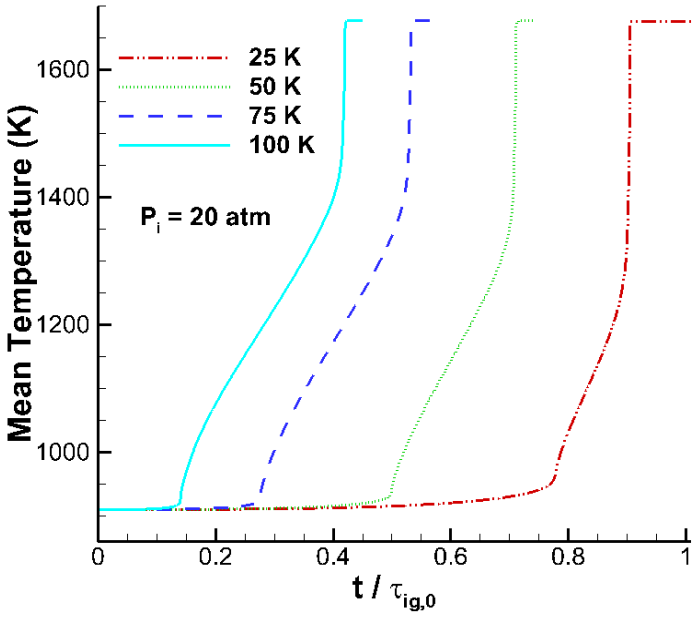

(a)

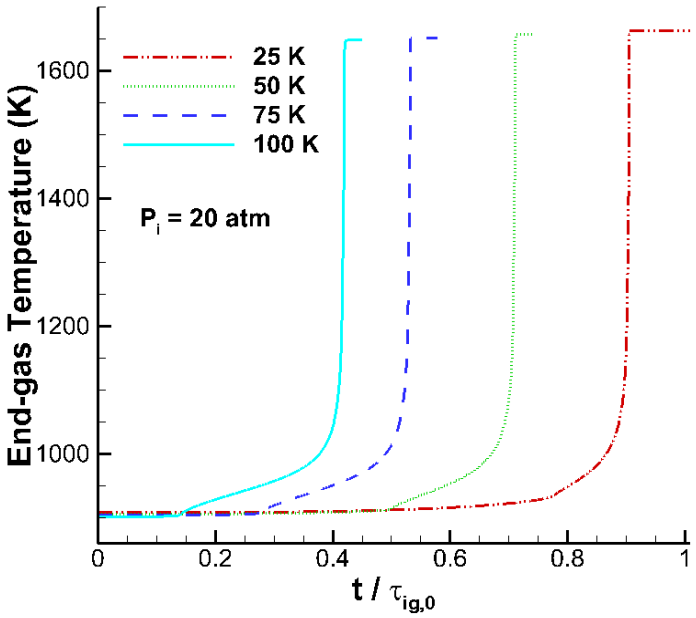

(b)

Figure 2.9: Evolution of (a) the mean and (b) end-gas temperature versus time (normalized by homogeneous ignition delay time at T_0), for different values of ΔT; T_0 = 910 K and P_0 = 20 atm.

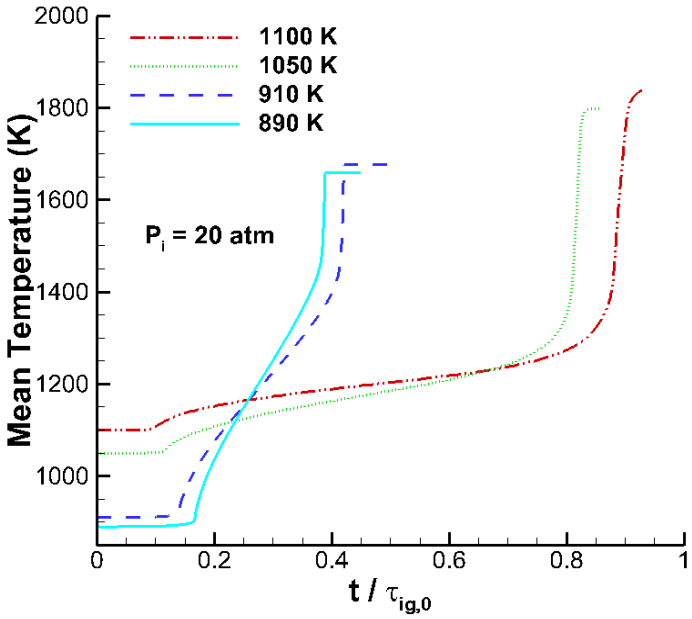

(a)

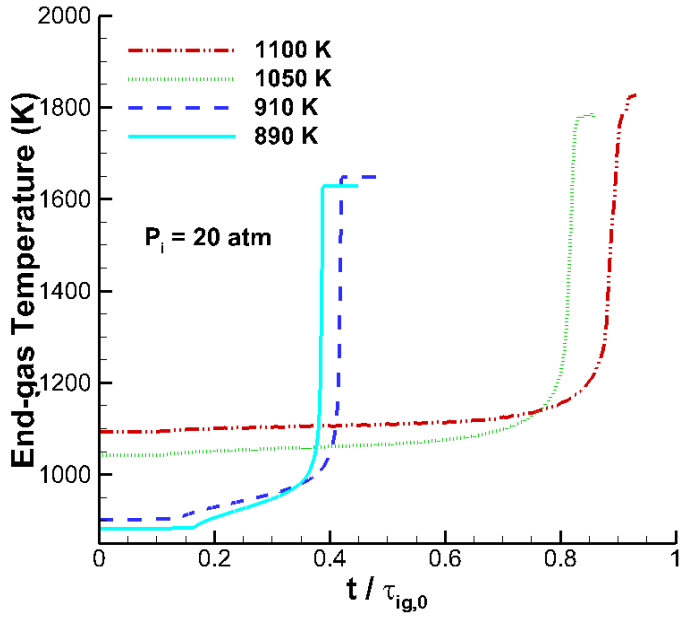

(b)

Figure 2.10: Evolution of (a) mean temperature and (b) end-gas temperature, versus time (normalized by homogeneous ignition delay time at the mean initial mixture conditions), for different magnitudes of T_0; ΔT = 100 K and P_0 = 20 atm.

The final set of the parametric study is carried out by varying T_0 from 890 to 1100 K, for fixed P_0 = 20 atm and ΔT = 100 K. Although not shown here, it is observed that the propagating reaction front is in the deflagrative regime for all cases considered, similar to Figure 2.8. Table 2.3 summarizes the corresponding mass fractions burned by deflagration and the corresponding Sankaran numbers. Based on the values of the mass fraction burned by deflagration, it is concluded that strong ignition is encountered for T_0 = 1100 K and 1050 K, whereas weak ignition occurs at lower T_0 = 910 K and 890 K. Again, the Zel'dovich-Sankaran criterion properly captures the ignition characteristics. The evolutions of mean and end-gas temperatures for these cases are shown in Figures 2.10(a) and 2.10(b), respectively. The weak ignition regime results in significantly advanced ignition as compared to its homogeneous counterpart.

Table 2.3: Mass fraction burned by deflagration and Sankaran numbers for different parametric cases (ΔT = 100 K, P_0 = 20 atm)

T_0 (K)	Mass fraction burned by deflagration (%)	Sa
1100	33	0.06
1050	38	0.12
910	48	0.96
890	73	1.82

The overall parametric effects for combinations of the variations in T_0 and ΔT are summarized in Figure 2.11, where the normalized ignition delay time is plotted versus T_0 for different magnitudes of ΔT. In addition to the hot spot profiles, a global temperature gradient of 5 K/mm (similar to set #1 in Table

2.1) is also superimposed on the initial mean temperature. It is clearly observed that the sensitivity of auto-ignition phenomena to temperature inhomogeneities increases as the initial bulk temperature is lowered, leading to greater advancement in the net ignition delay time. As shown earlier, this trend directly reflects the transition from strong to weak ignition regime, resulting in greater influence of deflagrative front propagation. These findings are qualitatively in agreement with recent experimental findings based on detailed optical visualizations [24].

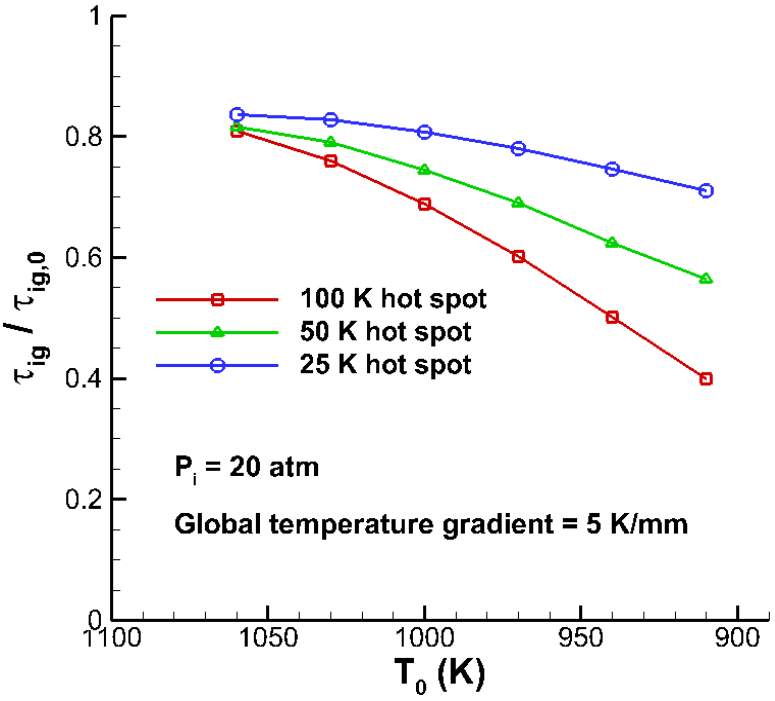

Figure 2.11: Variation of ignition delay timing (normalized by the homogeneous ignition delay at the corresponding initial mean temperature) with initial mean temperature for different hot spot strengths.

As a final remark, although the focus of the present work is on syngas auto-ignition, the Zel'dovich-Sankaran criterion is applicable to any reactant

mixture in general, with known homogeneous ignition characteristics and deflagration front propagation speed.

2.4 Concluding remarks

Auto-ignition characteristics of syngas fuel at high-pressure and low-temperature conditions were investigated via one-dimensional numerical simulations with detailed chemical kinetics and transport properties. Parametric tests were carried out over a wide range of thermodynamic conditions to study the effects of temperature inhomogeneities represented by global temperature gradients and localized hot spots. Front propagation speed and front Damköhler number analyses allowed detailed description of the propagating ignition front. It was observed that auto-ignition became more sensitive to the presence of temperature fluctuations as the bulk temperature was lowered, resulting in a transition from strong to weak ignition regime, accompanied by enhanced deflagrative front propagation. A larger strength of the hot spot was found to amplify the effects of weak ignition. Furthermore, the prevalence of weak ignition was found to yield a significant advancement of the net ignition delay time as compared to the corresponding homogeneous model predictions, by promoting end-gas compression-heating.

When the bulk mixture was not highly reactive, it was also observed that passive scalar dissipation could lead to very fast dissipation of the temperature fluctuations, when the mixing Damköhler number became much less than unity, thereby promoting strong ignition at sufficiently low temperatures. However, this effect was important only in case of global temperature gradients, and not for local hot spots.

The numerical results were used to validate the Zel'dovich-Sankaran criterion, which takes into consideration the interplay of chemical kinetics, thermo-physical properties and device-dependent thermal characteristics, as a predictive metric to identify ignition regimes. It was demonstrated that Sa = 1 adequately captures the boundary between the weak and strong ignition regimes. Furthermore, the relative magnitude of the Sankaran number translates accurately to the quantitative strength of the deflagration front in the overall ignition advancement.

In the next chapter, extension of the Zel'dovich-Sankaran and scalar mixing criteria to turbulent conditions will be carried out, leading to an ignition regime diagram.

Chapter 3
Regime Diagram for Auto-ignition of Homogeneous Reactant Mixtures with Turbulent Velocity and Temperature Fluctuations

In this Chapter, a theoretical scaling analysis is conducted to propose non-dimensional criteria to predict weak and strong ignition regimes for a compositionally homogeneous reactant mixture with turbulent velocity and temperature fluctuations. This leads to a regime diagram that provides guidance on expected ignition behavior based on the thermo-chemical properties of the mixture and the flow/scalar field conditions. The analysis extends the original Zel'dovich's theory by combining the turbulent flow and scalar characteristics in terms of the turbulent Damköhler and Reynolds numbers of the system, thereby providing unified and comprehensive understanding of the physical and chemical mechanisms controlling auto-ignition.

3.1 Problem definition and assumptions

Figure 3.1 shows a schematic of the problem under consideration and important characteristic quantities. The length scales include the chamber length, L, the integral eddy scale, ℓ, the Taylor microscale, λ, and the deflagration flame thickness, δ_f. In general, ℓ is considered a fraction of L, and λ/ℓ scales with the turbulent Reynolds number as will be discussed

later in section 3.2. The laminar flame speed, S_L, and the RMS turbulent velocity fluctuation at the integral scale, u', are important velocity scales that will be compared to the other relevant velocities to be determined later. For the scaling analysis, the following simplifications and assumptions are made:

1. Weak ignition is primarily caused by front propagation originating from small scale local temperature fluctuations, with a length scale typically of an order of 1 mm or less, such as local hot spots, and the effects of large scale bulk temperature gradients, such as gradients caused by wall heat losses, are not considered. This is based on the experimental observations that early stage ignition kernels are often generated in the interior of the combustor, not necessarily near the wall region.
2. The mixture composition is homogeneous, and only the temperature fluctuations are considered. Moreover, the scales of initial temperature and velocity fluctuations are comparable.
3. The Prandtl number of the mixture is unity so that combined with assumption 2, the dissipation of temperature fluctuations is mainly driven by turbulent flows. This implies that the time and length scales for turbulent velocity and scalar fields are the same (i.e. the Batchelor scale is identical to the Kolmogorov scale).

To characterize the turbulent velocity and scalar fields, key non-dimensional parameters are introduced. Following the framework of Liñán and Williams [96], a rational way to characterize turbulent combustion systems is to use the turbulent Reynolds number, which represents the intensity of turbulence, and the characteristic turbulent Damköhler number, which represents the relative intensity of chemical reaction. For the integral

scale eddy whose velocity, length, and time scales are characterized by u', ℓ, $\tau_\ell = \ell / u'$, respectively, the turbulent Reynolds number is defined as:

$$\mathrm{Re}_\ell = \frac{u'\ell}{\nu} \tag{3.1}$$

where ν is the kinematic viscosity of the bulk mixture gas. As for the measure of the chemical intensity, two ignition Damköhler numbers are defined as:

$$\mathrm{Da}_\ell = \frac{\tau_\ell}{\tau_{ig}} \tag{3.2}$$

which is referred to as the *integral* Damköhler number, and

$$\mathrm{Da}_\lambda = \frac{\tau_{\lambda_T}}{\tau_{ig}} \tag{3.3}$$

is referred to as the *mixing* Damköhler number, where τ_{ig} is the ignition delay time for the homogeneous reactant mixture at the bulk temperature, τ_{λ_T} is the mixing time scale associated with the Taylor microscale for the temperature field, λ_T. The mixing time scale and the Taylor microscale which are determined in terms of the RMS temperature fluctuation, T', and the mean temperature dissipation rate, $2\alpha\widetilde{|\nabla T|^2}$, written as:

$$\tau_{\lambda_T} = \frac{T'^2}{\alpha\widetilde{|\nabla T|^2}},\ \lambda_T^2 = \frac{T'^2}{\widetilde{|\nabla T|^2}} \tag{3.4}$$

in analogy with those of the Taylor microscales for velocities:

$$\tau_\lambda = \frac{u'^2}{\nu\overline{\left|\partial u_j / \partial x_j\right|^2}},\ \lambda^2 = \frac{u'^2}{\overline{\left|\partial u_j / \partial x_j\right|^2}} \tag{3.5}$$

Based on assumption 3, it follows that the mixing time and length scales for temperature are interchangeable with those for turbulent velocities, such that:

$$\tau_{\lambda_T} = \tau_\lambda,\ \lambda_T = \lambda \tag{3.6}$$

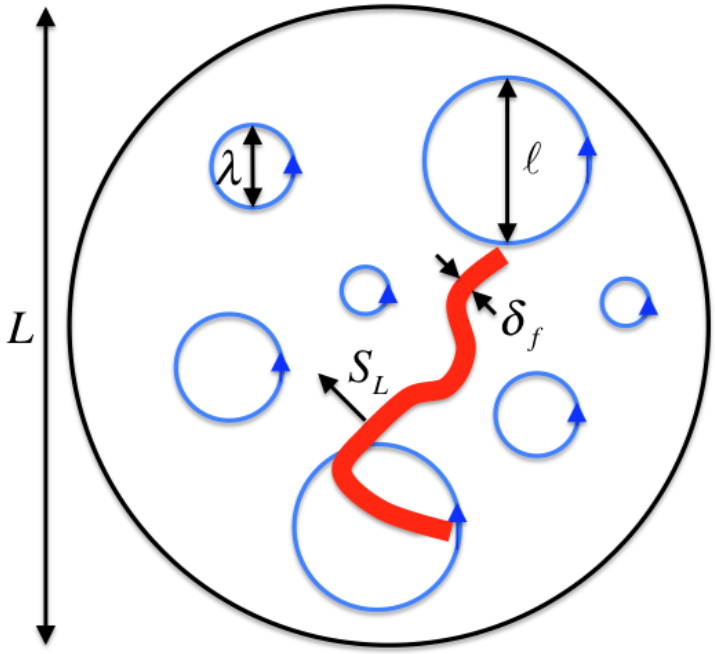

Figure 3.1: A schematic of a combustion chamber with various physical length scales.

3.2 Scaling analysis

The main objective of the scaling analysis is to derive an expression for the Zel'dovich-Sankaran criterion in terms of the characteristic Reynolds and Damköhler numbers. According to the theory of homogeneous isotropic turbulence [97], the scaling relation yields:

$$\frac{\lambda}{\ell} = \mathrm{Re}_\ell^{-1/2}, \frac{\tau_\lambda}{\tau_\ell} = \frac{\lambda / u'_\lambda}{\ell / u'} = \frac{\lambda}{\ell}\frac{u'}{u'_\lambda} = \left(\frac{\lambda}{\ell}\right)^{2/3} = \mathrm{Re}_\ell^{-1/3} \tag{3.7}$$

It follows that

$$\mathrm{Da}_\lambda = \frac{\tau_{\lambda_T}}{\tau_{\mathrm{ig}}} = \frac{\tau_\lambda}{\tau_{\mathrm{ig}}} = \frac{\tau_\ell}{\tau_{\mathrm{ig}}}\frac{\tau_\lambda}{\tau_\ell} = \mathrm{Da}_\ell \mathrm{Re}_\ell^{-1/3} \tag{3.8}$$

The significance of Da_λ is that it is the ratio of the characteristic temperature dissipation time to the characteristic ignition delay time at the bulk mean temperature. Therefore, if $\mathrm{Da}_\lambda < 1$, the temperature fluctuations are dissipated before ignition occurs, thus the system is unlikely to exhibit the weak ignition behavior triggered by reaction front propagation.

The next step is to extend the Zel'dovich-Sankaran criterion, Equation (2.4), to turbulent conditions. To this end, it is assumed that the occurrence of the hot-spot-induced pre-ignition is proportional to the statistical mean temperature gradient, such that

$$\mathrm{Sa} \approx \beta S_L \left|\frac{d\tau_{ig}}{dT}\right| \widetilde{|\nabla T|} \tag{3.9}$$

where it is estimated that

$$\widetilde{|\nabla T|} \approx \frac{T'}{\lambda_T} \approx \frac{T'}{\lambda} = \frac{T'}{\ell \mathrm{Re}_\ell^{-1/2}} \tag{3.10}$$

Therefore, Equation (3.9) is written as:

$$\mathrm{Sa} \approx \beta S_L \left| \frac{d\tau_{ig}}{dT} \right| \frac{T'}{\ell} \mathrm{Re}_\ell^{1/2} = \beta \left(\frac{S_L}{\delta_f} \right) \left(\frac{\delta_f}{\ell} \right) T' \left| \frac{d\tau_{ig}}{dT} \right| \mathrm{Re}_\ell^{1/2} \tag{3.11}$$

which includes the length scale ratio, δ_f / ℓ where δ_f is the characteristic flame thickness. Following Liñán and Williams [96]:

$$\frac{\delta_f}{\ell} = \mathrm{Re}_\ell^{-1/2} \mathrm{Da}_{\ell,f}^{-1/2} = \mathrm{Re}_\ell^{-1/2} \left(\frac{\tau_\ell}{\tau_f} \right)^{-1/2} = \mathrm{Re}_\ell^{-1/2} \left(\frac{\tau_\ell}{\tau_{ig}} \right)^{-1/2} \left(\frac{\tau_{ig}}{\tau_f} \right)^{-1/2}$$

$$\frac{\delta_f}{\ell} = \mathrm{Re}_\ell^{-1/2} \mathrm{Da}_\ell^{-1/2} \left(\frac{\tau_{ig}}{\tau_f} \right)^{-1/2} \tag{3.12}$$

where it is noted that the integral Damköhler number in Liñán and Williams [96] was defined differently from Equation (3.2) above, and was based on the flame time scale, $\tau_f = \delta_f / S_L$. Therefore, the factor τ_{ig} / τ_f must be included. Combining Equations (3.11) and (3.12), the turbulent ignition regime criterion can be written as:

$$\mathrm{Sa} = K \mathrm{Da}_\ell^{-1/2}, \; K = \beta \left(\frac{T'}{\left(\tau_f \tau_{ig} \right)^{1/2}} \right) \left| \frac{d\tau_{ig}}{dT} \right| \tag{3.13}$$

where *K* is referred to as the normalized thermal ignition sensitivity. In comparison with the laminar version in Equation (2.4), $S_L |\nabla T|$ has now been

expressed as $\left(T'/\tau^*\right)\mathrm{Da}_\ell^{-1/2}$ through the dimensional scaling, with a *reduced* time scale, $\tau^* = \left(\tau_f \tau_{ig}\right)^{1/2}$. The final ignition regime criterion becomes:

$$\begin{cases} \mathrm{Da}_\ell < K^2 : \text{ weak ignition} \\ \mathrm{Da}_\ell > K^2 : \text{ strong ignition} \end{cases} \tag{3.14}$$

As discussed with Equation (3.8), an additional condition of $\mathrm{Da}_\lambda = \mathrm{Da}_\ell \mathrm{Re}_\ell^{-1/3} > 1$ needs to be satisfied to ensure weak ignition, since otherwise the temperature fluctuations are likely to dissipate away before the front forms. Finally, $\mathrm{Da}_\ell < 1$ would ensure an even stronger mixing scenario, since eddies at all scales would have time scales shorter than the ignition delay time, such that all temperature fluctuations would be dissipated and only strong ignition would be expected.

3.3 The regime diagram and discussion

Compiling the above scaling analysis leads to the regime diagram as shown in Figure 3.2. The autoignition processes in nearly homogeneous mixtures with turbulent fluctuations are characterized in the Da-Re space, to represent the relative chemical and turbulence intensities determined by the chemistry, thermodynamics and turbulent transport in the gas mixture. It is shown that the primary factor to determine the ignition regime is Da_ℓ, while Re_ℓ modifies the conditions further.

First, for a given Re_ℓ, the Zel'dovich-Sankaran criterion indicates that the weak/mixed ignition regime is possible for $1 < \mathrm{Da}_\ell < K^2$. If $\mathrm{Da}_\ell > K^2$, when the reactant mixture is either too reactive (small τ_{ig}) or the mixture ignition

characteristics are not sensitive to the temperature fluctuations (small $d\tau_{ig}/dT$), such that the entire mixture ignites almost at the same time despite some level of temperature fluctuations. This is referred to as the *reaction-dominant* strong ignition regime. On the other hand, if $\mathrm{Da}_\ell < 1$, then the turbulent mixing is rapid (small τ_ℓ) such that the temperature fluctuations are dissipated before the local ignition takes place. In contrast to the $\mathrm{Da}_\ell > K^2$ case, this is referred to as the *mixing-dominant* strong ignition regime. Note that the *K* parameter includes the ignition delay sensitivity, which is more than just a time scale characterization, and depends strongly on the ignition chemistry of the specific fuel.

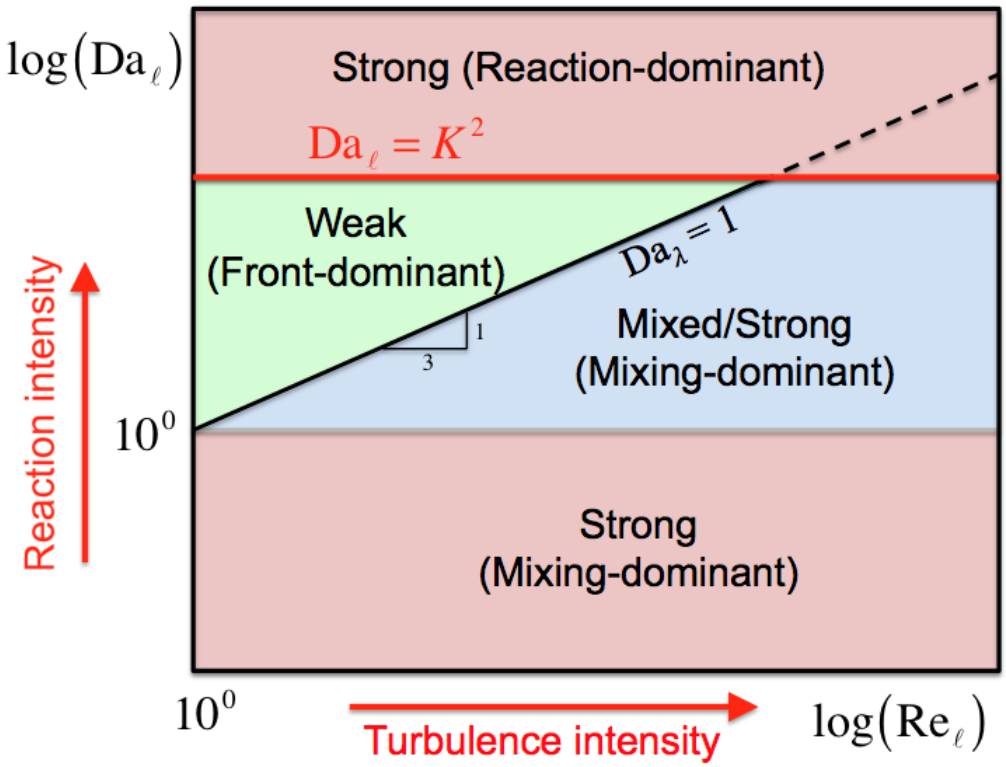

Figure 3.2: Regime diagram for strong and weak ignition for homogeneous mixture with turbulence and temperature fluctuations.

Between the limits $1 < \mathrm{Da}_\ell < K^2$, weak ignition is possible; however, the mixing Damköhler number, Da_λ, provides an additional criterion for this region of the regime diagram. Considering that the dynamics of turbulent mixing and dissipation is commonly characterized by the Taylor scale, λ, a proper criterion to determine the mixing-dominant strong ignition would be the ratio of the Taylor mixing time, τ_λ, to the ignition time, τ_{ig}. Therefore, the $\mathrm{Da}_\lambda = 1$ condition serves as a more refined criterion within the limits of $1 < \mathrm{Da}_\ell < K^2$ to further identify the boundary between the weak and strong ignition regimes. Considering Equation (3.8), this line appears on the regime diagram with a slope of 1/3, indicating that the occurrence of weak ignition phenomena will become less likely as the turbulent Reynolds number of the mixture increases. Still, the conditions between $\mathrm{Da}_\lambda < 1$ and $\mathrm{Da}_\ell > 1$ are a "grey" zone, in that some mixed mode ignition in which a mild level of front propagation followed by a strong ignition may occur. This is denoted as the *mixing-dominant mixed/strong* ignition regime.

The regime diagram serves as qualitative guidance to the expected ignition behavior. The appropriate auto-ignition regime can be identified given the knowledge of the thermo-chemical properties of the mixture (e.g. pressure, temperature, reaction chemistry, etc.), and the characteristic turbulent flow parameters (e.g. Reynolds number, turbulence/scalar fluctuation intensity, etc.). If the initial condition of the mixture falls into the weak ignition or mixed/strong ignition regimes, then large discrepancies in the ignition delay prediction against the measured data can be expected and must be treated carefully.

3.4 Concluding remarks

A theoretical scaling analysis was conducted to develop a regime diagram to predict weak and strong ignition regimes for a compositionally homogeneous reactant mixture with turbulent and temperature fluctuations. The diagram provides guidance on expected ignition behavior based on the thermo-chemical properties of the mixture and the flow/scalar field conditions. The analysis is an extension of the previous studies by Zel'dovich [31] and Sankaran et al. [32] to combine the turbulent flow and scalar characteristics in terms of the characteristic Damköhler and Reynolds numbers of the system. The results of this work provided a more unified and comprehensive understanding of the physical and chemical mechanisms controlling ignition characteristics compared to the existing experimental maps in previous studies [24, 28], which were solely based on the ignition delay sensitivity.

It was recognized that the Zel'dovich-Sankaran criterion includes the ignition delay sensitivity, $d\tau_{ig}/dT$, as a critical factor. Therefore, the traditional regime characterization based on the Damköhler and Reynolds numbers (such as those for turbulent premixed combustion regimes), which were based on time scales only, was not sufficient to describe the transitions between weak and strong ignition phenomena, and the introduction of the sensitivity parameter, *K*, was necessary. The regime diagram further showed how turbulence characteristics would affect the Zeldovich-Sankaran criterion based on the Kolmogorov's theory of homogeneous isotropic turbulence.

The Zel'dovich-Sankaran criterion indicates that there is a region where mixtures with high-*K* values or high thermal sensitivity are more susceptible to weak ignition. Such conditions are reached with hydrogen/oxygen mixtures at low temperatures and high pressures. Therefore, the theory serves as a reasonable argument that the ignition delay discrepancies observed in syngas

mixtures at low temperatures might be attributed to the ignition front propagation triggered by local temperature peaks.

In the next chapter, a parametric study is conducted employing 2D DNS, to provide numerical validation of the ignition regime diagram.

Chapter 4
Validation of turbulent ignition regime diagram

In this chapter, auto-ignition characteristics of compositionally homogeneous reactant mixtures in the presence of thermal non-uniformities and turbulent velocity fluctuations are computationally investigated. The main objectives are to identify the range of ignition and flame propagation behaviors and quantify the observed characteristics using non-dimensional analysis. 2D DNS of auto-ignition in a lean syngas/air mixture are performed at various parametric conditions. A number of parametric test cases, by varying the characteristic turbulent Damköhler and Reynolds numbers, are investigated. The high-fidelity simulations provide additional insight into the range of ignition behaviors that can be expected under high-pressure low-temperature conditions, and also provide numerical validation of the turbulent ignition regime diagram presented in chapter 3.

4.1 Numerical method and initial conditions

2D simulations are performed using the DNS code, S3D [86], which solves the compressible, Navier-Stokes, species and energy equations with higher order time integration and spatial discretization schemes [87]. The detailed H_2/CO mechanism with 12 species and 33 chemical reactions from Li et al. [88] is linked with CHEMKIN [89] and TRANSPORT [90] libraries for evaluating the reaction rates and thermodynamic and mixture-averaged

transport properties, respectively. Periodic boundary conditions were imposed in all directions to represent constant volume ignition.

A uniform syngas/air reactant mixture of equivalence ratio of 0.5, H_2:CO molar ratio of 0.7:1, an initial pressure of 20 atm, is chosen. In addition, the mixture is diluted with twice the amount of nitrogen present in the air, i.e., a molar ratio of N_2:O_2=11.28, to avoid shock wave formation [91, 92], which cannot be captured by the employed computational schemes at present.

Turbulent velocity fluctuations are superimposed on a stationary mean velocity field based on an isotropic kinetic energy spectrum function [98]. A similar random temperature spectrum, uncorrelated with the turbulent kinetic energy spectrum, is superimposed on a constant mean temperature field. In addition, a hot spot with a peak temperature of 100 K is superimposed on the temperature field in the form [32]:

$$T_{hs}(x,y) = \frac{A}{\pi}\exp\left[\frac{-2n^2((x-L/2)^2+(\mathrm{y}-L/2)^2)}{L^2}\right] - \frac{A}{2n^2} \qquad (4.1)$$

where L is the length of each side of a 2D square box domain, A = 450, n = 12 and (x, y) represents spatial location.

A total of eight DNS cases A-H are considered by varying initial mean temperature (T_0), most energetic turbulent length scale (ℓ_e) and u'. For the four different T_0 values of 1100, 1020, 990 and 970 K considered, the computed S_L values from PREMIX [99] simulations are 67.7, 27.8, 20.5, and 16.5 cm/s, respectively. L = 1.075 cm and 1.5 cm for cases A-E and F-H, respectively. Temperature fluctuation (T') is fixed at 15 K for all cases. The turbulence time scale is defined by $\tau_t = \ell_e / u'$. The most energetic length scales of velocity and the temperature fluctuations are the same for all cases. For all simulations, the Kolmogorov length scale is resolved with at least 1 grid point [100] and the thinnest reaction fronts were resolved with at least

10 grid points. Details of the physical parameters for the different cases and the expected ignition regimes are listed in Table 4.1. In addition, all the parametric cases are shown on the regime diagram in Figure 4.1. A typical profile of initial temperature is shown in Figure 4.2.

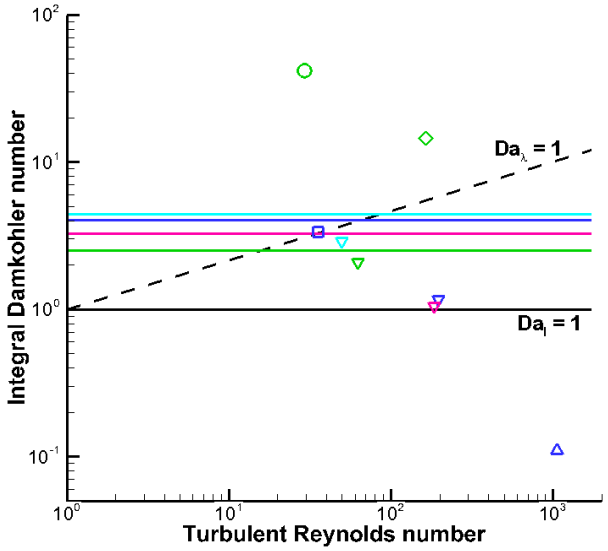

Figure 4.1: Parametric cases A (blue square), B (green circle), C (blue triangle), D (green diamond), E (pink delta), F (green diamond), G (blue delta) and H (sky blue delta) on the ignition regime diagram. The solid lines with the same colors as the symbols correspond to the respective Sa = 1 lines for those cases.

Table 4.1: Physical and regime diagram parameters for the DNS parametric cases

Case	T_0 (K)	τ_{ig} (ms)	K^2	ℓ_e (mm)	u' (m/s)	τ_t (ms)	Da_ℓ	Re_ℓ	Da_λ	Ignition Regime[a]
A	990	25.8	4.05	4.3	0.05	86.0	3.34	35.3	1.02	W
B	1100	2.07	2.51	4.3	0.05	86.0	41.6	29.4	13.5	RD-S
C	990	25.8	4.05	4.3	1.5	2.87	0.11	1057	0.01	MD-S
D	1100	2.07	2.51	1.4	0.325	4.31	2.08	62.2	0.6	MXD
E	1020	12.7	3.28	4.0	0.3	13.33	1.05	185	0.2	MXD
F	1100	2.07	2.51	6.0	0.2	30.0	14.5	164	2.65	RD-S
G	990	25.8	4.05	6.0	0.2	30.0	1.16	197	0.2	MXD
H	970	41.3	4.41	6.0	0.05	120.0	2.91	50.0	0.8	MXD

[a]Predicted ignition regime based on the regime diagram theory. W, RD-S, MD-S and MXD correspond to weak, reaction-dominant strong, mixing-dominant strong and mixed/strong ignition regimes, respectively.

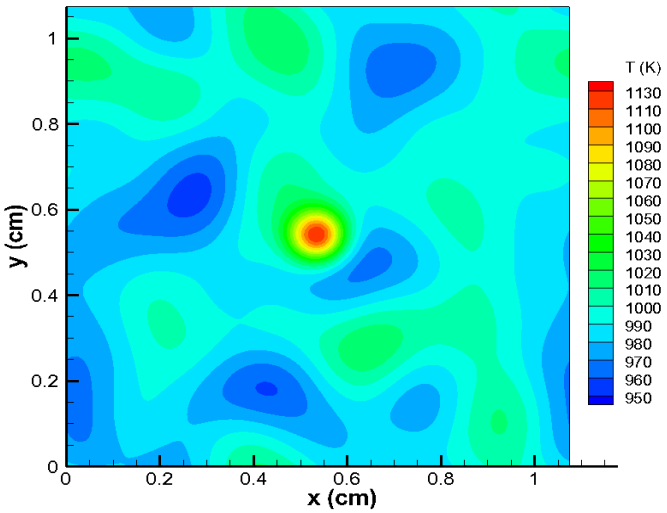

Figure 4.2: Initial temperature field for case A.

4.2 Results and discussion

4.2.1 General description of auto-ignition phenomena

For the eight simulation cases, auto-ignition progress was investigated by monitoring the temporal evolution of the temperature fields, mean pressure and heat release rate. For all cases tested, the observed ignition regimes were found to exhibit the behaviors predicted by the regime diagram as summarized in Table 4.1.

Results for three representative cases A, B and C are presented here which correspond to the W, RD-S and MD-S ignition regimes, respectively. Relative to cases A and C, the initial mean temperature for case B is higher and case C has relatively higher turbulence velocity fluctuation as compared with cases A and B.

Figure 4.3 shows the temporal evolution of temperature field for case A. It is readily observed that a reaction front emanates from the hot spot at the centre of the domain and consumes the majority of the reactant mixture. In

contrast, for case B, although there is initially some reaction front propagation from the hot spot (Figure 4.4(a)), the front is not able to consume much of the reactant mixture. Instead, isolated ignition fronts are formed in the end gas, consuming the rest of the mixture as shown in Figure 4.4(b). This is attributed to relatively higher reactivity of the mixture. Lastly, for case C, the stronger turbulence level leads to rapid scalar dissipation of the temperature fluctuations (Figure 4.5(a)). Due to strong turbulent mixing, T' decreases from the initial value of 15 K to a minimum value of 6 K, before any ignition fronts develop. Consequently, the reactant mixture auto-ignites nearly simultaneously throughout the domain as seen in Figure 4.5(b).

Figure 4.6 shows the temporal evolution of mean pressure and normalized integrated heat release rate (HRR) for the three cases, where the HRR is normalized by the maximum integrated HRR of the corresponding zero-dimensional (0D) cases. For comparison, the temporal evolution of 0D ignition for T_0 = 1100 K and 990 K are also shown. For case A, the pressure and HRR increase earlier and more slowly than the corresponding 0D case (at 990 K). The maximum HRR is also much lower. These features are attributed to enhanced compression heating of the end gas due to reaction front propagation. In comparison, cases B and C ignite much closer to the corresponding 0D ignition delay (at 1100 K) and have much higher peak HRRs compared with case A. Moreover, the rates of pressure rise are much higher for cases B and C compared with case A.

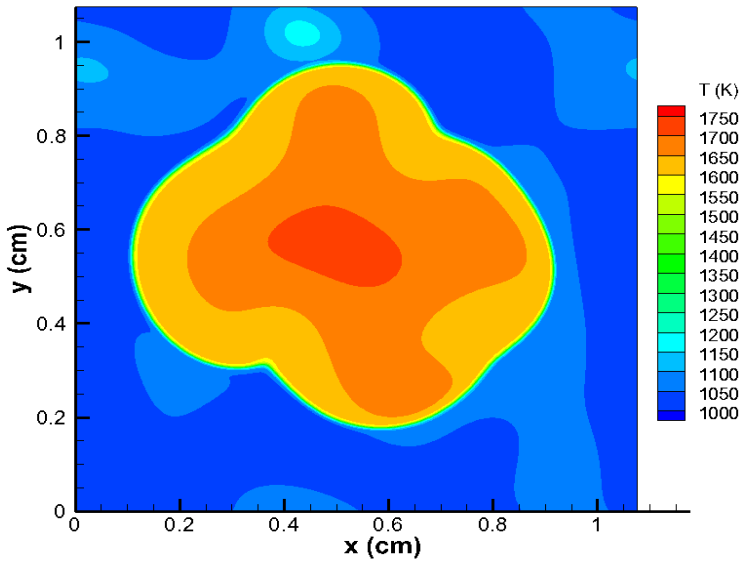

(a)

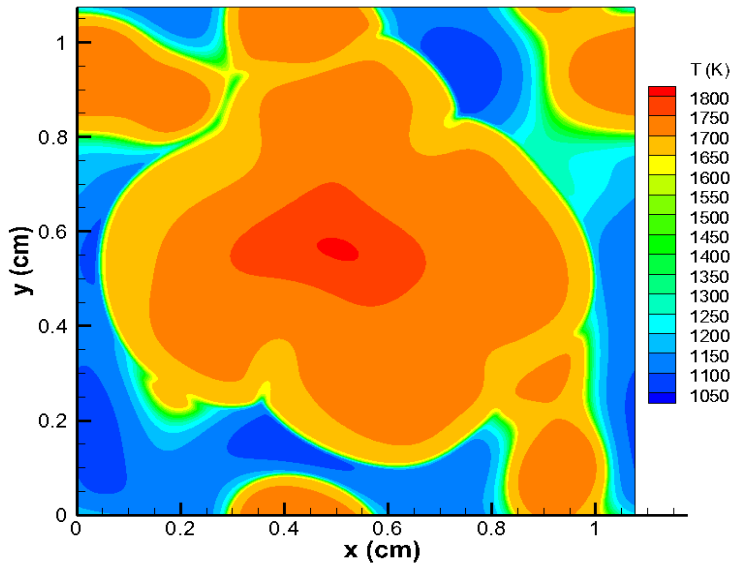

(b)

Figure 4.3: Temperature isocontours for case A at (a) 10.5 ms and (b) 12.5 ms.

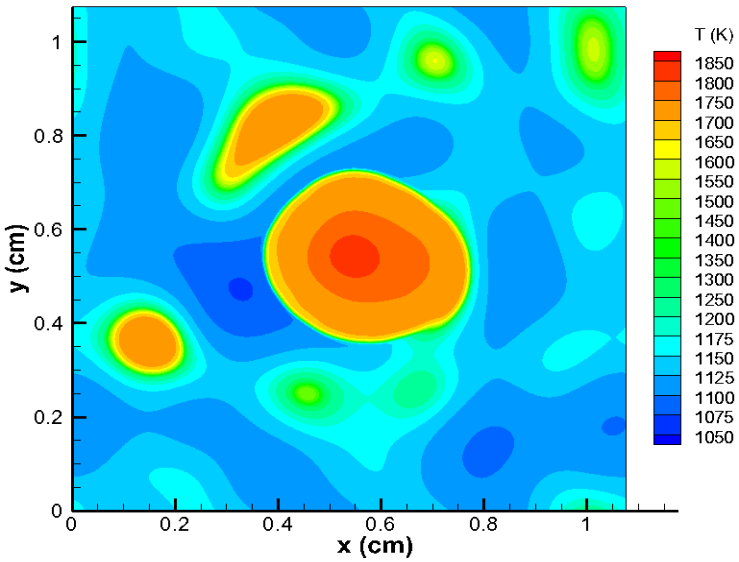

(a)

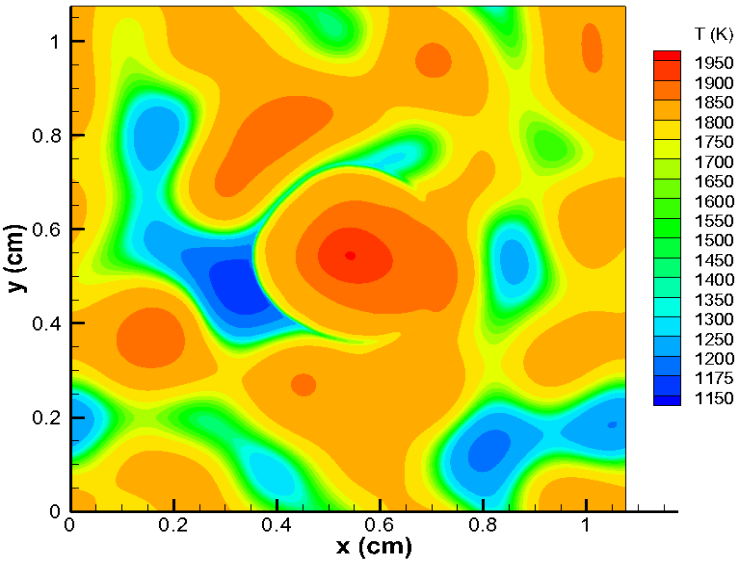

(b)

Figure 4.4: Temperature isocontours for case B at (a) 1.3 ms and (b) 1.6 ms.

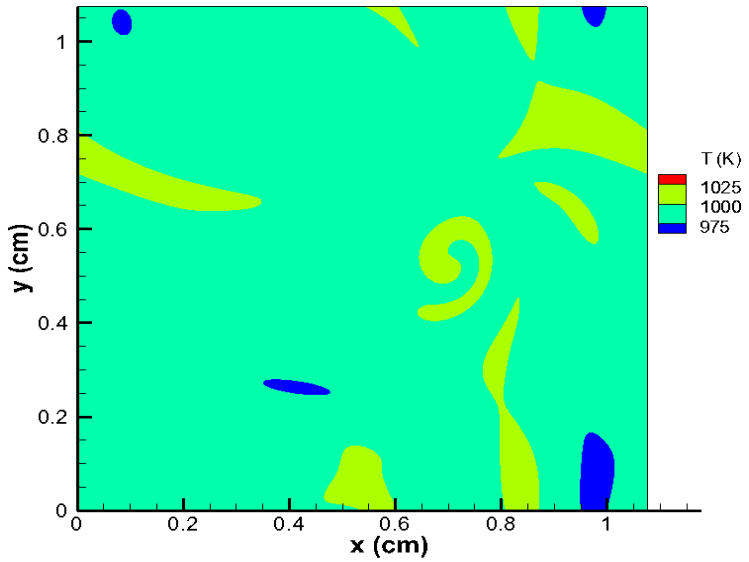

(a)

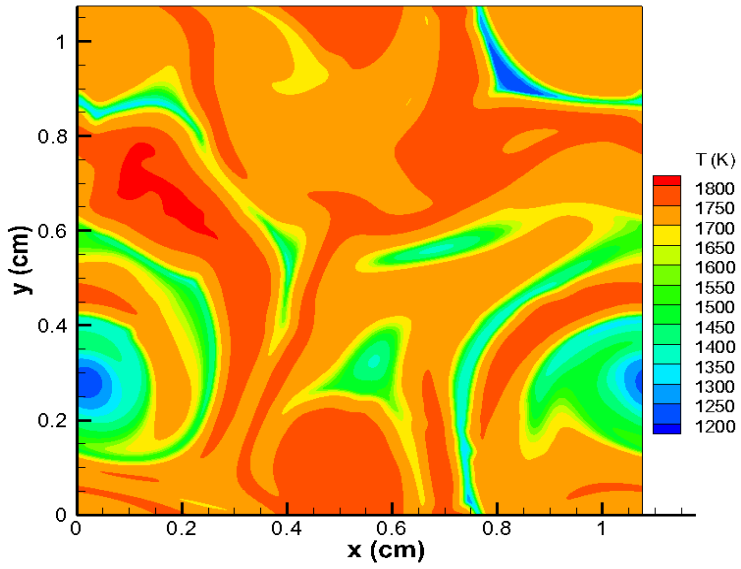

(b)

Figure 4.5: Temperature isocontours for case C at (a) 8.5 ms and (b) 24 ms.

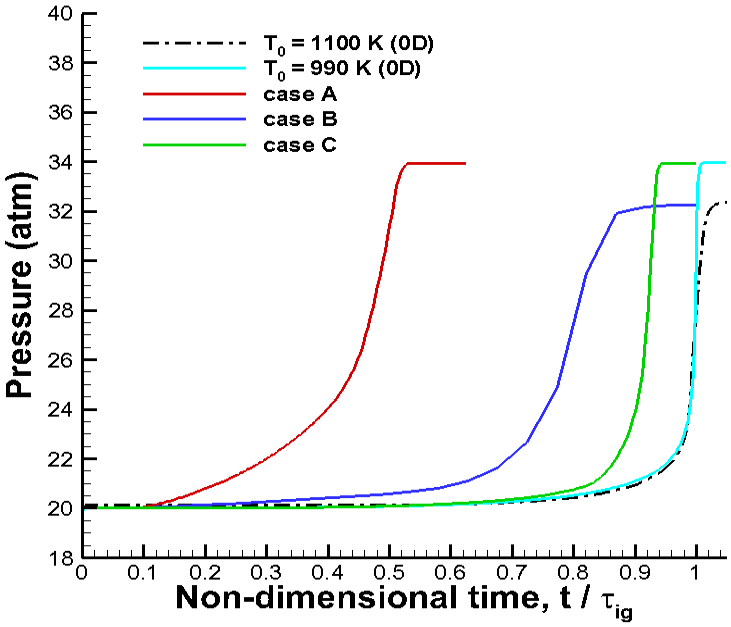

(a)

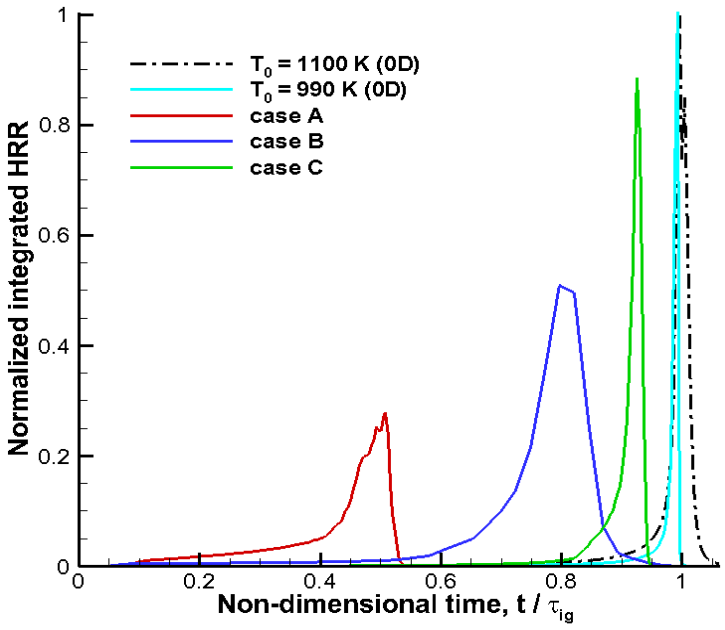

(b)

Figure 4.6: Temporal evolution of (a) mean pressure and (b) heat release rate for cases A, B and C. The time is normalized by the homogeneous ignition delay time at the mean initial mixture conditions for each case.

4.2.2 Front speed analysis

To characterize the auto-ignition behaviors, front propagation speeds are examined for the cases. The density-weighted front propagation speed, S_d, as defined in Equation (2.2), is employed as a metric to distinguish between deflagration and spontaneous ignition fronts. The isocontour of Y_{H_2} = 0.019 is chosen to evaluate the mean displacement speed as this particular isocontour coincides approximately with the location of instantaneous maximum HRR. Different choices of the marker species yielded consistent results.

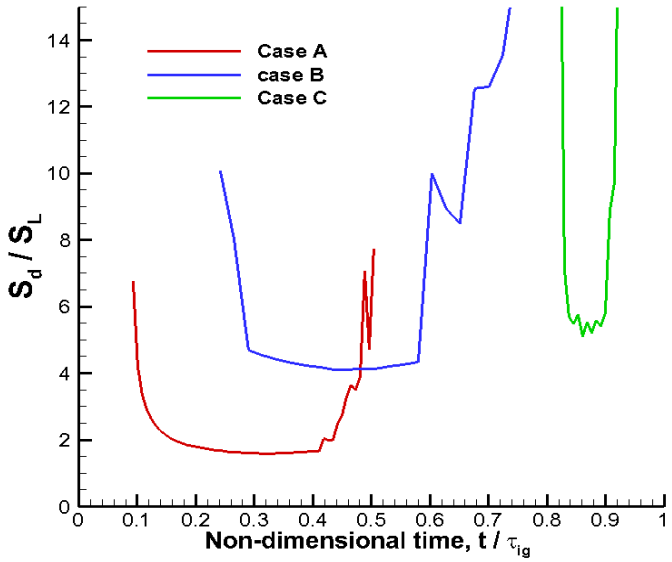

Figure 4.7: Temporal evolution of mean front speed for cases A, B and C. The time is normalized by the homogeneous ignition delay time at the mean initial mixture conditions for each case.

Figure 4.7 shows the temporal evolution of the mean front speed, normalized by the corresponding laminar flame speed, for cases A, B and C. The mean front speeds exhibit a characteristic U-shape, similar to the 1D

cases in chapter 2, which is attributed to the initial thermal runaway in the nascent ignition kernel during the early phase of combustion and final stage of fuel consumption. For case A, the minimum front speed is close to S_L (within a factor of 1.5) indicating deflagrative front propagation. On the other hand, for cases B and C, the minimum front speed is much higher (by over a factor of 4) than S_L, thereby suggesting that spontaneous propagation is the dominant combustion mode. Moreover, the duration of minimum front speed is much shorter for case C, indicating that the mixture auto-ignites nearly homogeneously in this case. These results along with the qualitative description of the ignition progress in section 4.2.1 suggest that the auto-ignition behaviors of cases A, B and C are in good agreement with the W, RD-S and MD-S regimes, respectively, as predicted by the regime diagram.

4.2.3 Computational singular perturbation (CSP) diagnostics

To gain further insights into the ignition characteristics, CSP analysis [101, 102, 103] is employed as an automated diagnostic tool to investigate the nature of the local reaction front propagation. CSP allows projection of all relevant chemical and transport processes onto a curvilinear frame of reference spanned by the right eigenvectors of the Jacobian matrix ($d\mathbf{g}/d\mathbf{Z}$) of the chemical source term vector ($\mathbf{g}$), where $\mathbf{Z}$ is the scalar solution variable vector (N_s species and temperature). The local eigenmodes, equal to the total number of scalar variables (N_s+1), are thus identified having distinct characteristic timescales. Moreover, importance indices can be identified as the non-dimensional measure of the relative contribution of an individual process to the dynamics of a target observable [104, 105]. To assess the role of transport with respect to chemistry in ignition front propagation, the importance index of transport (convection and diffusion) to the slow dynamics of temperature, I^T, is analyzed in the regions ahead of the reaction fronts

[105]. By definition, I^T ranges from 0 to 1; transport prevails over kinetics when this index assumes values close to unity.

Figure 4.8(a) shows the isocontours of I^T for case A at t = 10.5 ms. The corresponding temperature isocontours are shown in Figure 4.3(a). In addition, isocontours of HCO radical mass fraction (in black) are also superimposed to denote the active reaction zones. It is clearly seen that I^T approaches 1 in the upstream pre-heat region of the front, indicating that the reaction zone propagates upstream by virtue of transport, i.e., as a deflagration front. This confirms that the ignition behavior in this case is indeed in the weak (W) regime. Similarly, Figures 4.8(b) and 4.8(c) show the I^T and HCO mass fraction isocontours for cases B and C, at the same time instants for which the temperature profiles are shown in Figures 4.4(b) and 4.5(b), respectively. In contrast to case A, I^T is much lower (< 0.5) in the regions upstream of the ignition fronts. Therefore, front propagation is primarily driven by spontaneous ignition in these cases. Combining with the observations from the evolution of the respective temperature fields in Figures 4.4 and 4.5, it can be inferred that the cases B and C fall into the reaction-dominant and mixing-dominant strong ignition regimes, respectively. These results demonstrate that the ignition regime diagram is able to predict the strong and weak ignition regimes at various parametric conditions of initial turbulent velocity and temperature fluctuations with good fidelity.

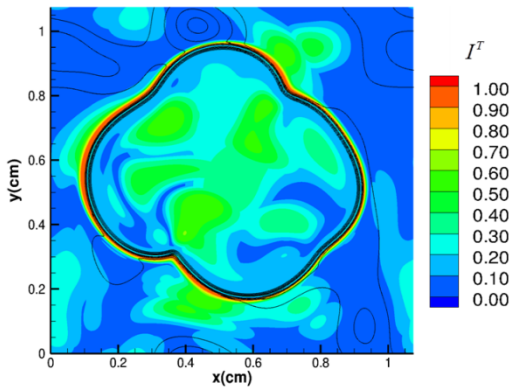

(a)

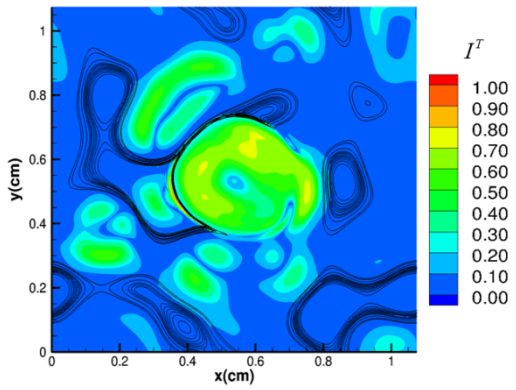

(b)

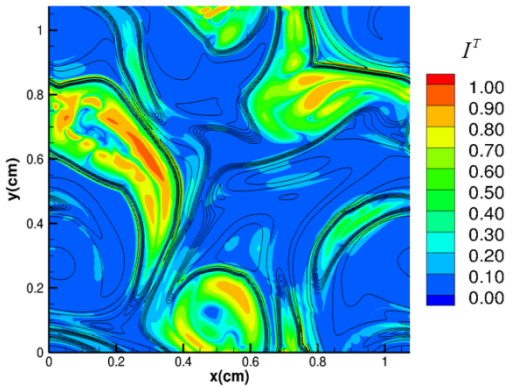

(c)

Figure 4.8: I^T isocontours for (a) case A (t = 10.5 ms), (b) case B (t = 1.6 ms) and (c) case C (t = 24 ms). The HCO mass fraction contours are overlaid (in black).

4.3 Concluding remarks

In the present work, 2D DNS of auto-ignition in a uniform syngas/air mixture in the presence of turbulence and temperature fluctuations were performed, at high-pressure low-temperature conditions. Parametric cases were considered by varying the characteristic integral Damköhler and Reynolds numbers of the system, corresponding to different conditions on the ignition regime diagram proposed in chapter 3. For all cases, the observed ignition behaviors were found to agree with the predictions of the regime diagram consistently. Three representative cases A, B and C were analyzed in detail. Temporal evolution of the temperature field, mean pressure and integrated HRR showed increased propensity for reaction front propagation from a hot spot in case A; whereas for case B, isolated ignition kernels were formed; and for case C, rapid dissipation of the temperature fluctuations due to strong turbulent mixing was readily observed. The features of the simulation results indicated that the cases could be classified as weak (case A), reaction-dominant strong (case B) and mixing-dominant strong ignition (case C).

Further investigation of the ignition front characteristics was carried out using front speed and CSP importance index analyses. These additional diagnostics consistently showed that ignition in case A was driven by deflagration, whereas cases B and C were dominated by spontaneous ignition. These results are new and importantly demonstrate the large range of auto-ignition behaviors that can be encountered at low-temperatures and high-pressures for syngas, as well as the profound effects of turbulence and temperature fluctuations to accelerate ignition relative to 0D reference conditions. Significantly larger effects were observed in the weak ignition regime, consistent with the experimental observations [24]. Furthermore, the DNS results were consistent with predictions from the regime diagram based on theoretical scaling analysis. This demonstrated that the physical and

chemical mechanisms controlling auto-ignition phenomena in thermally inhomogeneous turbulent reacting flows were well captured by the ignition criteria proposed in chapter 3.

Chapter 5
Assessment of flamelet versus multi-zone combustion modeling approaches for stratified-charge compression ignition engines

In this chapter, the spray-interactive flamelet (SIF) and extended multi-zone (EMZ) combustion models coupled with multi-dimensional CFD are employed to investigate the effects of charge stratification in a direct-injection compression ignition engine under low load conditions. The objective of the present study is to assess the validity of the multi-zone and flamelet approaches to spray combustion in DI/HCCI engines with varying levels of in-cylinder charge stratification resulting from different fuel injection timings. A parametric study is carried out in order to compare the two approaches for early and late fuel injection scenarios. The numerical results are compared against available experimental data [46].

5.1 Experimental conditions and numerical setup

The experimental study conducted by Dec and Sjoberg [46], which investigated fuel stratification effect on HCCI using direct injection, is adopted as main data in order to validate the multi-zone and flamelet-based combustion models. The engine used in the experiment had a shallow bowl, pancake-shaped piston. A hollow-cone, swirl stabilized gasoline-type direct-injection (GDI) fuel injector with 44^0 spray cone angle and injection pressure

of 70 bar was mounted at the center of the cylinder head. The fuel used was iso-octane. The details of the engine geometry and operating conditions are listed in Table 5.1. The intake valve closing (IVC) and exhaust valve opening (EVO) crank angles are calculated from top-dead-center (TDC) intake, such that 360^0 CA corresponds to the TDC position.

Table 5.1: Engine design and operating conditions [46]

Displacement	9.81×10^{-4} m^3
Bore	0.102 m
Stroke	0.12 m
Connecting rod	0.192 m
Geometric compression ratio	18:1
IVC	205^0 CA
EVO	480^0 CA
Fuel	Iso-octane
RPM	1200
Intake pressure	120000 Pa
Intake temperature	415 CA
Global equivalence ratio	0.1
Fuel injection duration	1.9^0 CA

A multi-dimensional CFD code, KIVA-3V [106], is used in the present study. Numerical simulations are performed for the closed part of the cycle, from IVC to EVO. The global equivalence ratio is 0.1. A uniform mixture distribution is specified at IVC. A parametric study over a range of start-of-injection (SOI) timings between 220^0 CA and 315^0 CA is conducted. As the spray arrangement considered is symmetric, a quasi-2D grid, with 1.5 mm

grid spacing and 0.5^0 sector angle is used. Periodic boundary conditions are imposed in the azimuthal direction. The computational mesh at TDC is shown in Figure 5.1, where the left end corresponds to the cylinder axis. The crevice region is incorporated in the mesh, which is further refined near the wall for better accuracy. Based on motored pressure trace matching, an effective compression ratio of 16.8 is used for numerical modeling [107]. For an unbiased model comparison, a constant estimated temperature at IVC (T_{IVC}) of 408 K is used in all simulation cases, based on the correlation from Sjoberg and Dec [108]. No model "tuning" has been performed. In-cylinder turbulence is modeled using the re-normalized group (RNG) k-ε model [109] with wall functions. The flow field at IVC is initialized with a swirl ratio of 0.9 from the experiment. The Taylor Analogy Breakup (TAB) [110] breakup model built into KIVA-3V is used to describe spray atomization. A skeletal reaction mechanism by Chen et al. [111] with 259 species is used for modeling iso-octane chemistry. In addition, the thermal NO emissions are modeled by the extended Zeldovich mechanism [112]. Both the EMZ and SIF combustion models are integrated into KIVA-3V, in the framework of Reynolds-averaged Navier-Stokes (RANS) formulation. These models are summarized in the next section.

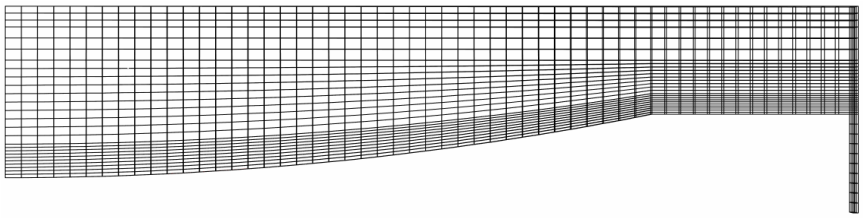

Figure 5.1: KIVA-3V computational mesh at TDC.

5.2 Combustion modeling approaches

5.2.1 EMZ model

In this approach, all the fluid mechanical processes, such as spray, turbulent diffusion and mixing, are handled by KIVA-3V on a highly resolved CFD grid of the engine geometry. Instead of solving for chemistry in each cell, however, the multi-zone chemical kinetics solver aggregates the cells from the grid into a relatively smaller number of zones based on temperature (T), composition (equivalence ratio [69], φ) and specific internal energy of formation (u_f) [70] used as progress variables. Each zone contains a fraction of mass (not exceeding 1% of the total mass) in the cylinder and is representative of a group of cells with similar thermodynamic and chemical properties. The averages of the temperature, composition and pressure for the cells in each zone are used to represent the thermodynamic state of the mixture in that particular zone. This thermodynamic state is then used as an initial condition for an adiabatic constant volume reactor calculation to determine the change in species composition and heat release for the zone over the time step [69].

After the chemistry calculation, the new species composition and heat release are redistributed from each zone back onto the corresponding cells in physical space. This remapping is done under three constraints [69]: 1) the mass of each cell within the zone must be conserved; 2) the mass of each individual species within the zone must be maintained during remapping; and 3) the total number of C, H, O and N atoms in each cell must be maintained. The composition change and the heat release due to chemical reactions in each cell obtained from remapping provide the chemistry source terms in the species continuity and internal energy governing equations, respectively. The KIVA-3V code subsequently handles these governing equations and solves for the convection and diffusion processes over the same

time step. Figure 5.2 shows a flow chart briefly describing the fully coupled KIVA-EMZ model.

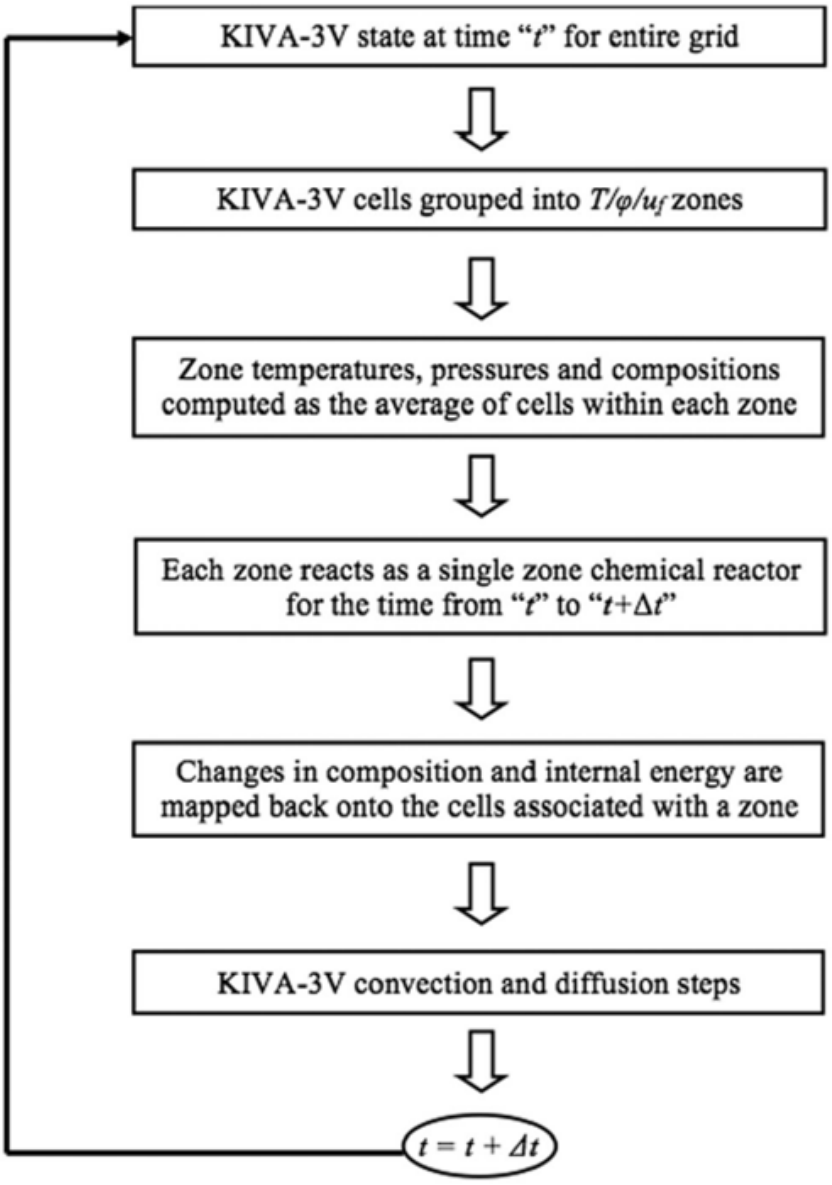

Figure 5.2: A schematic flow chart of the KIVA-EMZ model.

5.2.2 SIF model

As in the standard flamelet approach, the SIF model [85] determines the large number of reactive scalars in a reduced dimensional space governed by conserved scalar variables. However, a key feature of the SIF model is that it fully incorporates the interaction between spray evaporation and gas-phase combustion, which is important when the overlap of the two processes becomes large. In this approach, a mixture fraction (*Z*) is defined by the carbon mass fraction, defined as:

$$Z = \sum_{i=1}^{n} Y_i \frac{\varsigma_i}{\varsigma_{Fuel}} \tag{5.1}$$

where ς_i represents the carbon mass fraction in species *i*. The KIVA-3V CFD code is modified to solve the transport equations for favre-averaged mean ($\tilde{Z}$) and variance ($\widetilde{Z''^2}$) of the mixture fraction in the physical space, instead of the actual species transport equations. The modified CFD code also solves for the turbulent flow field and determines the thermodynamic properties (pressure *p*, total specific enthalpy $\tilde{h}$), droplet vaporization rate ($\dot{\rho}_f$) and the scalar dissipation rate ($\tilde{\chi}$). The local scalar dissipation rate is modeled [113] as follows:

$$\tilde{\chi} = c_\chi \frac{\tilde{\varepsilon}}{\tilde{\kappa}} \widetilde{Z''^2} \tag{5.2}$$

with c_χ = 2.0. The conditional averaged scalar dissipation rate, $\tilde{\chi}_Z$, is then determined by a volumetric average and using an assumption of a one-dimensional mixing layer [114]. The spray vaporization source terms are also

expressed as functions of mixture fraction by using a conditional averaging approach [85].

Once these variables are computed in the CFD code, the spray vaporization source terms and the conditional averaged scalar dissipation rate are passed onto the reactive space, where the following governing equations for reactive species and temperature are solved by the flamelet solver:

$$\rho \frac{\partial Y_i}{\partial t} = \rho \frac{\tilde{\chi}_Z}{2} \frac{\partial^2 Y_i}{\partial Z^2} + \dot{\omega}_i + \dot{\rho}_i - \dot{\rho}_Z \frac{\partial Y_i}{\partial Z} \tag{5.3}$$

$$\rho \frac{\partial T}{\partial t} = \rho \frac{\tilde{\chi}_Z}{2} \frac{\partial^2 T}{\partial Z^2} + \dot{\omega}_T + \rho \frac{\tilde{\chi}_Z}{2C_P} \frac{\partial C_P}{\partial Z} \frac{\partial T}{\partial Z} + \frac{1}{C_P} \frac{\partial P}{\partial t} + \sum_{i=1}^{n} \rho \frac{\tilde{\chi}_Z}{2\mathrm{Le}_i} \frac{C_{Pi}}{C_P} \frac{\partial Y_i}{\partial Z} \frac{\partial T}{\partial Z} + \frac{1}{C_P} \sum_{i=1}^{n} h_i \dot{\rho}_i - \dot{\rho}_Z \frac{\partial T}{\partial Z} \tag{5.4}$$

Equations (5.3) and (5.4) are derived by a coordinate transformation from the physical space to the reactive space. In the present work, the reactive space in Z is described by 100 grid points between Z = 0 (no fuel) and Z = 1 (pure fuel). In the above equations, the first term on the right-hand-side (RHS) represents turbulent diffusive transport, where $\tilde{\chi}_Z$ accounts for the effect of small-scale turbulent mixing on combustion. The second term on the RHS is the chemical source term. The last two terms correct for the direct local increase in the species mass fraction due to evaporation (in this case, only the fuel) and the indirect effect of species addition as a result of the shift in the mixture fraction coordinate due to evaporation, respectively. These additional terms allow for the full interaction between spray evaporation, gas-phase transport and reaction. Unity Lewis numbers are assumed for all reactive scalars. In the flamelet solver, chemical reaction rates are solved by

CHEMKIN-II [115] and LSODE [116] is used to integrate the equations in the reactive space.

Once the reactive scalar variables, Y_i (t, Z), are updated in the flamelet solver, the species information at each physical location is determined by the probability distribution function (PDF) integral with a presumed beta PDF [113, 117]. The local temperature is then determined from the known species information and the known total enthalpy. The interaction between the CFD code and the flamelet solver is schematically shown in Figure 5.3. The information being passed from the KIVA-3V CFD solver to the flamelet solver is shown in dashed lines. A detailed description of the fully coupled KIVA-SIF model can be found in Keum et al. [85].

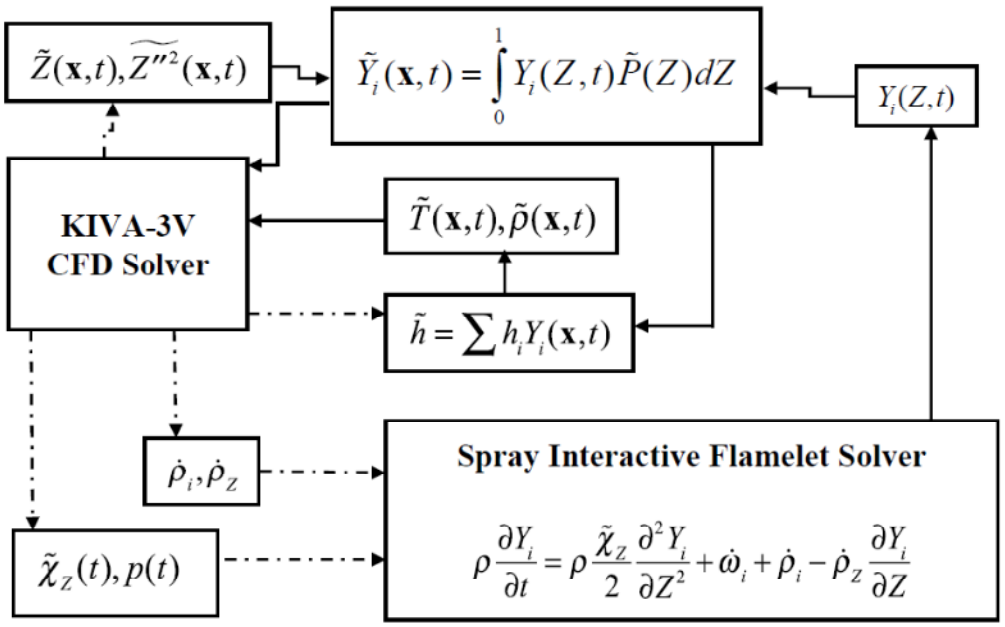

Figure 5.3: A schematic of the KIVA-SIF code structure. The information passed from the KIVA-3V CFD solver to the flamelet solver is represented by dashed lines.

5.3 Results and discussion

The results from the numerical study are compared with available experimental data in the form of mean in-cylinder pressure trace, ignition timing, combustion efficiency, CO and NO_x emissions. In addition, in-cylinder distributions of temperature, equivalence ratio and intermediate radicals at different time instants are examined to analyze the combustion progress predicted by the two combustion models considered here. The key parameter is the injection timing: (a) an early fuel injection case with SOI at 220^0 CA, and (b) a delayed injection with SOI at 315^0 CA.

5.3.1 Early fuel injection

The in-cylinder pressure from the numerical simulations versus crank angle is compared to the experiment for the earliest SOI at 220^0 CA in Figure 5.4. There is good agreement between the simulations and experiment with the simulations slightly over-predicting the peak pressure. Both the SIF and EMZ models predict nearly identical pressure rise rates (heat release) and ignition timing for this early fuel injection case. The spatial distributions of temperature and equivalence ratio at TDC are compared between the SIF and EMZ combustion models in Figure 5.5. Both models predict nearly identical temperature distributions and combustion progress. The T-Φ scatter plot at TDC predicted by the SIF model as shown in Figure 5.6 (the corresponding EMZ plot is very similar) indicates that most of the in-cylinder mixture is very well-mixed (T range: 1000-1100 K, Φ range: 0.02-0.17) prior to ignition, resulting in conditions similar to lean HCCI.

Due to the low stratification level, only a small number of zones (approximately 100) are found to be sufficient for chemistry calculations by the EMZ model. As for the SIF combustion model, the species governing equation in the reactive space is given by Equation (5.3). Inspection of the

reactive space in mixture fraction reveals that the magnitude of conditional scalar dissipation rate is indeed very small during the pre-ignition stage. This suggests that turbulent diffusion due to small scale fluctuations (variances in mixture fraction) does not play any significant role in the auto-ignition, as would be expected in the HCCI condition. The spray source terms also vanish well ahead of ignition, as sufficient time is available for fuel evaporation to take place. Hence, the species governing Equation (5.3) is reduced to a homogeneous reaction equation:

$$\rho \frac{\partial Y_i}{\partial t} \simeq \dot{\omega}_i \tag{5.5}$$

such that the evolution of reactive species depends only on chemical reactions, with little effect of turbulent transport. Similarly, temperature evolution in Equation (5.4) also becomes solely dependent on chemistry and the compression heating due to piston motion. Consequently, for the early injection condition, the SIF model degenerates to the identical form of the EMZ model.

Table 5.2 compares the numerical and experimental results for combustion efficiency and CO emission. Combustion efficiency is defined as the difference between the enthalpy of the fresh charge at the intake valve closing (IVC) and that of the combustion products at exhaust valve opening (EVO), normalized by the maximum possible enthalpy difference [118]:

$$\eta_{comb} = \frac{\left(\sum h_i Y_i\right)_{EVO} - \left(\sum h_i Y_i\right)_{IVC}}{\left(\sum h_i Y_i\right)_{Equilibrium} - \left(\sum h_i Y_i\right)_{IVC}} \tag{5.6}$$

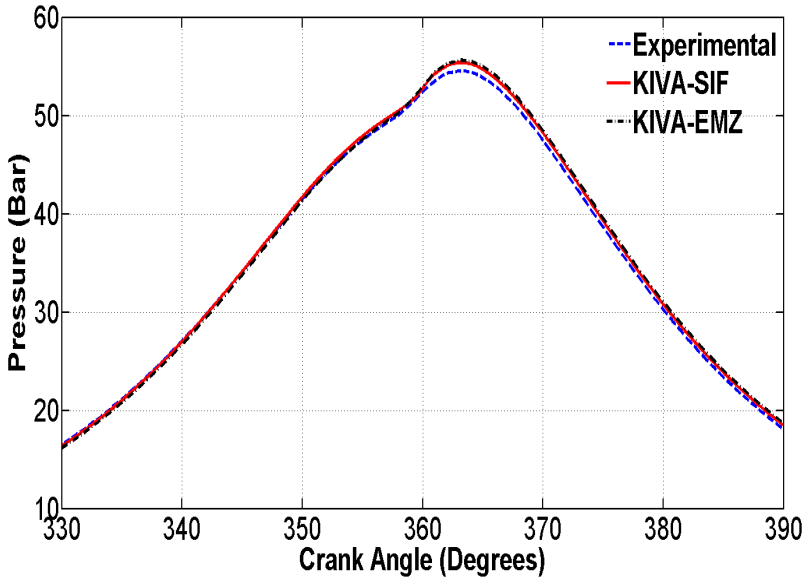

Figure 5.4: Pressure traces for the early injection case with SOI at 220^0 CA.

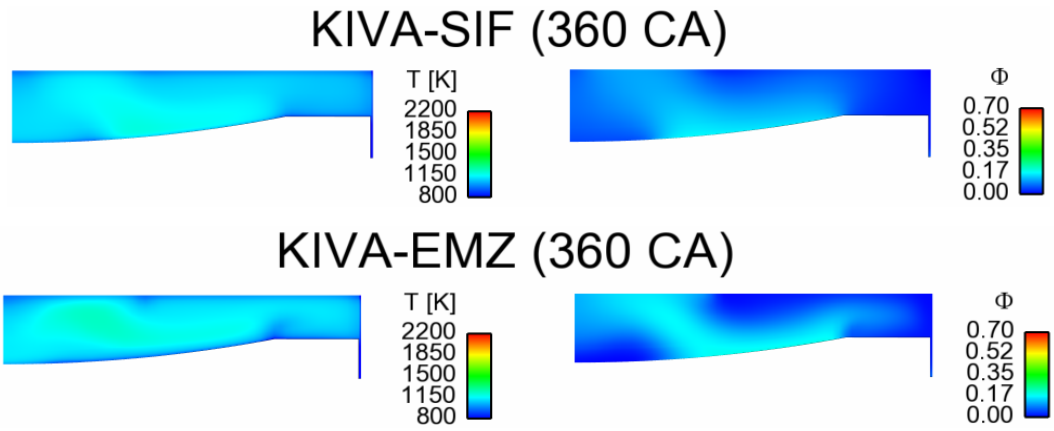

Figure 5.5: Spatial distributions of in-cylinder temperature and equivalence ratio predicted by the SIF and EMZ models at TDC for the early injection case with SOI at 220^0 CA.

Again, both the combustion model predictions are in good agreement with experiment. As the global equivalence ratio is very low and the in-cylinder

mixture is nearly homogeneous, the bulk temperatures are also very low with a maximum around 1300 K. This leads to incomplete CO-CO_2 conversion, resulting in high concentrations of CO and low combustion efficiency. The low in-cylinder temperatures also result in very low NO_x formation.

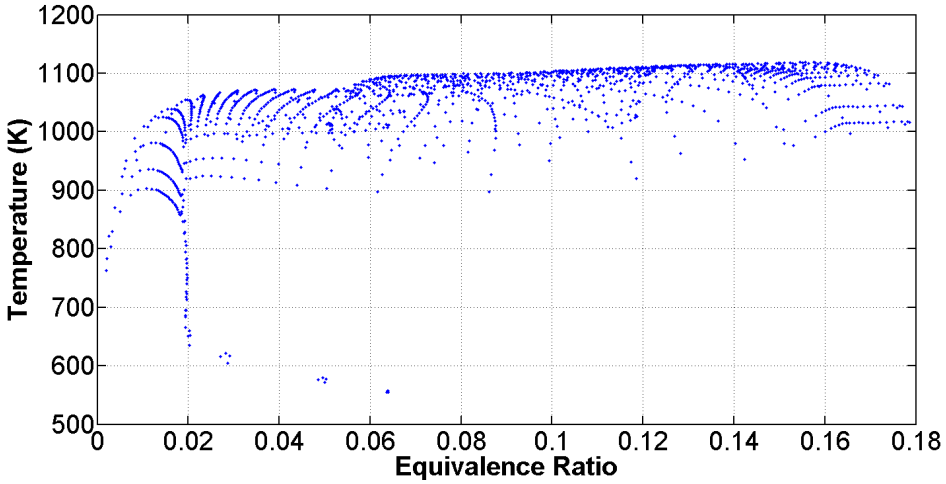

Figure 5.6: Scatter plot of in-cylinder temperature versus equivalence ratio predicted by the SIF model at TDC for the early fuel injection case with SOI at 220^0 CA.

Table 5.2: Experimental and numerical results for fuel injection timing at SOI 220^0 CA

Method	Combustion efficiency	CO (g/kg fuel)
Experimental	0.58	982
KIVA-SIF	0.71	934.35
KIVA-EMZ	0.74	921.24

5.3.2 Delayed fuel injection

Figure 5.7 shows the pressure traces from the simulations and experiment for the delayed injection case with SOI at 315^0 CA. In this case, the SIF model prediction agrees very well with the experimental data, except for a slight over-prediction of pressure rise (case "SIF-full model"). In contrast, the EMZ model significantly under-predicts the ignition delay as well as the overall combustion phasing and pressure rise (case "EMZ-default zones").

The spatial distributions of temperature, equivalence ratio, H_2O_2 and OH radicals at some specific crank angles prior to ignition are shown in Figures 5.8-5.10, depicting the combustion progress as predicted by the two models. The interaction between spray and the gas motion generated by the piston results in the formation of high equivalence ratio pockets. The high-Φ regions have decreased temperatures due to evaporative cooling from the liquid fuel spray and decreased compression heating due to lower values of the specific heat ratio. This results in a much higher degree of large scale mixture stratification.

The evolution of the radical species prior to ignition shows considerable differences between the two combustion models. For both SIF and EMZ models, the radical pool starts to develop (Figure 5.8) at the spray contours, where the temperature is relatively higher. However, the radical build-up for the SIF model soon accelerates faster as compared to the EMZ model (Figures 5.9 and 5.10), especially in the richer mixtures, ultimately leading to more advanced overall ignition as seen in the pressure plots of Figure 5.7.

One of the factors that influence the accuracy of the EMZ model is the zoning of computational cells before chemistry calculation and the remapping of species from zones to corresponding cells after solving for chemistry. Each zone is considered homogeneous at the average temperature, pressure and composition of the cells contained in that particular zone. As such, solving for chemistry does not account for any effects of local gradients. In addition, the

remapping of species at each time step is done in such a way that some detail of composition gradients from the previous time step is maintained [119]. This may lead to similar distributions of species over a number of time steps and hence slower reaction progress. To mitigate these effects, an additional EMZ simulation is performed where the zoning criteria are tightened by a factor of 100 over the default values mentioned in the previous section. Tightening the zoning criteria increases the computational time significantly as the number of zones created (~2000) is much greater than the default case (~200). The corresponding pressure trace is shown in Figure 5.7 (case "EMZ-refined zones"). As expected, the EMZ-refined zones case yields faster ignition, higher pressure rise rate and peak pressure relative to the default zoning case, although not by a sufficient amount. On the other hand, the SIF model employed in this study is based on a single representative flamelet formulation, indicating that the computational cost is much lower than the EMZ counterpart. A more important implication is that high fidelity can be more effectively achieved by incorporating the small-scale fluctuations (by way of the scalar dissipation rate in this case) in the combustion submodel, especially as the level of fluctuations becomes larger.

One of the key components of the SIF combustion model is the scalar dissipation rate, which connects the physical and reactive spaces and denotes the rate of small-scale mixing. Figure 5.11 shows the temporal evolution of volume-averaged scalar dissipation rate (SDR) conditioned on the stoichiometric mixture fraction from the SIF numerical simulation. Immediately after the start of injection, SDR rises to approximately 100 s^{-1} due to high mixture fraction gradients, followed by a slower decay. A secondary rise at 357^0 CA is due to the onset of ignition creating an abrupt local consumption of reactants and creation of gradients. It is evident that the effect of scalar dissipation rate cannot be neglected before and during ignition for the late injection case.

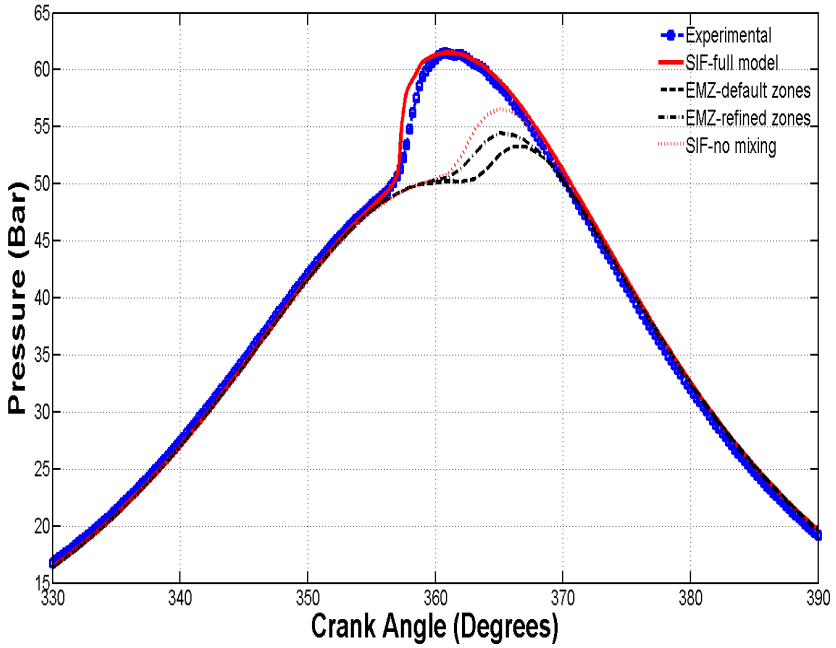

Figure 5.7: Pressure traces for delayed fuel injection case with SOI at 315^0 CA.

Figure 5.12 shows the evolution of two key profiles in the mixture fraction space: (a) H_2O_2 concentration, representative of ignition precursor at this thermodynamic condition, and (b) temperature. It is observed that H_2O_2 is initially formed at the lean mixtures, where $Z << Z_{st} = 0.063$, but the temperature is high. Subsequently, the peak concentration shifts towards richer mixtures. At 357^0 CA, denoted by the transition from dashed to solid curves, ignition starts at $Z = 0.0315$. The location of the peak concentration continues to move toward higher Z condition, via the transport of radicals and heat. The SIF model properly captures this effect via the turbulent diffusion terms in Equations (5.3) and (5.4). In contrast, the EMZ approach inherently neglects the local turbulence-chemistry interaction while solving for chemistry. As such, the validity of the EMZ model is expected to be limited to relatively early injection timing leading to smaller level of fluctuations at the onset of ignition.

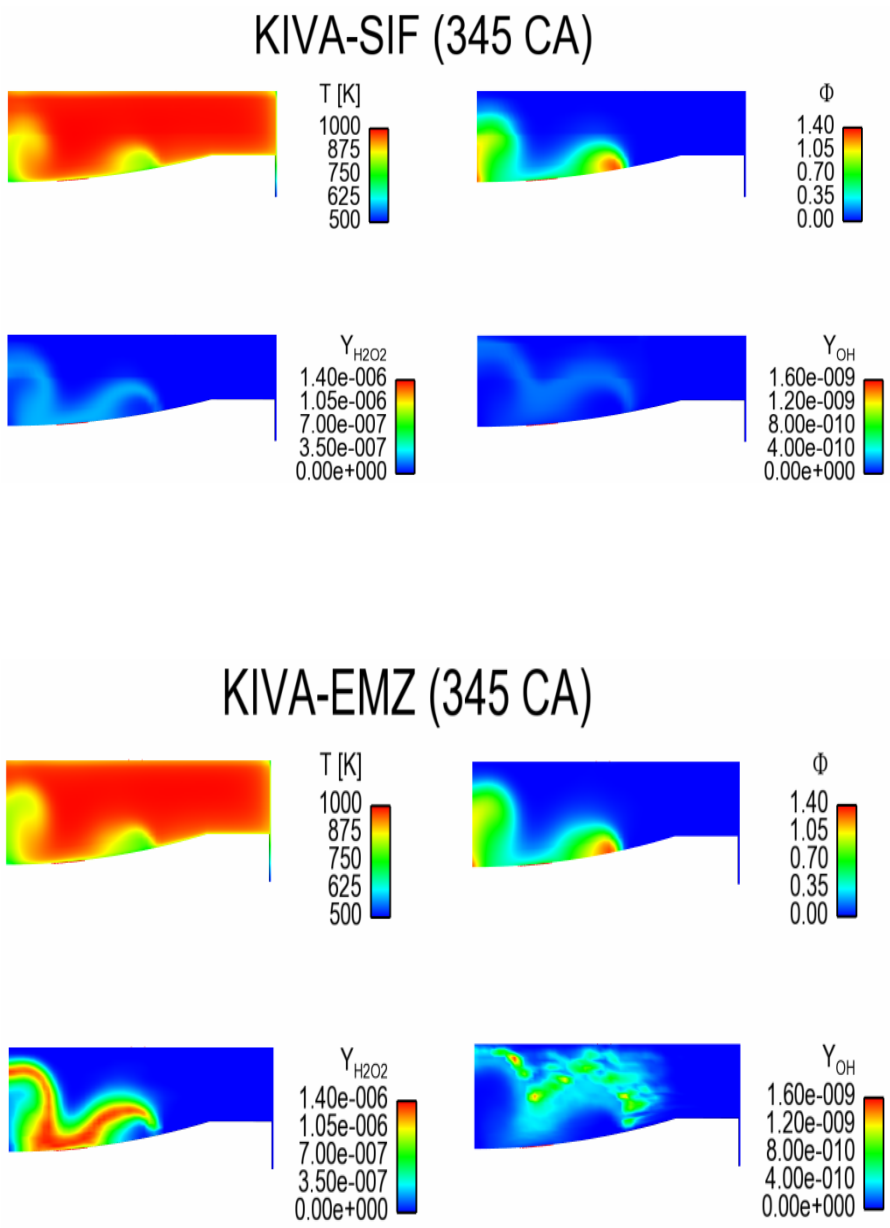

Figure 5.8: Spatial distributions of in-cylinder temperature, equivalence ratio, and H_2O_2 and OH mass fractions at 345^0 CA, predicted by the SIF and EMZ models for the late- injection case with SOI at 315^0 CA.

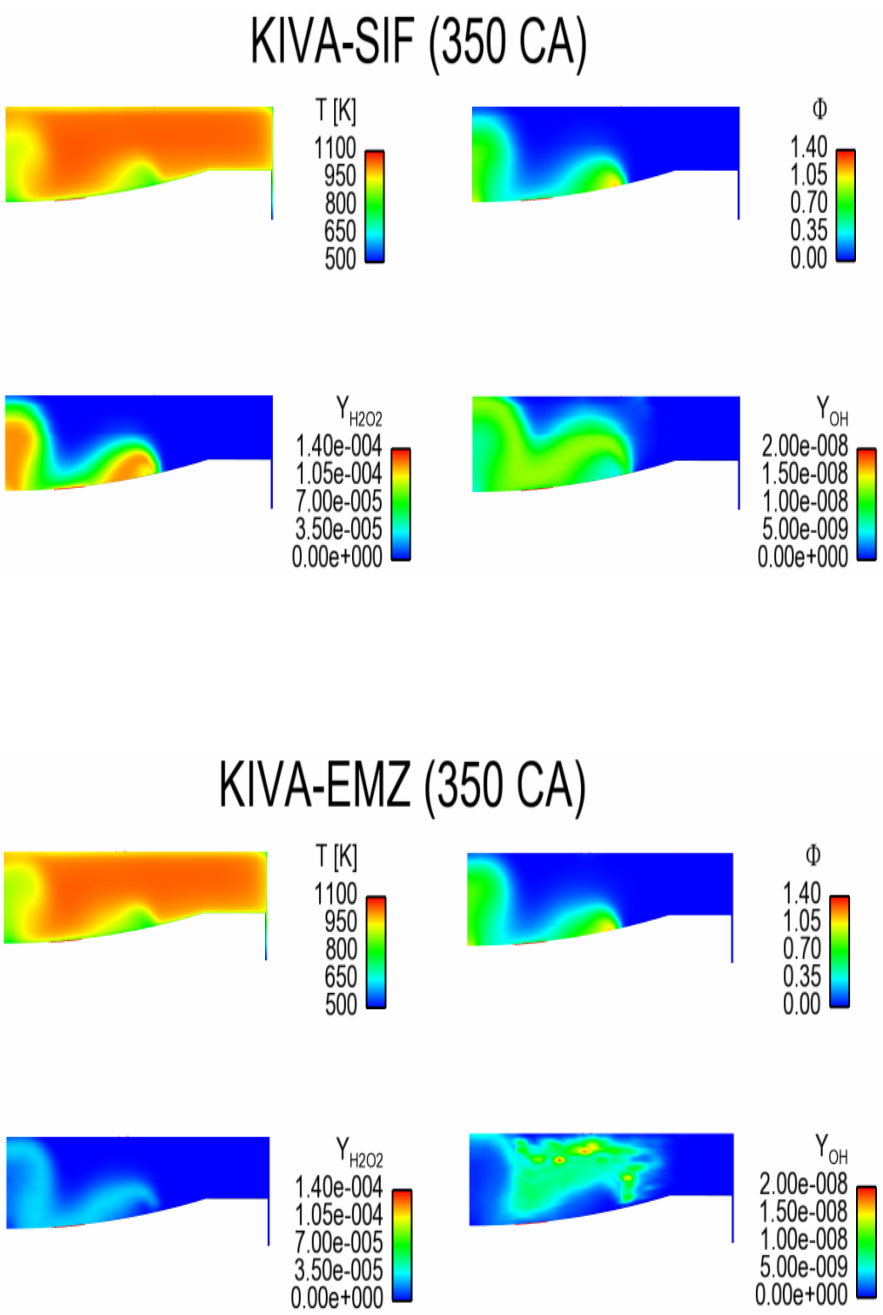

Figure 5.9: Spatial distributions of in-cylinder temperature, equivalence ratio, and H_2O_2 and OH mass fractions at 350^0 CA, predicted by the SIF and EMZ models for the late- injection case with SOI at 315^0 CA.

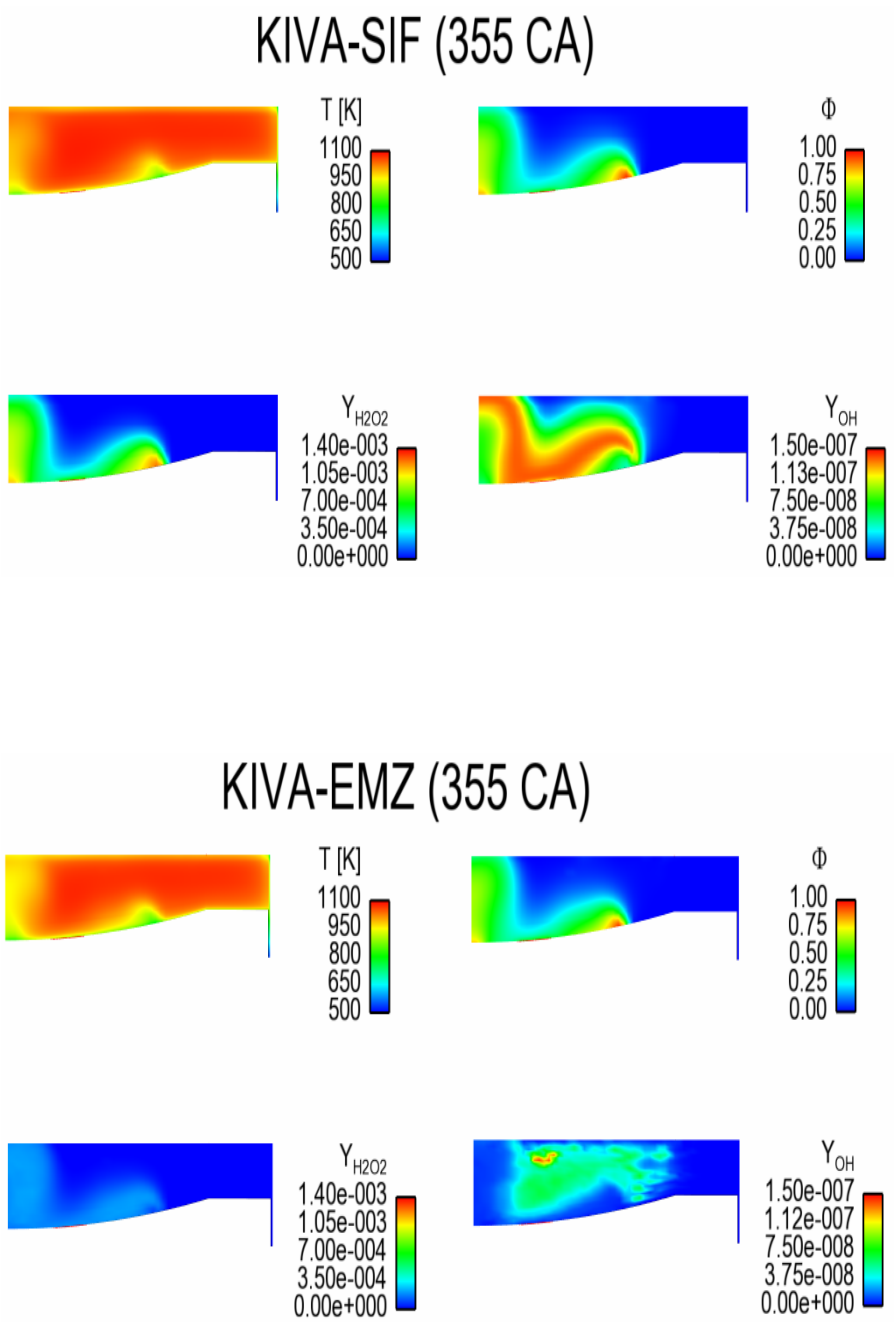

Figure 5.10: Spatial distributions of in-cylinder temperature, equivalence ratio, and H_2O_2 and OH mass fractions at 355^0 CA, predicted by the SIF and EMZ models for the late- injection case with SOI at 315^0 CA.

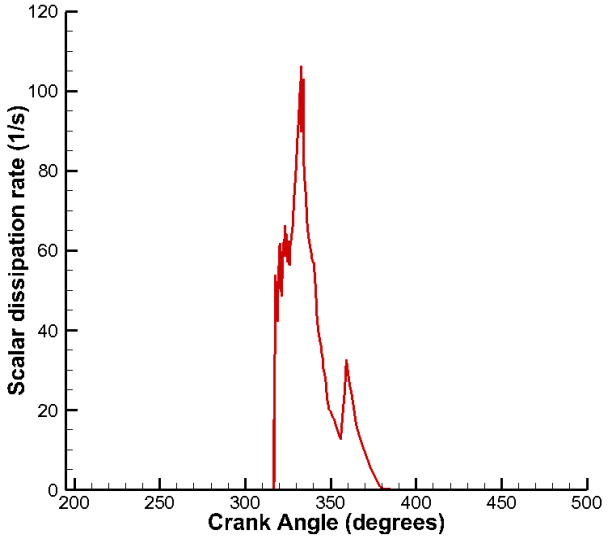

Figure 5.11: Time evolution of volume-averaged scalar dissipation rate conditioned on stoichiometric mixture fraction predicted by KIVA-SIF model for SOI 315^0 CA.

The need to capture the small-scale turbulence mixing is demonstrated by conducting an additional test with the SIF model. In this case, the diffusive terms in the reactive space are artificially eliminated from the full SIF formulation, resulting in a homogeneous reactor type of model, although the detailed procedure to compute the reaction source terms is somewhat different from that of the EMZ approach. This test case is denoted as "SIF-no mixing" and the corresponding pressure trace is presented in Figure 5.7. It is clearly seen that the "no-mixing" model predicts a much lower pressure rise rate and retarded combustion timing; the results are much closer to the EMZ model than to the full SIF model. This further confirms that, when the in-cylinder mixture stratification is high, capturing the influence of turbulent mixing on chemistry is most critical in accurate prediction of the net ignition and combustion phasing. Incidentally, these findings are consistent with the conclusions drawn from earlier DNS investigations [72, 82].

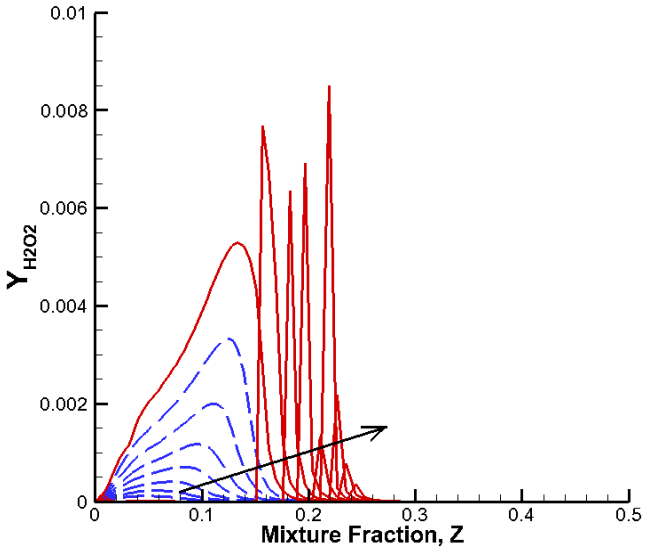

(a)

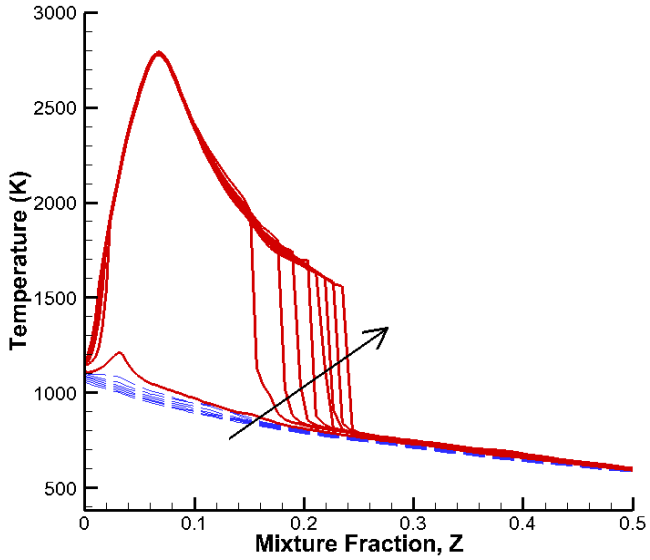

(b)

Figure 5.12: SIF model results of the time evolution of (a) H_2O_2 mass fraction and (b) temperature in the reactive space, for the delayed fuel injection case with SOI at 315^0 CA. The dashed and solid lines denote the pre-ignition (350^0 CA to 356^0 CA) and post-ignition (357^0 CA to 365^0 CA) periods, respectively. Crank angle increases in the direction of the arrow.

The numerical solutions of the "SIF-full model" and "EMZ-refined zones" cases are further compared with experimental results in terms of combustion efficiency, CO and NO_x emissions in Table 5.3. As the bulk temperatures predicted by the EMZ model are lower than the SIF model, it predicts much higher levels of CO and lower levels of NO_x. Delayed combustion timing, lower heat release rate and higher CO emissions lead to a lower combustion efficiency predicted by the EMZ model.

Table 5.3: Experimental and numerical results for fuel injection timing at SOI 315^0 CA

Method	Combustion efficiency	CO (g/kg fuel)	NO_x (g/kg fuel)
Experimental	0.92	180	27
KIVA-SIF	0.95	163.67	29.38
KIVA-EMZ	0.82	356.34	16.21

5.3.3 SOI parametric study

Finally, as a parametric study, predictions by the two models for various key quantities are compared against the experimental data. Table 5.4 compares the level of stratification for different SOIs in terms of the standard deviation of local equivalence ratio (σ_Φ) at 365^0 CA, as obtained from the simulations with the SIF model, showing an increase in the level of stratification as the SOI is delayed.

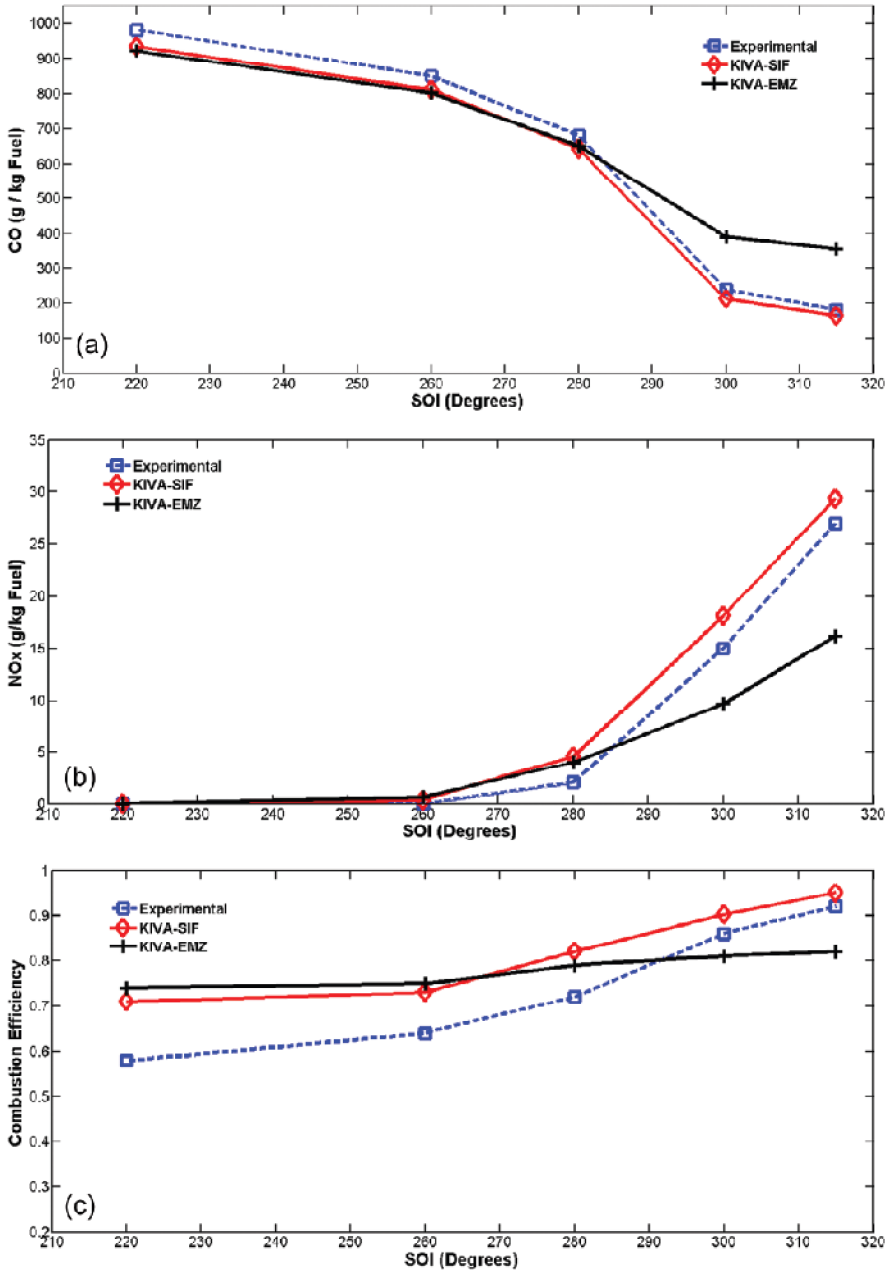

Figure 5.13: Comparison between experimental data and model predictions over a range of SOI timings: (a) CO emissions, (b) NO_x emissions, and (c) combustion efficiency.

A comparison of combustion efficiency, CO and NO_x emissions between the numerical results and experimental data over a range of SOI is shown in Figure 5.13. At earlier SOI conditions, the two modeling results are nearly identical. As the SOI is delayed, however, more mixture inhomogeneities arise in the engine cylinder and the performance of the SIF model improves and agrees more closely with the experimental data. Both models tend to over-predict combustion efficiency, but the SIF model results improve as the SOI is delayed and overall capture the trend with the experiment more consistently than the EMZ model.

Table 5.4: Effect of SOI on the standard deviation of equivalence ratio (at 365^0 CA)

SOI (^{0}CA)	σ_Φ
220	0.05
260	0.075
280	0.087
300	0.140
315	0.235

5.4 Concluding remarks

Combustion models based on the spray-interactive flamelet and extended multi-zone approaches were employed in DICI engine simulations. A parametric study over a wide range of SOI timings was conducted, and the numerical results were validated against available experimental data. It was observed that for low in-cylinder stratification condition, both SIF and EMZ models predicted similar ignition timings, and combustion progress, CO and

NO_x emissions agreed very well with experiment. Under such nearly homogeneous mixture conditions, the SIF model degenerated into the EMZ model, as chemistry became important and turbulent mixing did not play a significant role. As charge stratification increased, however, the SIF model was found to be more accurate in predicting combustion characteristics. The EMZ model under-predicted the ignition delay and combustion phasing because it neglected the effect of diffusive transport due to turbulent fluctuations, which was responsible for enabling faster overall ignition. Additional parametric comparisons further revealed that the improved prediction of the SIF approach was mainly attributed to its ability to describe the small-scale transport processes. This numerical study demonstrates that the SIF model serves as a more general framework for HCCI engine simulations for a wider range of stratified conditions.

In the next chapter, KIVA-SIF model is employed to further investigate the impact of fuel injection parameters such as injection pressure and spray cone angle on the performance of the DICI engine at low load conditions, for the most delayed SOI timing of 315^0 CA. Relative effectiveness of the two injection parameters in extending the low load limit of HCCI through delayed fuel injection strategy is assessed by conducting extensive parametric studies.

Chapter 6
Effects of fuel injection parameters on HCCI combustion at low load conditions

In this chapter, a numerical study is conducted to investigate the effects of fuel injection parameters, such as the injection pressure and spray cone angle, on the overall combustion efficiency and CO/NO_x emissions, with the objective of enhancing the effectiveness of late fuel injection strategy in extending the low load limit of HCCI engines. Closed cycle engine simulations are performed incorporating detailed iso-octane reaction kinetics and combustion submodel based on the SIF approach. Extensive parametric studies are conducted to provide a detailed map of the combustion efficiency and emission performance.

6.1 Numerical setup

The engine configuration and numerical setup for the present study are the same as described in section 5.1. In this case, the focus is on conditions near the NO_x knee (injection timing fixed at 315^0 CA) at which significant amount of NO_x was observed experimentally [46]. For parametric studies, the spray cone angle is varied from 44^0 to 120^0, while the injection pressure is varied from 70 to 1000 bar. For both parametric cases, the operating conditions for the baseline case are the same as listed in Table 5.1. KIVA-SIF model is used here, which was earlier discussed in section 5.2.2.

6.2 Results and discussion

6.2.1 Effects of fuel injection pressure

As a first parametric study, the injection pressure is varied from 70 bar (baseline case) to 1000 bar. Table 6.1 shows seven different injection pressures and the corresponding injection velocities considered in this work. The spray injection velocity is determined from the injection pressure using the following relation:

$$V_{inj} = C_D \sqrt{\frac{P_{inj} - P_{cyl}}{\rho_{fuel}}} \tag{6.1}$$

where C_D= 0.7 is used for the best match with the experimental conditions. The spray cone angle is kept constant at 44^0. It can be seen that the injection velocity increases with increasing injection pressure. Therefore, the injection duration is decreased accordingly, in order to maintain a constant global equivalence ratio of 0.1.

First, the effect of injection pressure on the level of mixture stratification is examined. As a quantitative metric, the equivalence ratio based on carbon/oxygen elemental mass fraction is employed. The standard deviation (σ_φ) and maximum value of the equivalence ratio versus the injection pressure are shown in Figure 6.1. All values are evaluated during combustion at TDC. It is observed that the standard deviation in the equivalence ratio decreases as the injection pressure increases, indicating that a higher injection pressure results in a more homogeneous mixture, which can be attributed to higher associated injection velocity. The effect is, however, more pronounced at the lower injection pressures. For example, an increase in injection pressure from 70 bar to 250 bar yields a decrease in the standard

deviation by almost two-fold. At further higher pressures, the effect becomes less sensitive to the injection pressure variation.

Table 6.1: Case setup - injection pressure

Case	P_{inj} (bar)	V_{inj} (m/s)
1	70	84.96
2	120	114.34
3	170	137.59
4	250	168.22
5	500	239.95
6	750	294.71
7	1000	340.78

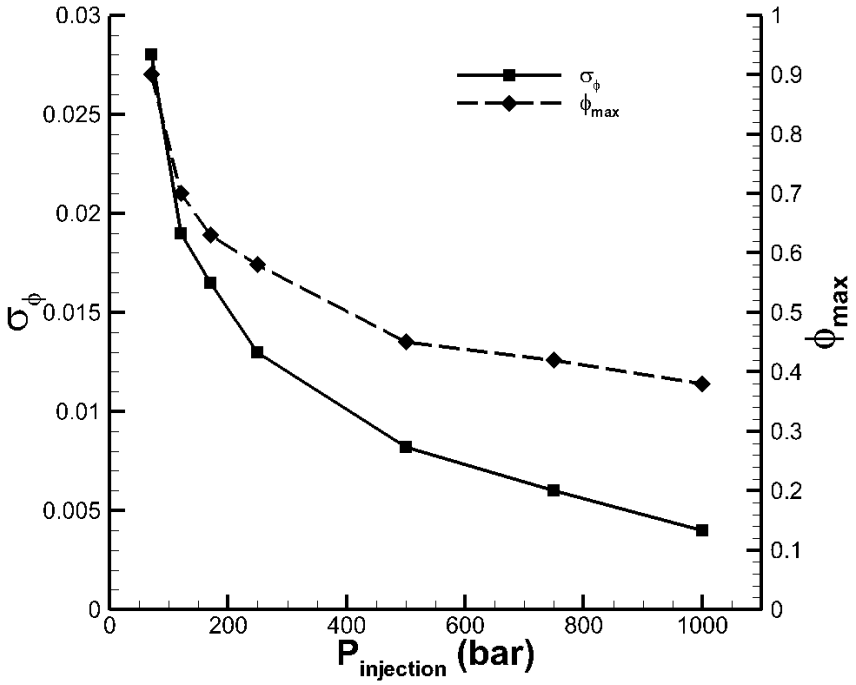

Figure 6.1: Standard deviation and maximum values of equivalence ratio (at TDC) versus fuel injection pressure.

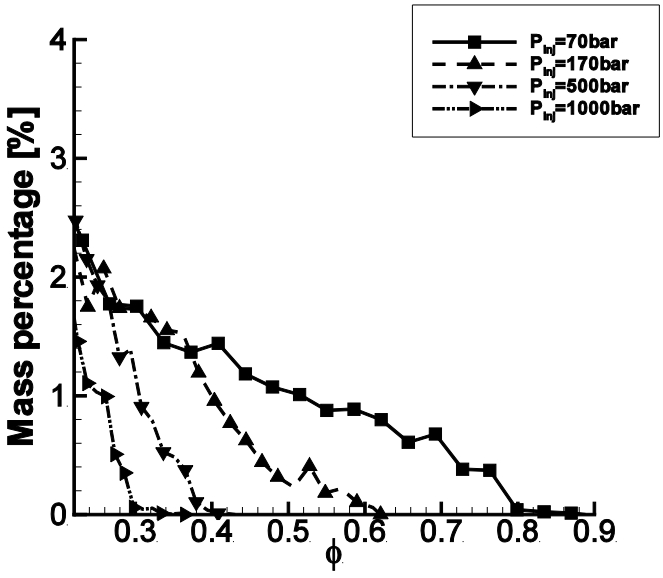

(a)

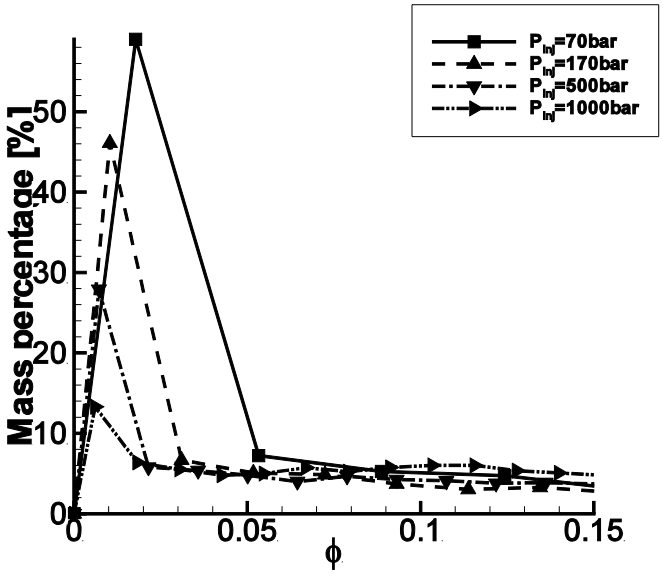

(b)

Figure 6.2: In-cylinder mass distribution over equivalence ratio: (a) maximum equivalence ratio and (b) unmixed region.

A similar trend is also observed in the maximum equivalence ratio behavior. Figure 6.2 shows the mass distribution of equivalence ratio at firing TDC for different injection pressures. For the convenience of discussion, the mass distributions are shown in two different scales on the x-axis. First, the effect of injection pressure on the maximum equivalence ratio is examined in Figure 6.2(a). The x-axis scale is taken between 0.2 and 0.9 to examine the maximum value of the in-cylinder equivalence ratio at different injection pressures. It is observed that higher injection pressure reduces the maximum equivalence ratio, as well as the mass distributed to the higher equivalence ratio region.

A similar plot is reproduced with a different x-axis scale in Figure 6.2(b). This time, the x-axis scale is chosen from 0 to an equivalence ratio of 0.15. It is clearly seen that at lower injection pressures, more mass is present in the low equivalence ratio regions. The lower injection pressure case of P_{inj} = 70 bar shows that almost 60% of the total charge has equivalence ratio close to zero, which represents poor mixing. As the injection pressure increases, the peak value at the lower equivalence ratio is decreased, indicating better mixing over a larger portion of in-cylinder charge mass. The injection pressure of 1000 bar shows that less than 20% of the total charge is located near zero equivalence ratio. Furthermore, it is seen that the 1000 bar injection pressure creates more uniform distribution over a wide range of equivalence ratio. From the statistical analysis in Figures 6.1 and 6.2, it is concluded that a higher injection pressure reduces the level of in-cylinder mixture stratification.

Next, the effect of injection pressure on combustion efficiency and emissions is investigated. Figure 6.3 shows the variations in the combustion efficiency, CO and NO emissions as a function of injection pressure. Despite the large effect on the level of stratification, the net combustion efficiency appears to be relatively insensitive to injection pressure, with only about 10%

decrease within the range of the injection pressure from 70 bar to 1000 bar. On the other hand, NO emission is found to be highly sensitive to injection pressure, especially in the lower pressure range. An increase in the injection pressure from 70 bar to 120 bar leads to nearly 50% reduction in NO. The CO emissions are found to increase monotonically with the injection pressure, which can be attributed to the lower combustion temperatures due to enhanced mixing. These results suggest that a small increase in injection pressure (up to a few hundred bars) can be utilized to improve NO emissions significantly without a large penalty in combustion efficiency and CO emissions.

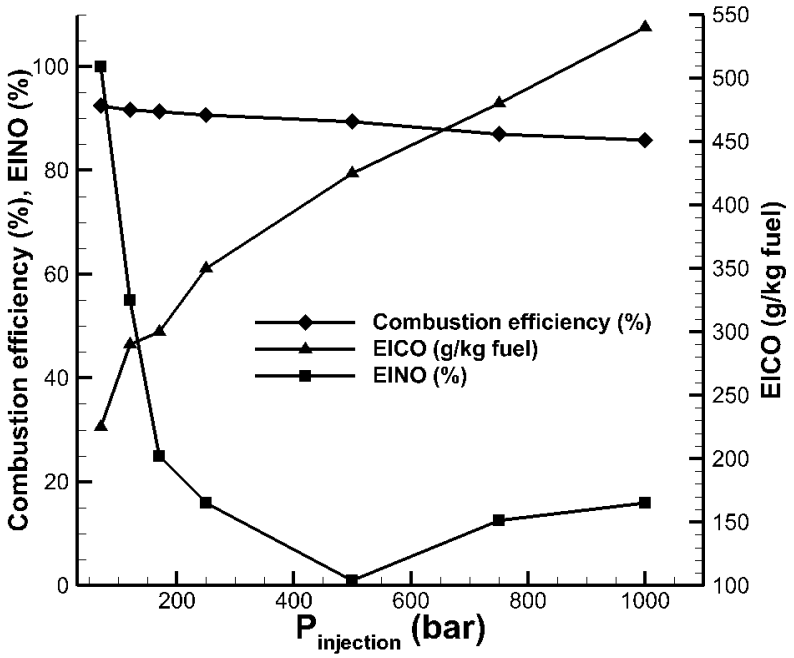

Figure 6.3: Combustion efficiency and CO and NO emissions versus fuel injection pressure.

Considering the large sensitivity in the lower injection pressure range, results from Case 1 (P_{inj} = 70 bar) and Case 3 (P_{inj} =170 bar) are further examined. Figures 6.4 and 6.5 compare the equivalence ratio, temperature and NO distributions at TDC for the two cases. It is evident that higher NO production in case 1 is strongly related to the richer mixture pockets due to their higher combustion temperatures. Comparing the results at 70 bar and 170 bar, it is concluded that the main effect of injection pressure on the reduced NO emissions is through enhanced mixing. This is found to be consistent with previous experiments [120].

6.2.2 Effects of spray cone angle

To assess the effects of spray cone angle, the injection angle is varied from 44^0 (baseline) to 120^0. The five test cases investigated in the present work are listed in Table 6.2. The injection pressure is maintained constant at 70 bar.

Similar to the previous section, the in-cylinder stratification level is first examined by the standard deviation and maximum value of equivalence ratio, as shown in Figure 6.6. It is found that the standard deviation is reduced by two-fold when the cone angle is changed from 44^0 to 70^0. In contrast, to obtain similar reduction in stratification level, the injection pressure had to be increased to as high as 500 bar. It is also noted that both the standard deviation and the maximum equivalence ratio decrease monotonically with the cone angle until 90^0 cone angle. Consequently, the cone angle is found to be a better candidate for controlling mixture stratification than the injection pressure.

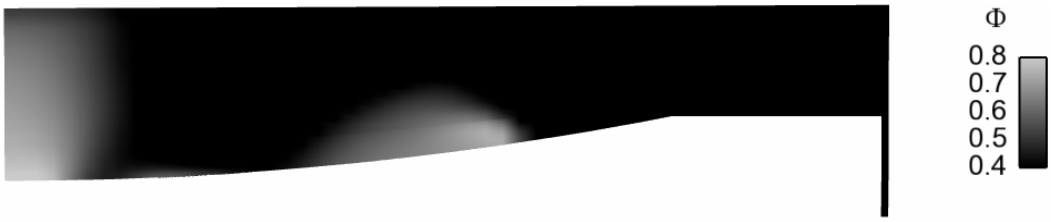

(a)

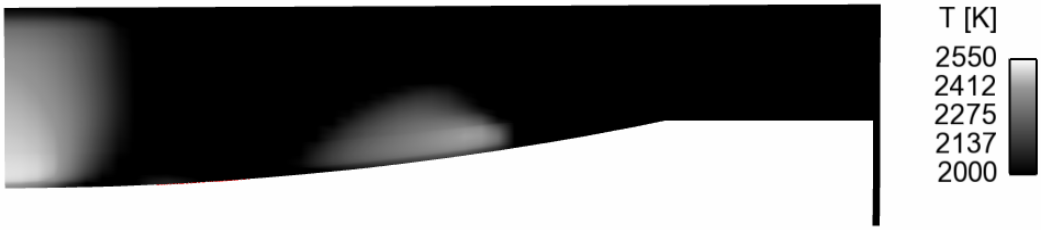

(b)

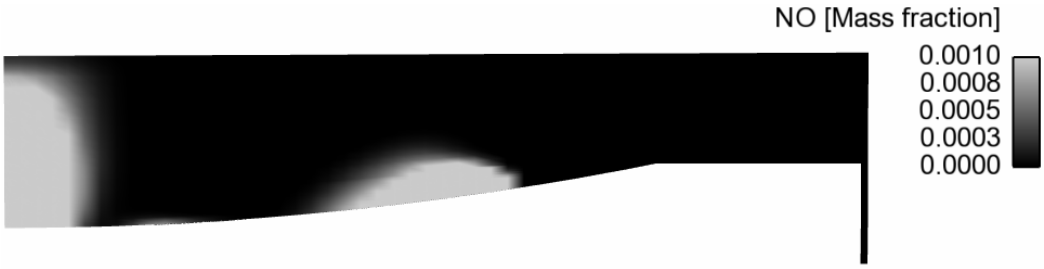

(c)

Figure 6.4: (a) Equivalence ratio, (b) temperature and (c) NO distributions at TDC (360^0 CA) with fuel injection pressure of 70 bar.

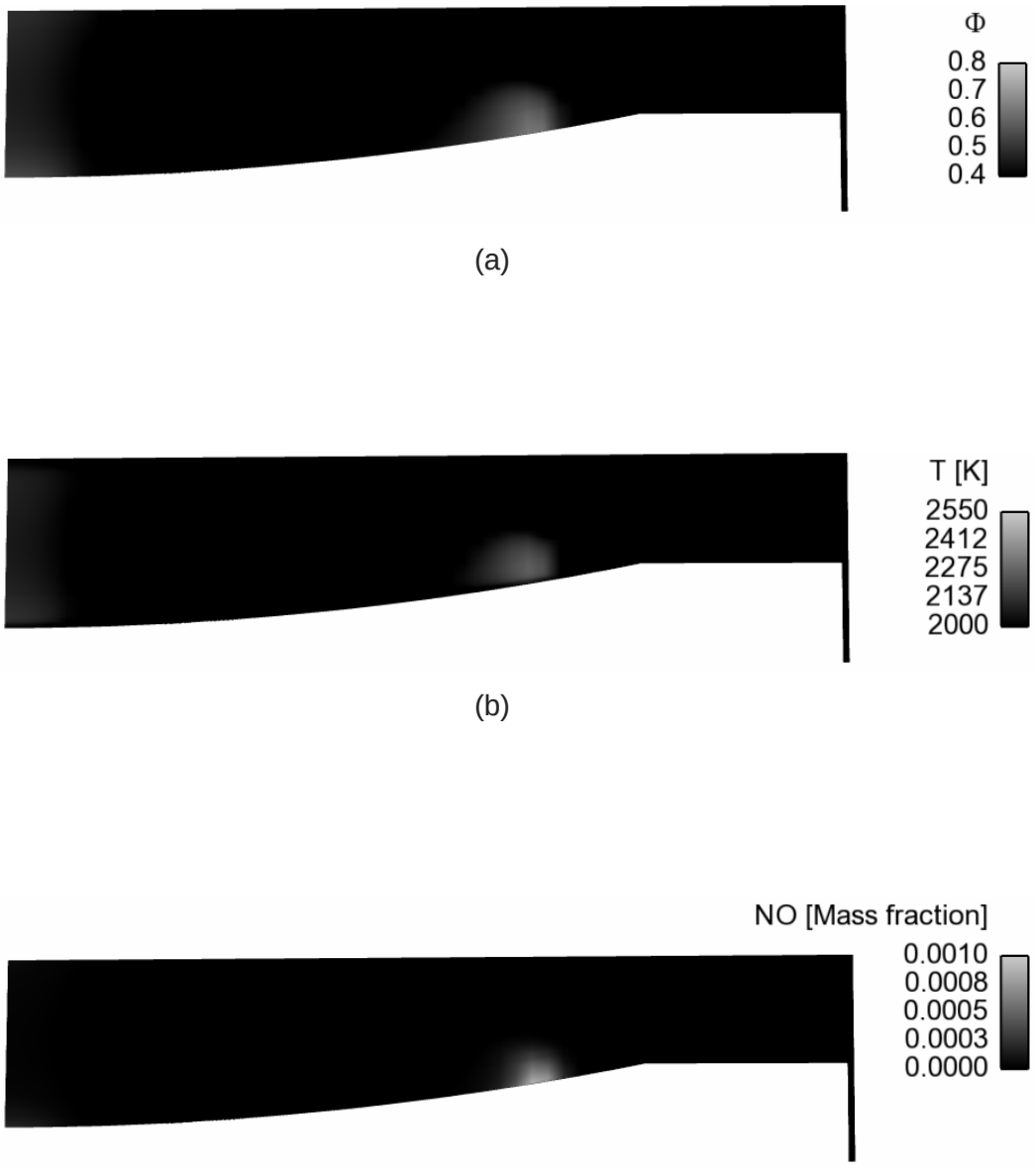

Figure 6.5: (a) Equivalence ratio, (b) temperature and (c) NO distributions at TDC (360^0 CA) with fuel injection pressure of 170 bar.

Table 6.2: Case setup - spray cone angle

Case	Spray cone angle
A	44^0
B	60^0
C	75^0
D	90^0
E	120^0

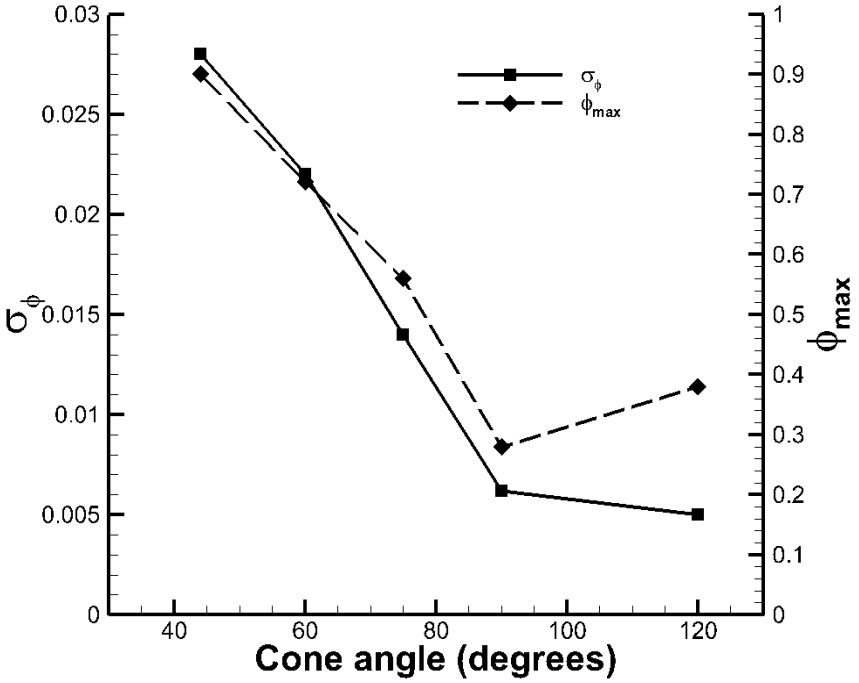

Figure 6.6: Standard deviation and maximum values of equivalence ratio (at TDC) versus fuel injection spray cone angle.

The effects of spray cone angle on combustion efficiency and emissions are shown in Figure 6.7. It is found that variation in the cone angle has little effect on combustion efficiency as well as CO emissions. On the other hand, NO emissions are significantly affected by the spray cone angle. In

particular, an abrupt decrease in NO emissions is observed when the cone angle is increased from 60^0 (Case B) to 75^0 (Case C). Cases B and C are further examined. Figures 6.8 and 6.9 compare the equivalence ratio and NO distributions of the two parametric cases. While the qualitative pictures appear similar, the maximum equivalence ratio (φ_{max}) decreases significantly and becomes less than 0.6 as the cone angle widens from 60^0 to 75^0. In other words, the significant reduction of NO in case C coincides with the mixture condition, $\varphi_{max} < 0.6$. This observation is again consistent with the experimental findings by Hwang et al [120].

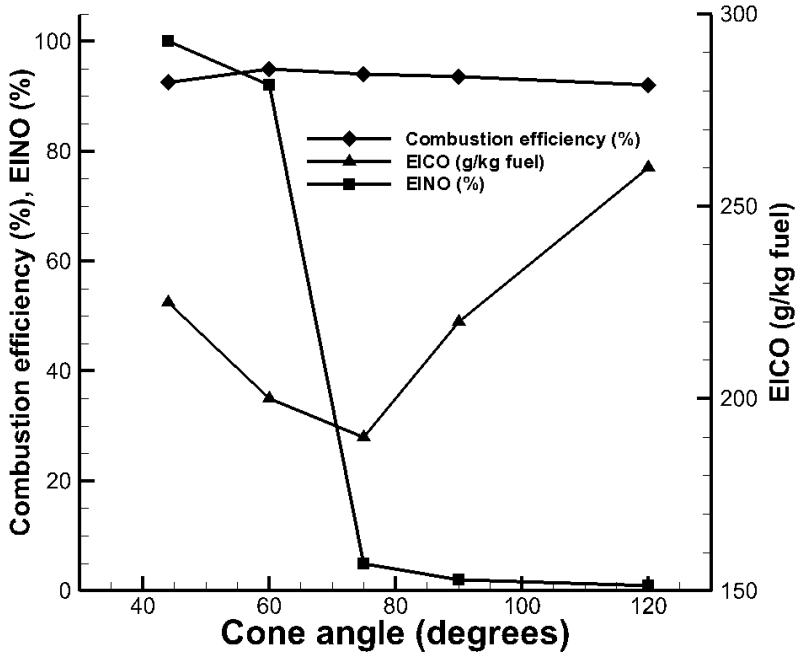

Figure 6.7: Combustion efficiency and CO and NO emissions versus spray cone angle.

To summarize this study, Figure 6.10 shows the NO_x-CO tradeoff curves as either the spray cone angle or the injection pressure is varied. For the

conditions under study, it is found that optimizing spray cone angle is a far better means to improve the emission performance, rather than increasing injection pressure, which would be a much more expensive option in practical applications.

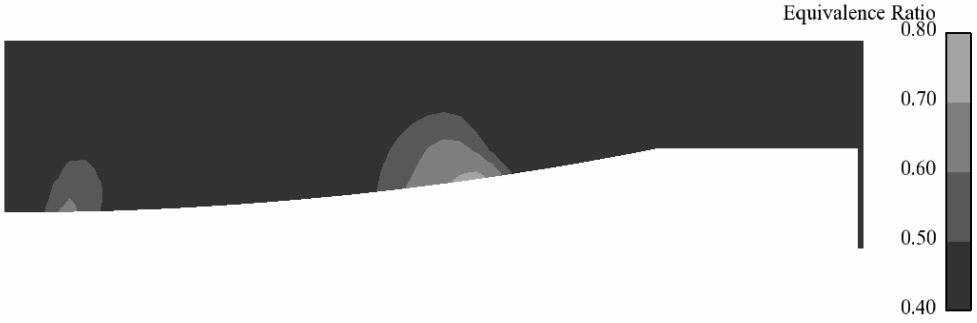

(a)

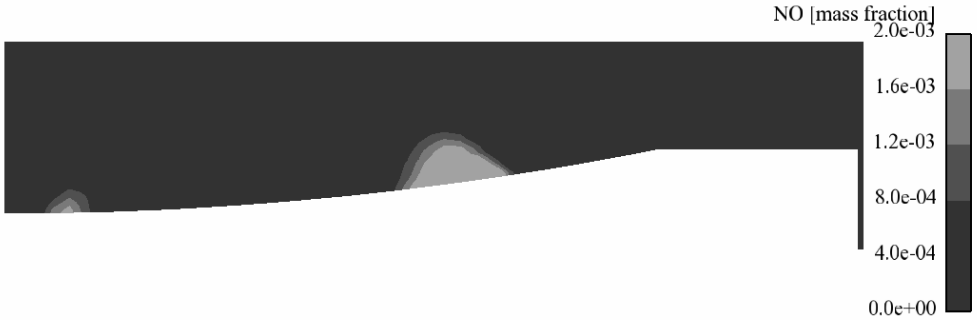

(b)

Figure 6.8: (a) Equivalence ratio and (b) NO distributions at TDC with 60^0 spray cone angle.

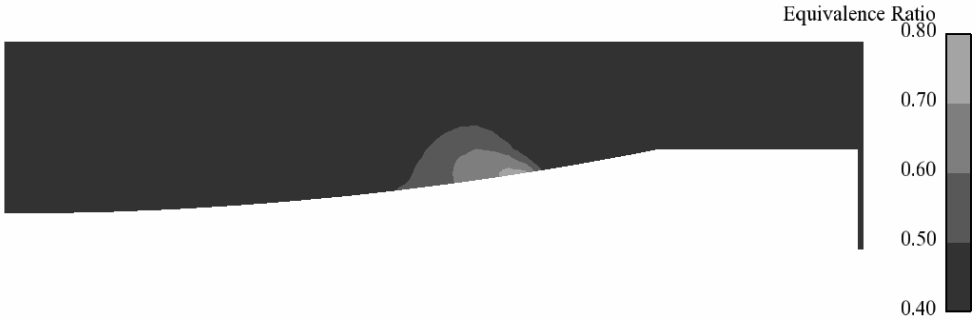

(a)

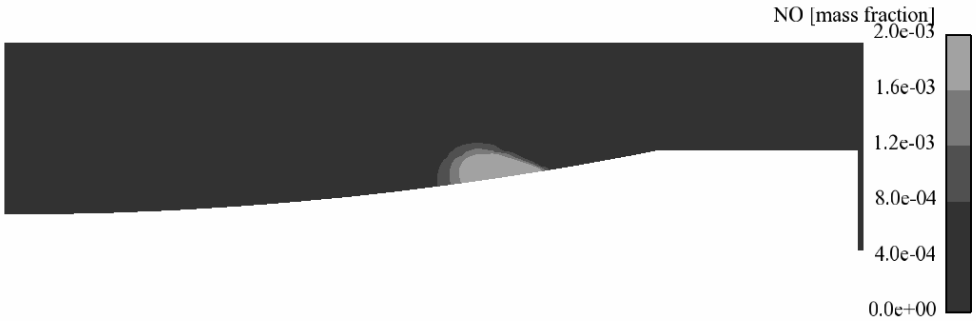

(b)

Figure 6.9: (a) Equivalence ratio and (b) NO distributions at TDC with 75^0 spray cone angle.

6.3 Concluding remarks

The effects of fuel injection parameters on combustion and emissions at low load HCCI operating conditions were numerically investigated for a delayed fuel injection condition beyond the NO_x knee limit. It was found that increasing the injection pressure and widening the cone angle reduced in-cylinder charge stratification. The enhanced mixing resulted in lower in-cylinder temperatures, thereby reducing the NO emission levels significantly.

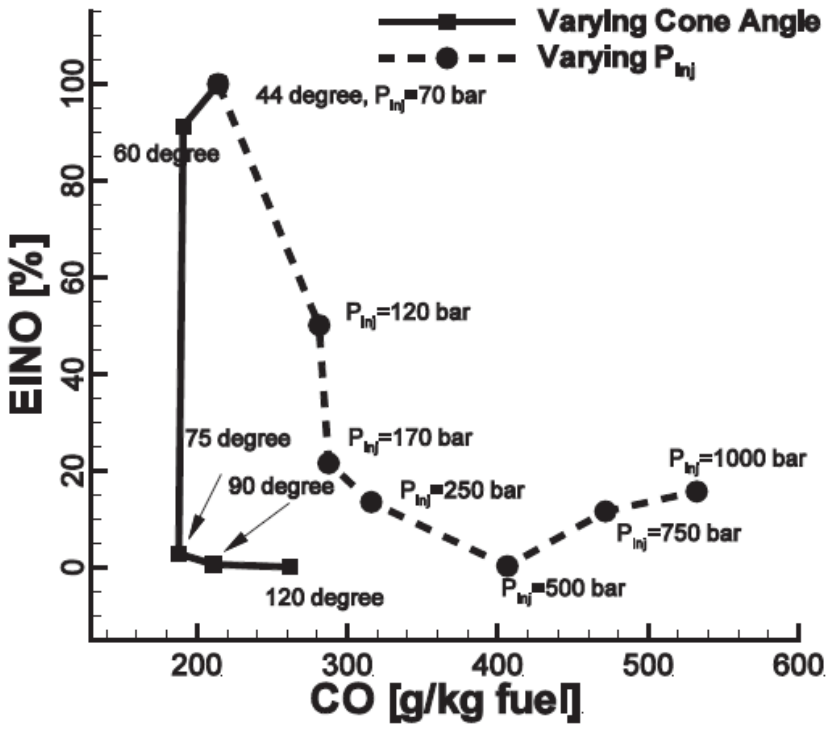

Figure 6.10: NO_x-CO trade-off with varying fuel injection pressure and spray cone angle.

For the current configuration, however, the stratification level defined by the standard deviation of the equivalence ratio did not significantly affect the combustion efficiency and CO emissions. For all parametric cases, it was observed that combustion efficiency was reasonably high (> 85%) and the maximum equivalence ratio was higher than 0.3 but less than 0.6, which was found to be rich enough to maintain stable combustion and low enough to keep the NO_x levels down. The present work demonstrates that an optimization of injection pressure and spray cone angle coupled with delayed fuel injection may be carefully conducted in order to achieve higher combustion efficiency and lower emissions in direct-injection stratified compression ignition engines at low load conditions.

Chapter 7
Conclusions and future work

7.1 Conclusions

This dissertation focused on the systematic investigation of ignition regimes and combustion characteristics relevant to modern LTC strategies employed in advanced gas turbines and IC engines. The technical approach used both theoretical analysis and high-fidelity modeling to develop predictive tools to capture a wide range of behaviors at high-pressure, low-temperature conditions. The major findings of this research are listed below:

- **Chapter 2:** It was demonstrated that in the presence of thermal inhomogeneities such as bulk thermal gradients and local thermal hot spots, transition in auto-ignition behavior could occur from strong (homogeneous) regime to weak (inhomogeneous; deflagration-dominant) regime as the initial reactivity of the mixture was lowered [121]. A predictive criterion, based on the Sankaran number [32], originally derived from Zel'dovich's theory [31], was validated and shown to capture the strong ignition limit, *a priori*. Consistent with previous experimental observations of syngas/air auto-ignition at high pressures and low temperatures [24], it was found that the occurrence of weak ignition resulted in significant advancement of overall ignition. In addition, a mixing Damköhler number was also introduced to take into account the effects of passive scalar mixing on the ignition dynamics. Mixing

effects became dominant at sufficiently low temperatures and resulted in rapid scalar dissipation of the temperature fluctuations, thereby enhancing the propensity to ignite in the strong regime.

- **Chapters 3-4:** The ignition prediction criteria developed above were further extended to turbulent reacting flows in terms of the characteristic turbulent Reynolds and Damköhler numbers, using non-dimensional scaling analysis. The modified ignition criteria led to an ignition regime diagram [122] that classified ignition regimes as weak, reaction-dominant strong, mixing-dominant strong and mixed. Furthermore, validation using a 2D DNS parametric study of syngas/air auto-ignition demonstrated that the regime diagram provided a comprehensive understanding of the physical and chemical mechanisms controlling auto-ignition in the presence of turbulent velocity and temperature fluctuations.

- **Chapter 5:** A numerical study of DI-HCCI combustion at a low load condition was carried out to validate the spray-interactive flamelet (SIF) and extended multi-zone (EMZ) combustion models [123]. A parametric study over a wide range of SOI timings revealed that both models showed comparable fidelity at low stratification level (early fuel injection). However, as charge stratification increased (delayed fuel injection), the SIF model predicted the combustion characteristics and emissions more accurately. The better performance by the SIF model was attributed to the incorporation of small-scale turbulence-chemistry interaction effects in its formulation via the scalar dissipation rate. The numerical study demonstrated that SIF model serves as a more

general framework for LTC simulations over a wider range of stratified conditions.

- **Chapter 6:** A numerical study was conducted using SIF combustion model, to investigate the effects of two fuel injection parameters, injection pressure and spray cone angle, on the overall combustion efficiency and emissions, with the objective of enhancing the effectiveness of the late fuel injection strategy in extending the low load limit of DI-HCCI engines [124]. Increasing the injection pressure and widening the spray cone angle led to lowering of in-cylinder charge stratification, resulting in lower combustion temperatures, thereby reducing the NO_x levels significantly, yet without affecting combustion efficiency and CO emissions markedly. However, optimizing spray cone angle was shown to be a better strategy to improve emission performance, as compared to increasing fuel injection pressure.

7.2 Directions for Future Work

With regard to the ignition regime analysis (chapters 2-4), there is scope to improve upon and extend the findings of the present work. As of now, auto-ignition characteristics of a relatively simple fuel such as syngas have been investigated and used to validate the ignition regime criteria. A similar study with complex hydrocarbon fuels and bio-fuels for both negative temperature coefficient (NTC) and non-NTC conditions would be highly insightful. It will be especially interesting to gauge the predictive capability of Sankaran criterion in these scenarios where the fuel may exhibit complex low-temperature and intermediate-temperature chemistry as well. Secondly, right now, we have conducted DNS studies with 2D turbulence without any vortex stretching and tilting. However, turbulence is inherently a 3D

phenomenon. Therefore, computational studies for realistic 3D turbulent reacting flows will provide better insights into the ignition behaviors.

The current ignition regime theory assumes that only thermal non-uniformities are important. It should be extended to include the effects of compositional fluctuations as well. Finally, the present formulation of the regime theory doesn't provide a criterion to capture detonation, which can potentially be useful in the prediction of super-knock phenomena under boosted high-temperature conditions. A 'modified' Sankaran criterion for detonation can be formulated by substituting S_L with sonic speed, a, in Equation (3.9) and performing a scaling analysis analogous to section 3.2. However, shock-capturing schemes will need to be implemented in the DNS code, S3D that was used in the present work, to conduct validation studies to assess the predictive capability of the new criterion.

Regarding the engine combustion simulation study (chapters 5-6), there are potential improvements that can be made to the SIF combustion model. The current model is based on a single flamelet approach. It should be properly extended to utilize multiple flamelets [79] to account for spatially varying scalar dissipation rate and fuel vaporization. Another important issue to be addressed is accounting for heat transfer. Since all local cells are mapped into one single flamelet, the cells having the same Z value will share similar thermodynamic properties, regardless of their physical locations or different levels of local heat transfer. This issue can be taken care of, following a similar approach to Hergart and Peters [78]. Finally, coupling large-eddy simulation (LES) with the high-fidelity SIF combustion model is another potentially important area of research.

Bibliography

1. R.D. Reitz, *Directions in internal combustion engine research*, Combust. Flame 160 (2013), pp. 1-8.

2. U.S. Energy Information Administration (EIA). *http.eia.gov/.*

3. G.A. Lavoie, J.B. Martz, M.S. Wooldridge, D.N. Assanis, *A multi-mode combustion diagram for spark assisted compression ignition*, *Combust. Flame* 157 (6) (2010), pp. 1106-1110.

4. United States Department of Energy (DOE), *Hydrogen from Coal Program - Research, Development and Demonstration Plan*, 2009. http://fossil.energy.gov/programs/fuels/publications/programplans/2009_Draft_H2fromCoal_Sept30_web.pdf.

5. C-J. Sung, C.K. Law, *Fundamental combustion properties of H_2/CO mixtures: Ignition and flame propagation at elevated pressures*, Combust. Sci. Technol. 180 (2008), pp. 1097-1116.

6. R.A. Dennis, R. Harp, in: Proceedings of ASME Turbo Expo 2007; Power for Land, Sea and Air, Paper GT2007-28338, May 14-17 2007. Montreal, Canada.

7. K.H. Casleton, R.W. Breault, G.A. Richards, *System issues and tradeoffs associated with syngas production and combustion*, Combust. Sci. Technol. 180 (2008), pp. 1013-1052.

8. P. Chiesa, S. Consonni, T. Kreutz, R.H. Williams, *Co-production of hydrogen, electricity and CO_2 from coal with commercially ready technology*, Int. J. Hydrogen Energy 30 (2005), pp. 747-767.

9. M.E. Dry, *The Fischer-Tropsch process: 1950-2000*, Catal. Today 71 (2002), pp. 227-241.

10. D.J. Wilhelm, D.R. Simbeck, A.D. Karp, R.L. Dickenson, *Syngas production for gas-to-liquids applications: technologies, issues and outlook*, Fuel Process. Technol. 71 (2001), pp. 139-148.

11. P. Glarborg, *Hidden interactions - trace species governing combustion and emissions*, Proc. Combust. Inst. 31 (2007), pp. 77–98.

12. P. Chieza, D. Lozza, L. Mazzocchi, *Using hydrogen as gas turbine fuel*, J. Eng. Gas Turbines Power 127 (2005), pp. 73-80.

13. G.A., Richards, M.M. McMillian, R.S. Gemmen, W.A. Rogers, S.R. Cully, *Issues for low-emission, fuel-flexible power systems*, Prog. Energy Combust. Sci. 27(2) (2001), pp. 141–169.

14. T. Lieuwen, V. McDonell, D. Santavicca, and T. SattelMayer, *Burner Development and Operability Issues Associated with Steady Flowing Syngas Fired Combustors*, Combust. Sci. Technol. 180(6) (2008), pp. 1169–1192.

15. M. Chaos, F.L. Dryer, *Syngas combustion kinetics and applications*, Combust. Sci. Technol. 180 (2008), pp. 1053-1096.

16. E.L. Peterson, D.M. Kalitan, A.B. Barrett, S.C. Reehal, J.D. Mertens, D.J. Beerer, R.L. Hack, V.G. McDonell, *New syngas/air ignition data at*

lower temperature and elevated pressure and comparison to current kinetic models, Combust. Flame 149 (2007), pp. 244-247.

17. F.L. Dryer, M. Chaos, *Ignition of syngas/air and hydrogen/air mixtures at low temperatures and high pressures: Experimental data interpretation and kinetic modeling implications*, Combust. Flame 152 (2008), pp. 293-299.

18. D.J. Beerer, V.G. McDonell, *Autoignition of hydrogen and air inside a continuous flow reactor with application to lean premixed combustion*, J. Eng. Gas Turbines Power 130 (5): 051507 (2008).

19. D.M. Kalitan, J.D. Mertens, M.W. Crofton, E.L. Peterson, *Ignition and oxidation of CO/H_2 fuel blends in air*, J. Propul. Power 23 (6) (2007), pp. 1291-1304.

20. S.M. Walton, X. He, B.T. Zigler, M.S. Wooldridge, *An experimental investigation of the ignition properties of hydrogen and carbon monoxide mixtures for syngas turbine applications*, Proc. Combust. Inst. 31 (2007), pp. 3147–3154.

21. S.P. Medvedev, G.L. Agafonov, S.V. Khomik, B.E. Gelfand, *Ignition delay in hydrogen-air and syngas-air mixtures: Experimental data interpretation via flame propagation*, Combust. Flame 157 (2010), pp. 1436-1438.

22. R. Blumenthal, K. Fieweger, K.H. Comp, *Self-ignition of H_2-air mixtures at high pressure and low temperature*, Proc. Int. Symp. Shock Waves 20 (1995), pp. 935-940.

23. V.V. Martynenko, O.G. Penyaz'kov, K.A. Ragotner, S.I. Shabunya, *High-temperature ignition of hydrogen and air at high pressures*

downstream of the reflected shock wave, J. Eng. Phys. Thermophys. 77 (4) (2004), pp. 785-793.

24. A.B. Mansfield, M.S. Wooldridge, *High-pressure low-temperature ignition behavior of syngas mixtures*, Combust. Flame 161 (9) (2014), pp. 2242-2251.

25. T. Javed, E. Es-sebbar, M. Jaasim, J. Badra, H.G. Im, A. Farooq, *Interpreting low-temperature shock tube ignition delay data*, 7th European Combustion Meeting, Budapest, Hungary, 2015.

26. Y. Uygun, S. Ishihara, H. Olivier, *A high pressure ignition delay time study of 2-methylfuran and tetrahydrofuran in shock tubes*, Combust. Flame 161 (2014), pp. 2519-2530.

27. V.V. Voevodsky, R.I. Soloukhin, *On the mechanism and explosion limits hydrogen-oxygen chain self-ignition in shock waves*, Proc. Combust. Inst. 10 (1965), pp. 279–283.

28. J.W. Meyer, A.K. Oppenheim, *On the shock-induced ignition of explosive gases*, Proc. Combust. Inst. 13 (1971), pp. 1153–1164.

29. E.S. Oran, T.R. Young, J.P. Boris, A. Cohen, *Weak and strong ignition. I. Numerical simulations of shock tube experiments*, Combust. Flame 48 (1982), pp. 135-148.

30. E.S. Oran, J.P. Borris, *Weak and strong ignition. II. Sensitivity of the hydrogen-oxygen system*, Combust. Flame 48 (1982), pp. 149-161.

31. Y.B. Zeldovich, *Regime classification of an exothermic reaction with nonuniform initial conditions*, Combust. Flame 39 (1980), pp. 211–214.

32. R. Sankaran, H.G. Im, E.R. Hawkes, J.H. Chen, *The effects of non-uniform temperature distribution on the ignition of a lean homogeneous hydrogen-air mixture*, Proc. Combust. Inst. 30 (2005), pp. 875–882.

33. M. Ihme, *On the role of turbulence and composition fluctuations in rapid compression machines: Autoignition of syngas mixtures*, Combust. Flame 159 (2012), pp. 1592-1604.

34. H. Wu, M. Ihme, *Effects of flow-field and mixture inhomogeneities on the ignition dynamics in continuous flow reactors*, Combust. Flame 161 (2014), pp. 2317-2326.

35. F.L. Dryer, M.S. Wooldridge, E.L. Peterson, V.G. McDonell, H.G. Im, *Panel discussion: Ignition delay issue*, United States Department of Energy University Turbine Systems Research (UTSR) meeting, Purdue, 2014.

36. F. Zhao, T.W. Asmus, D.N. Assanis, J.E. Dec, J.A. Eng, P.M. Najt, *Homogeneous Charge Compression Ignition (HCCI) Engines: Key Research and Development Issues*, Society of Automotive Engineers, Warrendale, PA, 2003.

37. J.E. Dec, *Advanced compression ignition engines - understanding the in-cylinder processes*, Proc. Combust. Inst. 32 (2009), pp. 2727-2742.

38. M. Yao, Z. Zheng, H. Liu, *Progress in recent trends in homogeneous charge compression ignition (HCCI) engines*, Prog. Energy Combust. Sci. 35 (2009), pp. 398-437.

39. X. Lu, D. Han, Z. Huang, *Fuel design and management for the control of advanced compression-ignition combustion modes*, Prog. Energy Combust. Sci. 37(6) (2011), pp. 741-783.

40. S. Saxena, I.D. Bedoya, *Fundamental phenomena affecting low temperature combustion and HCCI engines, high load limits and strategies for extending these limits*, Prog. Energy Combust. Sci. 39(5) (2013), pp. 457-488.

41. S. Onishi, S.H. Jo, K. Shoda, P.D. Jo, S. Kato, *Active thermo-atmosphere combustion (ATAC) - A new combustion process for internal combustion engines*, SAE paper 790501 (1979).

42. P. Najt, D. Foster, *Compression-ignited homogeneous charge combustion*, SAE paper 830264 (1983).

43. R.H. Stanglmaier, C.E. Roberts, *Homogeneous charge compression ignition (HCCI): Benefits, compromise and future engine applications*, SAE paper 1999-01-3682 (1999).

44. J.A. Eng, *Characterization of pressure waves in HCCI combustion*, SAE paper 2002-01-2859 (2002).

45. J.E. Dec, A *computational study of the effects of low fuel loading*, SAE paper 2002-01-1309 (2002).

46. J. Dec, M. Sjoberg, *A parametric study of HCCI combustion- the sources of emissions at low loads and the effects of GDI fuel injection*, SAE paper 2003-01-0752 (2003).

47. M. Sjoberg, J. Dec, N. Cernansky, *Potential of thermal stratification and combustion retard for reducing pressure-rise rates on HCCI engine, based on multi-zone modeling and experiments*, SAE paper 2005-01-0113 (2005).

48. J.E. Dec, Y. Yang, N. Dronniou, *Boosted HCCI – Controlling pressure-rise rates for performance improvements using partial fuel stratification with conventional gasoline*, SAE paper 2011-01-0897 (2011).

49. H. Liu, P. Zhang, Z. Li, J. Luo, Z. Zheng, M. Yao, *Effects of temperature inhomogeneities on the HCCI combustion in an optical engine*, Appl. Therm. Eng. 31 (2011), pp. 2549-2555.

50. R. Sankaran, H.G. Im, *Characteristics of auto-ignition in stratified iso-octane mixture with exhaust gases under homogeneous charge compression ignition engines*, Combust. Theory Modell. 9(3) (2005), pp. 417-432.

51. G. Bansal, H.G. Im, *Autoignition and front propagation in low temperature combustion environments*, Combust. Flame 158 (2011), pp. 2105-2112.

52. C.S. Yoo, T. Lu, J.H. Chen, C.K. Law, *Direct numerical simulations of ignition of a lean n-heptane/air mixture with temperature inhomogeneities at constant volume: Parametric study*, Combust. Flame 158 (2011), pp. 1727-1741.

53. M.B. Luong, Z. Luo, T. Lu, S.H. Chung, C.S. Yoo, *Direct numerical simulations of the ignition of lean primary reference fuel/air mixtures with temperature inhomogeneities*, Combust. Flame 160 (2013), pp. 2038-2047.

54. C.S. Yoo, Z. Luo, T. Lu, H. Kim, J.H Chen, *A DNS study of ignition characteristics of a lean iso-octane/air mixture under HCCI and SACI conditions*, Proc. Combust. Inst. 34 (2013), pp. 2985-2993.

55. S.O. Kim, M.B. Luong, J.H. Chen, C.S. Yoo, *A DNS study of the ignition of lean PRF/air mixtures with temperature inhomogeneities under high pressure and intermediate temperature*, Combust. Flame 162 (2015), pp. 717-726.

56. M.B. Luong, Z. Luo, T. Lu, S.H. Chung, C.S. Yoo, *Direct numerical simulations of the ignition of a lean biodiesel/air mixture with temperature and composition inhomogeneities at high pressure and intermediate temperature*, Combust. Flame 161 (2014), pp. 2878-2889.

57. M.B. Luong, G.H. Yu, T. Lu, S.H. Chung, C.S. Yoo, *Direct numerical simulations of ignition of a lean n-heptane/air mixture with temperature and composition inhomogeneities relevant to HCCI and SCCI combustion*, Combust. Flame (2015), DOI: 10.1016/j.combustflame.2015.09.015.

58. G. Bansal, A. Mascarenhas, J.H. Chen, *Direct numerical simulations of autoignition in stratified dimethyl-ether (DME)/air turbulent mixtures*, Combust. Flame 162 (2015), pp. 688-702.

59. A. Babajimopoulos, G. Lavoie, D. Assanis, *Modeling HCCI combustion with high levels of residual gas fraction - a comparison of two VVA strategies*, SAE paper 2003-01-3220 (2003).

60. R. Hasigawa, H. Yanagihara, *HCCI combustion in DI diesel engine*, SAE paper 2003-01-0745 (2003).

61. A. Bhagatwala, J.H. Chen, T. Lu, *Direct numerical simulations of HCCI/SACI with ethanol*, Combust. Flame 161 (2014), pp. 1826-1841.

62. K. Inagaki, T. Fuyuto, K. Nishikawa, K. Nakakita, I. Sakata, *Duel-fuel PCI combustion controlled by in-cylinder stratification of ignitability*, SAE paper 2006-01-0028 (2006).

63. A. Paykani, A.H. Kakaee, P. Rahnama, R.D. Reitz, *Progress and recent trends in reactivity-controlled compression ignition engines*, Int. J. Eng. Res. (2015), DOI: 10.1177/1468087415593013.

64. A. Bhagatwala, R. Sankaran, S. Kokjohn, J.H. Chen, *Numerical investigation of spontaneous flame propagation under RCCI conditions*, Combust. Flame 162 (2015), pp. 3412-3426.

65. M. Christensen, B. Johansson, A. Hultqvist, *The effect of combustion chamber geometry on HCCI operation*, SAE paper 2002-01-0425 (2002).

66. M. Christensen, B. Johansson, *The effect of in-cylinder flow and turbulence on HCCI operation*, SAE paper 2002-01-2864 (2002).

67. S. Aceves, D. Flowers, C. Westbrook, J. Smith, W. Pitz, R. Dibble, M. Christensen, B. Johansson, *A multi-zone model for prediction of HCCI combustion and emissions* , SAE paper 2000-01-0327 (2000).

68. D.L. Flowers, S. Aceves, J.M. Frias, R. Hessel, R. Dibble, *Effect of mixing on hydrocarbon and carbon monoxide emissions prediction for iso-octane HCCI engine combustion using a multi-zone kinetic solver*, SAE paper 2003-01-1821 (2003).

69. A. Babajimopoulos, D. Assanis, D. Flowers, S. Aceves, R. Hessel, *A fully coupled computational fluid dynamics and multi-zone model with detailed kinetics for the simulation of premixed charge compression ignition engines*, Int. J. Eng. Res. 6 (2005), pp. 497-512.

70. J. Kodavasal, S. Keum, A. Babajimopoulos, *An extended multi-zone combustion model for PCI simulation*, Combust. Theory Modell. 6 (2011), pp. 893-910.

71. J.H. Chen, E.R. Hawkes, R. Sankaran, S. Mason, H.G. Im, Direct *numerical simulation of ignition front propagation in a constant volume with temperature inhomogeneities I. Fundamental analysis and diagnostics*, Combust. Flame 145 (2006), pp. 128-144.

72. E.R. Hawkes, R. Sankaran, P.P. Pebay, J.H. Chen, Direct *numerical simulation of ignition front propagation in a constant volume with temperature inhomogeneities II. Parametric study*, Combust. Flame 145 (2006), pp. 145-159.

73. N. Peters, *Laminar diffusion flamelet models in non-premixed turbulent combustion*, Prog. Energy Combust. Sci. 10 (1984), pp. 319-339.

74. R. Bilger, *Turbulent diffusion flames*, Ann. Rev. Fluid Mech. 21 (1989), pp. 101-135.

75. H. Pitsch, Y. Yan, N. Peters, *Numerical investigation of soot formation and oxidation under diesel engine conditions*, SAE paper 952357 (1995).

76. H. Pitsch, H. Barths, N. Peters, *Three-dimensional modeling of NOx and soot formation in DI-diesel engines using detailed chemistry based on the interactive flamelet approach*, SAE paper 962057 (1996).

77. H. Barths, H. Pitsch, N. Peters, *3D simulation of DI diesel combustion and pollutant formation using a two-component reference fuel*, Oil Gas Sci. Technol.- Rev. IFP 54 (1999), pp. 233-244.

78. C. Hergart, N. Peters, *Applying the representative interactive flamelet model to evaluate the potential effect of wall heat transfer on soot emissions in a small-bore direct-injection diesel engine*, J. Eng. Gas Turbines Power 124 (2002), pp. 1042-1052.

79. H. Barths, C. Hasse, G. Bikas, N. Peters, *Simulation of combustion in direct injection diesel engines using a eulerian particle flamelet model*, Proc. Combust. Inst. 28 (2000), pp. 1161-1168.

80. D.J. Cook, *Combustion and ignition modeling for IC engines*, PhD Thesis, Stanford University, 2007.

81. D.J. Cook, H. Pitsch, G. Nentwig, *Numerical investigation of unburnt hydrocarbon emissions in a homogeneous-charge late-injection diesel-fueled engine*, SAE paper 2008-01-1666 (2008).

82. V. Mittal, D. Cook, H. Pitsch, *An extended multi-regime flamelet model for IC engines*, Combust. Flame 159 (2012), pp. 2767-2776.

83. C. Hasse, N. Peters, *A two mixture fraction flamelet model applied to split injections in a DI diesel engine*, Proc. Combust. Inst. 30 (2005), pp. 2755-2762.

84. E.M. Doran, H. Pitsch, D.J. Cook, *Multi-dimensional flamelet modeling of multiple injection diesel engines*, SAE paper 2012-01-0133 (2012).

85. S. Keum, H.G. Im, D.N. Assanis, *A spray-interactive flamelet model for direct injection engine combustion*, Combust. Sci. Technol. 184 (2012), pp. 469-488.

86. J.H. Chen, A. Choudhary, B. de Supinski, M. DeVries, E.R. Hawkes, S. Klasky, W.K. Liao, K.L. Ma, J. Mellor-Crummey, N. Podhorszki, R.

Sankaran, S. Shende, C.S. Yoo, *Terascale direct numerical simulations of turbulent combustion using S3D*, Comput. Sci. Disc. 2 (2009) 015001.

87. C.A. Kennedy, M.H. Carpenter, *A comparison of several new numerical methods for the simulation of compressible shear layers*, Appl. Numer. Math. 14 (1994), pp. 397-433.

88. J. Li, Z. Zhao, A. Kazakov, M. Chaos, F.L. Dryer, J.J. Scire, *A comprehensive kinetic mechanism for CO, CH_2O and CH_3OH combustion*, Int. J. Chem. Kinet. 39 (2007), pp. 109–136.

89. R.J. Kee, F.M. Rupley, E. Meeks, J.A. Miller, *CHEMKIN-III: a fortran chemical kinetic package for the analysis of gas-phase chemical and plasma kinetics*, Tech. Rep. SAND96-8216, Sandia National Laboratories, 1996.

90. R.J. Kee, G. Dixon-Lewis, J. Warnatz, M.E. Coltrin, J.A. Miller, *A fortran computer code package for the evaluation of gas-phase multicomponent transport properties*, Tech. Rep. SAND86-8246, Sandia National Laboratories, 1986.

91. X.J. Gu, D.R. Emerson, D. Bradley, *Modes of reaction front propagation from hot spots*, Combust. Flame 133 (2003), pp. 63-74.

92. J.H. Chen, S.D. Mason, J.C. Hewson, *The effect of temperature inhomogeneity on low-temperature autoignition of fuel-lean premixed hydrogen/air mixtures*, in: Proc. Third Joint Sections Meeting of the U.S. Sections of the Combustion Institute, 2003.

93. G. Mittal, C-J. Sung, *Aerodynamics inside a rapid compression machine*, Combust. Flame 145 (2006), pp. 160-180.

94. T. Echekki, J.H. Chen, *Analysis of the contribution of curvature to premixed flme propagation*, Combust. Flame 118 (1999), pp. 308-311.

95. H.G. Im, J.H. Chen, *Structure and propagation of triple flames in partially premixed hydrogen-air mixtures*, Combust. Flame 119 (1999), pp. 436-454.

96. A. Liñán, F.A. Williams, *Fundamental aspects of combustion*, Oxford University Press (1993).

97. H. Tennekes, J.L. Lumley, *A first course in turbulence*, MIT Press, Cambridge, MA (1972).

98. J.O. Hinze, *Turbulence*, McGraw-Hill, New York (1975).

99. R.J. Kee, J.F. Grcar, M.D. Smooke, J.A. Miller, *A fortran computer code package for modeling steady laminar one-dimensional flames*, Tech. Rep. SAND85-8240, Sandia National Laboratories, 1985.

100. S.B. Pope, *Turbulent flows*, Cambridge University Press (1975).

101. S.H. Lam, Corrado Casci (Ed.), *Recent advances in the Aerospace Sciences*, Plenum Press, New York and London (1985).

102. S.H. Lam, *The CSP method for simplifying kinetics*, Int. J. Chem. Kinet. 26 (1994), pp. 461–486.

103. M. Valorani, H.N. Najm, D.A. Goussis, *CSP analysis of a transient flame-vortex interaction: time scales and manifolds*, Combust. Flame 134 (2003), pp. 35-53.

104. M. Valorani, F. Creta, D.A. Goussis, J.C. Lee, H.N. Najm, *An automatic procedure for the simplification of chemical kinetic mechanisms based on CSP*, Combust. Flame 146 (2006), pp. 29-51.

105. S. Gupta, H.G. Im, M. Valorani, *Classification of ignition regimes in HCCI combustion using computational singular perturbation*, Proc. Combust. Inst. 33 (2011), pp. 2991-2999.

106. A. Amsden, *A block-structured KIVA program for engines with vertical or canted valves*, LA-13313-MS (1997).

107. M. Sjoberg, J.E. Dec, A. Babajimopoulos, D.N. Assanis, *Comparing enhanced natural thermal stratification against retarded combustion phasing for smoothing of HCCI heat-release rates*, SAE paper 2004-01-2994 (2004).

108. M. Sjoberg, J.E. Dec, *An investigation of the relationship between measured intake temperature, BDC temperature, and combustion phasing for premixed and DI HCCI engines*, SAE paper 2004-01-1900 (2004).

109. Z. Han, R.D. Reitz, *Turbulence modeling of internal combustion engines using RNG k-ε models*, Combust. Sci. Technol. 106 (1995), pp. 267–295.

110. P. O'Rourke, A. Amsden, *The tab method for numerical calculation of spray droplet breakup*, SAE paper 872089 (1987).

111. J. Chen, Y. Chen, Y. Choi, *Development and validation of isooctane skeletal mechanisms based on LLNL detailed mechanism*, Int. J. Vehicle Des. 46 (2008), pp. 128–138.

112. G. Lavoie, J.B. Heywood, J. Keck, *Experimental and theoretical study of nitric oxide formation in internal combustion engines*, Combust. Sci. Technol. 1 (1970), pp. 313–326.

113. N. Peters, *Turbulent combustion*, Cambridge University Press (2000).

114. H. Pitsch, M. Chen, N. Peters, *Unsteady flamelet modeling of turbulent hydrogen-air diffusion flames*, Proc. Combust. Inst. 27 (1998), pp. 1057-1064.

115. R.J. Kee, F.M. Rupley, J.A. Miller, *CHEMKIN-II: a fortran chemical kinetic package for the analysis of gas-phase chemical kinetics*, Tech. Rep. SAND89-9009B, Sandia National Laboratories, 1989.

116. A. Hindmarsh, *LSODE and LSODI, two new initial value ordinary differential equation solvers*, SIGNUM Newsletter 15(4) (1980), pp. 10-11.

117. S.S. Girimaji, *Assumed β PDF model for turbulent mixing: Validation and extension to multiple scalar mixing*, Combust. Sci. Technol. 78 (1991), pp. 177–196.

118. J.B. Heywood, *Internal combustion engine fundamentals*, McGraw-Hill, New York (1988).

119. D.L. Flowers, S.L. Aceves, A. Babajimopoulos, *Effect of charge non-uniformity on heat release and emissions in PCCI engine combustion*, SAE paper 2006-01-1363 (2006).

120. W. Huang, M. Sjoberg, J.E. Dec, *Fuel stratification for low-load HCCI combustion: performance and fuel-PLIF measurements*, SAE paper 2007-01-4130 (2007).

121. P. Pal, A.B. Mansfield, P.G. Arias, M.S. Wooldridge, H.G. Im, *A computational study of syngas auto-ignition characteristics at high-pressure and low-temperature conditions with thermal inhomogeneities*, Combust. Theory Modell. 19(5) (2015), pp. 587-601.

122. H.G. Im, P. Pal, M.S. Wooldridge, A.B. Mansfield, *A regime diagram for autoignition of homogeneous reactant mixtures with turbulent velocity and temperature fluctuations*, Combust. Sci. Technol. 187(8) (2015), pp. 1263-1275.

123. P. Pal, S.H. Keum, H.G. Im, *Assessment of flamelet versus multi-zone combustion modeling approaches for stratified-charge compression ignition engines*, Int. J. Eng. Res. (2015), DOI: 10.1177/1468087415571006.

124. S.H. Keum, P. Pal, H.G. Im, A. Babajimopoulos, D.N. Assanis, *Effects of fuel injection parameters on the performance of homogeneous charge compression ignition at low load conditions*, Int. J. Eng. Res. (2015), DOI: 10.1177/1468087415583597.